Turun yliopisto
University of Turku

MR-BASED ATTENUATION CORRECTION AND SCATTER CORRECTION IN NEUROLOGICAL PET/MR IMAGING WITH ^{18}F-FDG

Jarmo Teuho

TURUN YLIOPISTON JULKAISUJA – ANNALES UNIVERSITATIS TURKUENSIS
Sarja - ser. D osa - tom. 1337 | Medica - Odontologica | Turku 2018

Turun yliopisto
University of Turku

MR-BASED ATTENUATION CORRECTION AND SCATTER CORRECTION IN NEUROLOGICAL PET/MR IMAGING WITH ^{18}F-FDG

Jarmo Teuho

TURUN YLIOPISTON JULKAISUJA – ANNALES UNIVERSITATIS TURKUENSIS
Sarja - ser. D osa - tom. 1337 | Medica - Odontologica | Turku 2018

University of Turku

Faculty of Medicine
Medical Physics and Engineering
Doctoral Programme in Clinical Research
Turku PET Centre, Turku, Finland
National Cerebral and Cardiovascular Centre, Osaka, Japan

Supervised by

Mika Teräs, Professor
Department of Medical Physics
Turku University Hospital
Department of Biomedicine
University of Turku
Turku, Finland

Hidehiro Iida, Professor
Department of Investigative Radiology
National Cerebral and
Cardiovascular Centre
Osaka, Japan

Reviewed by

Hans Herzog, Professor
Institute of Neuroscience and Medicine
Forschungszentrum Jülich
Jülich, Germany

Ronald Boellaard, Professor
Faculty of Medical Sciences
University of Groningen
Groningen, Netherlands

Opponent

Thomas Beyer, Professor
Center for Medical Physics and
Biomedical Engineering
Medical University Vienna
Vienna, Austria

The originality of this thesis has been checked in accordance with the University of Turku quality assurance system using the Turnitin OriginalityCheck service.

ISBN 978-951-29-7137-4 (PRINT)
ISBN 978-951-29-7138-1 (PDF)
ISSN 0355-9483 (Print)
ISSN 2343-3213 (Online)
Painosalama Oy – Turku, Finland 2018

1 Timothy 1:15-16, English Standard Version (ESV)

15 The saying is trustworthy and deserving of full acceptance, that Christ Jesus came into the world to save sinners, of whom I am the foremost. 16 But I received mercy for this reason, that in me, as the foremost, Jesus Christ might display his perfect patience as an example to those who were to believe in him for eternal life.

To Elina

ABSTRACT

Jarmo Teuho

MR-based Attenuation Correction and Scatter Correction in Neurological PET/MR Imaging with ^{18}F-FDG

University of Turku, Faculty of Medicine, Medical Physics and Engineering, Doctoral Programme in Clinical Research, Turku PET Centre, Turku, Finland and The National Cerebral and Cardiovascular Research Centre, Osaka, Japan

Annales Universitatis Turkuensis, Turku, Finland, 2018

The aim was to investigate the effects of MR-based attenuation correction (MRAC) and scatter correction to positron emission tomography (PET) image quantification in neurological PET/MR with ^{18}F-FDG. A multi-center phantom study was conducted to investigate the effect of MRAC between PET/MR and PET/CT systems (I). An MRAC method to derive bone from T1-weighted MR images was developed (II, III). Finally, scatter correction accuracy with MRAC was investigated (IV).

The results show that the quantitative accuracy in PET is well-comparable between PET/MR and PET/CT systems when an attenuation correction method resembling CT-based attenuation correction (CTAC) is implemented. This allows achieving of a PET bias within standard uptake value (SUV) quantification repeatability (< 10 % error) and is within the repeatability of PET in most systems and brain regions (< 5 % error). In addition, MRAC considering soft tissue, air and bone can be derived using T1-weighted images alone. The improved version of the MRAC method allows achieving a quantitative accuracy feasible for advanced applications (< 5 % error). MRAC has a minor effect on the scatter correction accuracy (< 3 % error), even when using MRAC without bone.

In conclusion, MRAC can be considered the largest contributing factor to PET quantification bias in ^{18}F-FDG neurological PET/MR. This finding is not explicitly limited only to ^{18}F-FDG imaging. Once an MRAC method that performs close to CTAC is implemented, there is no reason why a PET/MR system would perform differently from a PET/CT system. Such an MRAC method has been developed and is freely available (http://bit.ly/2fx6Jjz). Scatter correction can be considered a non-issue in neurological PET/MR imaging when using ^{18}F-FDG.

Keywords: PET/MR, PET image quantification, MRAC, scatter correction, attenuation correction

TIIVISTELMÄ

Jarmo Teuho
MR-pohjaisen attenuaatiokorjauksen ja sirontakorjauksen vaikutus neurologisessa PET/MR kuvantamisessa ^{18}F-FDG radiomerkkikaineella

Turun yliopisto, Lääketieteellinen tiedekunta, Lääketieteellinen Fysiikka ja Tekniikka, Turun Kliininen Tohtoriohjelma, Valtakunnallinen PET-keskus, National Cerebral and Cardiovascular Research Centre, Osaka, Japani

Turun Yliopiston Julkaisuja, Turku, Suomi, 2018

Työssä tutkittiin MRI-attenuaatiokorjauksen ja sirontakorjauksen vaikutusta PET-kuvien visuaaliseen ja kvantitatiiviseen tarkkuuteen aivojen PET/MR-kuvantamisessa ^{18}F-FDG radiomerikkiaineella. PET-kuvien tarkkuutta PET/TT ja PET/MR-laitteiden välillä vertailtiin monikeskustutkimuksessa 3D-tulostettulla aivofantomilla (I). MRI-attenuaatiokorjauksen vaikutuksen minimointiin kehitettiin uusi menetelmä (II, III). Lopuksi arvioitiin MRI-attenuaatiokorjauksen vaikutusta PET-kuviin tehtävän sirontakorjauksen tarkkuuteen (IV).

PET-kuvien kvantitatiivinen tarkkuus on hyvin vertailtavissa PET/MR ja PET/TT-laitteiden välillä, kunhan TT-pohjaisen attenuaatiokorjauksen kaltainen menetelmä implementoidaan PET/MR-laitteille. Tämän ansiosta PET-kuviin aiheutuva virhe saadaan SUV-diagnostiikkaan (< 10 % virhe) riittävälle tasolle ja on suuruudeltaan PET-kuvantamisen toistettavuuden tasoa (< 5 % virhe) useammissa aivojen alueissa. Tämän tarkkuuden saavuttava menetelmä kehitettiin, käyttäen ainoastaan T1-painotteisia MRI-kuvia. Menetelmän kehittyneempi versio on tarkkuudeltaan riittävä haastavampiin sovelluksiin (< 5 % virhe). MRI-pohjaisella attenuaatiokorjauksella ei ole merkittävää vaikutusta sirontakorjausalgoritmin tarkkuuteen (< 3 % virhe), jopa silloin kuin luukudos jätetään huomiotta.

MRI-pohjainen attenuaatiokorjaus on suurin virhetekijä aivojen PET/MR-kuvantamisessa. Attenuaatiokorjauksen suorittaminen TT-pohjaisella tai sen tarkkuutta parhaiten vastaavalla MRI-pohjaisella menetelmällä on riittävä minimoimaan suurimmat virhelähteet PET/MR ja PET/TT-laitteiden välillä. Tämän tarkkuuden saavuttava MRI-pohjainen menetelmä kehitettiin ja on saatavilla ilmaiseksi tutkimuskäyttöön (http://bit.ly/2fx6Jjz). Sirontakorjauksen vaikutusta PET-kuvien kvantitatiiviseen tarkkuuteen voidaan pitää vähäisenä aivojen ^{18}F-FDG PET/MR-kuvantamisessa.

Avainsanat: PET/MR, kvantitatiivinen PET-kuvantaminen, MRAC, sirontakorjaus, attenuaatiokorjaus

TABLE OF CONTENTS

ABBREVIATIONS

^{11}C	Carbon-11 isotope
3D	Three-dimensional
^{18}F	Fluoride-18 isotope
^{68}Ga	Gallium-68 isotope
^{15}O	Oxygen-15 isotope
AAL	Automated anatomical labelling
ACF	Attenuation correction factor (1/cm)
CSF	Cerebrospinal fluid
CT	Computed tomography
Cs-137	Cesium-137 isotope
FDG	Fluorodeoxyglucose
FOV	Field of view
dRHE	Dual-echo ramped hybrid encoding
GE	General Electric
Ge-68	Germanium-68 isotope
GM	Gray matter
GPU	Graphics processing unit
HU	Hounsfield unit
K2HPO4	Kalium dipotassium hydroxide
keV	Kilo electron volt
LOR	Line of response
LOR-RAMLA	Line of response row action maximum likelihood algorithm
MC	Monte Carlo
MC-SSS	Monte Carlo single scatter simulation
MLAA	Maximum-likelihood reconstruction of attenuation and activity
MNI	Montreal neurological institute
MR	Magnetic resonance
MRAC	MR-based attenuation correction
MRI	Magnetic resonance imaging
MR-RT	MR-only radiotherapy planning
NAC	Non attenuation corrected (PET images)

OSEM	Ordered subsets expectation maximum algorithm
PET	Positron emission tomography
PET/CT	Positron emission computed tomography
PET/MRI	Positron emission magnetic resonance imaging
PETRA	Point-wise encoding time reduction with radial acquisition
PiB	Pittsburgh compound B
PSF	Point spread function
PSMA	Prostate specific membrane antigen
R2*	Transverse relaxation rate (1/T2*)
ROI	Region of interest
SPM	Statistical parametric mapping
SSS	Single scatter simulation
STE	Short echo time
SUV	Standard uptake value (g/ml)
SUVr	Standard uptake value ratio
T1	T1 relaxation time
T2	T2 relaxation time
T2*	T2* relaxation time
TF	Tail fitting
TF-SSS	Tail fitted single scatter simulation
TOF	Time of flight
TPB-AC	Tissue probability-based attenuation correction
TX	Transmission (Ge-68 or Cs-137 attenuation scan)
TXAC	Transmission-based attenuation correction
UTE	Ultra-short echo time
VOI	Volume of interest
WM	White matter
ZTE	Zero echo time

LIST OF ORIGINAL PUBLICATIONS

This doctoral dissertation consists of a summary and of the following publications which are referred to in the main text of the thesis by their numerals.

I. **Teuho, J.**, Johansson, J., Linden, J., Hansen, A.E., Holm, S., Keller, S.H., Delso, G., Veit-Haibach, P., Magota, K., Saunavaara, V., Tolvanen, T., Teräs, M., Iida, H.. *Effect of Attenuation Correction on Regional Quantification Between PET/MR and PET/CT: A Multicenter Study Using a 3-Dimensional Brain Phantom.* Journal of Nuclear Medicine 57, 818–824 (2016).

II. **Teuho, J.**, Linden, J., Johansson, J., Tuisku, J., Tuokkola, T., Teräs, M.. *Tissue Probability-Based Attenuation Correction for Brain PET/MR by Using SPM8*. IEEE Transactions on Nuclear Science 63, 2452–2463 (2016).

III. **Teuho, J.**, Tuisku, J., Karlsson, A., Linden, J., Teräs, M.. *Effect of brain tissue and continuous template-based skull in MR-based attenuation correction for brain PET/MR*. IEEE Transactions on Nuclear Science (digital) DOI:10.1109/TNS.2017.2692306 / IEEE Transactions on Radiation and Plasma Medical Sciences (in print) 1, 246 - 261 (2017).

IV. **Teuho, J.**, Saunavaara, V., Tolvanen, T., Tuokkola, T., Karlsson, A., Tuisku, J., Teräs, M.. *Quantitative evaluation of two scatter correction techniques for* ^{18}*F-FDG brain PET/MR imaging in regard to MR-based attenuation correction.* Journal of Nuclear Medicine 581, 691-1698 (2017).

Original publications are reproduced by permission from the copyright holders.

1 INTRODUCTION

The introduction of simultaneous PET/MR systems for clinical use in 2011 has been suggested to mark a paradigm shift for neuroimaging, especially in the field of neurodegenerative diseases by using ^{18}F-FDG in combination with MRI (Zaidi et al., 2011; Barthel et al., 2015). The soft tissue contrast and functional imaging capabilities of MRI combined with the quantitative nature of PET allow broadening the diagnostic capabilities for brain imaging in PET/MR compared to standalone PET and MR systems (Bailey et al., 2015). However, the methodological challenges related to major quantitative data corrections such as attenuation and scatter in PET/MR imaging to the visual and quantitative accuracy of PET images in neurological PET/MR studies should be evaluated.

1.1 MR-based attenuation correction for brain PET/MR

The inherent methodological property in MRI is that tissue intensities in MR images correspond to tissue relaxation times and proton density – a different physical quantity compared to CT or transmission imaging (Hofmann et al., 2009; Mehranian et al., 2016). Therefore, MRI tissue intensities do not directly correspond to electron density of tissues, allowing no direct transformation to tissue attenuation properties. In addition, the delineation and visualization of bone in the head region has been a challenge before the introduction of ultra-short echo time (UTE) and zero echo time (ZTE) sequences. When using conventional T1- or T2-weighted MRI, bone tissue and air appear with similar intensity due to the short T2* relaxation of bone, making it hard to distinguish and differentiate bone from air and take it into account in MR-based attenuation correction (MRAC).

Due to these inherent challenges in deriving bone density information (due to measurement of a different physical quantity) and visualizing bone (due to similar intensity in non-UTE sequences) from MR images, earlier clinical implementations of MR-based attenuation correction ignored bone entirely in both whole-body imaging and in the brain, replacing bone with soft tissue (Schultz et al., 2011). This was reported to cause a large, spatially varying bias in the regions close to bone, such as in the cortical regions of the gray matter. Errors of magnitude from -10 % to -25 % were initially reported, which could be visually differentiable as hypometabolism – a potential factor for misdiagnosis, impairing the diagnostic quality of the PET/MR images (Andersen et al., 2014). It is now generally agreed that at least soft tissue, air and bone are needed in the MR-based attenuation map of the head to achieve an acceptable visual and quantitative accuracy in PET when imaging the head region using ^{18}F-FDG.

The “MRAC problem”, as it was commonly called in 2014 in the scientific community, was the starting point of research for many scientists to find an optimal attenuation correction method for brain PET/MR. This “MRAC problem” has recently been solved by the introduction of several advanced methods allowing to achieve quantitative accuracy close to CT-based attenuation correction (CTAC) (Ladefoged et al., 2017). Currently, CTAC is widely considered the clinical “de facto” standard of attenuation correction due to its widespread availability and use in PET/CT. It should be noted here that CTAC is still a mere “silver standard” for attenuation correction (Hitz et al., 2014), although generally accepted as an accurate and robust method available for clinical routine. Only transmission-based attenuation correction (TXAC) using a rotating Ge-68 source, which is nearly no longer available, might be considered as the gold standard method available for attenuation correction, allowing measurement of linear attenuation coefficients at photon energies of 511 keV (Hoffman and Phelps et al., 1986; Bailey et al., 1998).

In the years of accomplishing this thesis work (from 2013 to 2017), a multitude of MRAC methods have been introduced and significant methodological advances have been made in the entire PET/MR field of neuroimaging. Due to the sheer extent of methods introduced in both whole-body and brain PET/MR imaging and wide range of radiotracers, this thesis will focus mostly on MRAC methods for brain imaging and ^{18}F-FDG. These MRAC methods can be divided into three broad categories, including segmentation-based, atlas-based and emission-based methods. Some methods can also be a combination of the previous three categories. These methods will be inspected in detail in Chapter 2.

In general, the main idea behind any MRAC method is to derive and approximate a “true” attenuation map of the head region based on information existing in measured MRI, emission data, CT-MRI atlas data or a combination of these. With this in mind, it should be stated that even the most accurate MR-based attenuation map is a finely calculated approximation of the true attenuation coefficients in the volume. Thus, the final accuracy requirements of an MR-based attenuation map will be determined by the end application and the clinical criteria and intent. Furthermore, it is relevant whether the MRAC-corrected PET images will be evaluated by visual or quantitative analysis with a clinical or scientific purpose in mind. At bare minimum, differentiation between air, soft tissue and bone should be achievable.

1.2 Scatter correction in brain PET/MR imaging

In addition to attenuation correction, scatter correction is one of the major quantitative corrections performed on PET data, as the fraction of scattered photons in 3D PET acquisitions in the brain region is increased to over 30 % (Zaidi et al., 2004). In essence, scatter and attenuation correction are closely related as the MR-derived attenuation map is used in calculation of the scattered photons when performing single scatter simulation (SSS). Therefore, any inaccuracies existing in the MR-based attenuation map used for scatter correction may propagate to the calculated scatter estimate or affect the accuracy of scatter scaling procedures. To this day, there have been only a few published reports which investigate MRAC-based errors and their effect on the accuracy of scatter correction (Bourgos et al., 2014).

Generally, the effect of erroneous scatter correction may introduce variation in quantitative parameters measured from PET images and at worst introduce artifacts which hinder the visual interpretation of the PET images (Cherry et al., 1995). For these reasons, the effect of MRAC on scatter correction accuracy should be determined and if needed, minimized. As scatter correction remains an integral part of quantitative PET imaging, its performance and accuracy in ^{18}F-FDG studies for PET/MR neuroimaging in relation to MRAC need to be studied in detail. Although vendor-based implementations of scatter correction may vary, the methods implemented on all major PET/MR and PET/CT systems are based on the general idea of determining the spatial location and distribution of photons undergone a single Compton scattering event. Details of the scatter correction procedures in PET will be inspected in detail in Chapter 2.

1.3 Summary

To summarize and conclude this introductory chapter, investigating the accuracy of attenuation and scatter correction in neurological PET/MR imaging is important concerning PET image quantification and visual quality when using 18F-FDG as radiotracer. Both of these data corrections are essential to achieve visually and quantitatively accurate diagnostic PET images.

To approach these issues practically: 1) the nature, cause and magnitude of the bias introduced by MR-based attenuation correction or scatter correction need to be determined to establish a common baseline of the performance of the correction methods and algorithms specifically in PET/MR systems in comparison to PET/CT systems and CT-based attenuation correction, 2) any PET/MR-specific technical challenges related to attenuation or scatter corrections need to be minimized by development and evaluation of new techniques, 3) recommendations based on the findings in 1) and 2) need to be done to minimize the quantitative and visual differences and their effect in PET due to attenuation and scatter corrections in clinical PET/MR for neuroimaging.

2 REVIEW OF THE LITERATURE

The advent of clinical PET/MR imaging with the introduction of two sequential systems, the Philips Ingenuity TF (Zaidi et al., 2011), the GE Tri-Modality PET/MR (Veit-Haibach et al., 2011) and two simultaneous systems, the Siemens Biograph mMR (Delso et al., 2011) and GE SIGNA (Grant et al., 2016) marked a paradigm shift in the area of neuroimaging. Combining PET and MR in the same system is a clear advantage and has potential in a number of clinical and research applications, especially in the field of neurology and neurodegenerative diseases. In these fields, ^{18}F-FDG represents a universal marker of neuronal and synaptic integrity with relatively disease-specific uptake reduction patterns (Barthel et al., 2015). A likely clinical key application of simultaneous PET/MR is in neurological disorders, especially in dementia imaging (Bailey et al., 2015; Drzezga et al., 2014, Dukart et al., 2011).

Simultaneous or near-simultaneous (sequential) acquisition of PET and MR allows several benefits in both research and clinical routine setting. One evident benefit is the improved data quality, clinical workflow, patient convenience and diagnostic imaging performance as the PET and MR images can be acquired in simultaneous fashion without co-registration of separate PET and MR acquisitions (Zaidi et al., 2011; Barthel et al., 2015). The benefits to clinical workflow due to decreased acquisition time can naturally be achieved only with a simultaneous system. By combining the soft tissue imaging contrast with the molecular and functional imaging from MR and the quantitative nature of PET creates possibilities for complementary, multi-parametric imaging (Herzog et al., 2010; Herzog et al., 2016; Bailey et al., 2015). Thus, both imaging modalities benefit when they are combined in a single system. It should be emphasized that all of the benefits stated above will be realized fully with a truly simultaneous PET/MR system.

However, for accurate visual identification, clinical diagnosis, radiotracer quantification and kinetic modeling both the visual and quantitative accuracy of the PET images needs to be guaranteed. Many of these applications rely on a solid quantitative foundation, which is highly dependent on the performance characteristics of the PET system and the accuracy of data correction and image reconstruction algorithms (Zaidi and Sossi et al., 2004).

A number of PET/MR-specific methodological challenges exist which need to be considered concerning the accuracy of PET images when using a PET/MR system. Most of these challenges are of a technical nature and are related to photon attenuation and scatter correction performed to PET images, both of which are obligatory prerequisites for quantitative and visually accurate ^{18}F-FDG PET images.

Therefore, the accuracy and performance of these data corrections will significantly affect the clinical usability and adoption of neurological ^{18}F-FDG imaging on PET/MR systems.

2.1 Physical process of photon attenuation in positron emission tomography

During PET image reconstruction process, two major data corrections are performed to account for the physical processes of the attenuation and scattering of the two 511 keV annihilation photons. Photon attenuation is the dominant physical degrading factor besides the contribution from scattered photons and other associated errors in the data acquisition and reconstruction process (Zaidi et al., 2004).

At photon energies of 511 keV, Compton processes dominate in interactions inside the tissue. The physical basis of photon attenuation is shortly explained in the following paragraphs while photon scattering will be covered in detail in section 2.5.

The magnitude of photon attenuation can be expressed by an exponential equation:

$$I(x) = I_0 e^{-\int_0^x \mu(x)dx}, \tag{1}$$

where I and I_0 are the attenuated and the un-attenuated intensity of the radiation (the photon flux) passing through a medium of tissue with an linear attenuation coefficient μ (expressed as probability of attenuation in cm^{-1}) at a point x along a line-of-response (LOR), in the case of a single detector.

For two coincidence detectors, the total probability of a successful detection of a coincidence event is the product of two probabilities expressed by (eq. 1) along a LOR from the annihilation point to opposite detectors A and B. Thereafter, the exponential term can be expressed for a non-uniform attenuating medium (e.g. patient head) as a constant (α) for a given LOR by following factor for each projection:

$$\alpha = e^{-\int_0^{A+B} \mu(x)dx}. \tag{2}$$

Thereafter, the uncorrected emission counts C_x for a given LOR can be expressed as an integral of attenuated point sources C_o multiplied by constant α (Hoffman and Phelps et al., 1986; Bailey et al., 1998):

$$C_x = \alpha \int C_o(x)dx, \tag{3}$$

where the attenuation correction factor (ACF) becomes simply ACF = 1/α for each LOR. As can be seen from (eqs.1 to 3), the ACFs are given directly along a LOR if I and I_0 can be measured by e.g. transmission scanning (Bailey et al., 1998). Another option is to calculate or approximate these ACFs (Zaidi et al., 2003) i.e by determining the object contour from projection data (Bergström et al., 1982).

Once these ACFs are derived, the attenuation corrected emission intensity $EM_{corrected}$ along the LOR can be calculated by using measured, uncorrected emission intensity $EM_{measured}$ and the derived ACFs. In the simplest form, performing attenuation correction for PET is a multiplicative operation of each projection of the measured emission data with the corresponding, measured or approximated ACFs:

$$EM_{corrected} = EM_{measured} \times ACF. \qquad (4)$$

The recovered activity in the PET images is thus affected by a multiplicative factor due to attenuation correction. The measured or calculated attenuation map of the patient's anatomy needs to include the measured or calculated μ-values.

The effect of attenuation correction to PET image quantification is thus dependent on the μ-values in the attenuation map. The effect of attenuation is determined based on these μ-values located in the paths of both annihilation photons and the path length of the photons travelling to two detectors defining an LOR.

2.2 Attenuation correction in standalone PET, PET/CT and PET/MR

In standalone PET systems, attenuation correction is performed by using transmission-based attenuation correction (TXAC). In TXAC, attenuation coefficients of 511 keV photons can be measured with a rotating Ge-68 source and in some systems, a Cs-137 transmission source integrated in the PET gantry. Applying the Ge-68 TXAC, first the attenuation sinogram containing the ACFs and second by reconstructing the attenuation map of the attenuating volume inside the gantry can be fully recovered. Thus, TXAC is still considered the gold standard method for attenuation correction although it's use has nearly stopped due to the diminishing number of standalone PET systems and the increasing number of PET/CT systems.

In PET/CT systems, the attenuation map of the object is derived using CT-based attenuation correction (CTAC). The attenuation coefficients for 511 keV photons from CT photon energies of typically 120 keV (range 80-140 keV) can be derived from the patient CT images. The HU values in CT images can be converted by bilinear transformation from HU to linear attenuation coefficients in cm^{-1} (Figure 1). This conversion is based on the linear relation between the attenuation coefficients and HU values, which is valid for the range of biological tissues. However, in high density materials such as Teflon, the conversion curve can no longer be considered accurate (Son et al., 2010). A number of bi-linear transforms are reported in the literature (Burger et al., 2002; Bai et al., 2003; Carney et al., 2006; Kinahan et al., 1998). The bi-linear transforms of Burger and Bai (Burger et al., 2002; Bai et al., 2003) are optimized for 120 keV tube voltages while the transform suggested by Carney (Carney et al., 2006) comprises a range of tube energies from 80 keV to 140 keV. Although CTAC has replaced TXAC as the clinical "de facto" standard, it can be considered as a "silver standard" compared to TXAC (Hitz et al., 2014). Thus, it is important to consider the variability in CTAC implementations as well as the difference between CTAC and measured attenuation maps using 511-keV photon sources (Su et al., 2016).

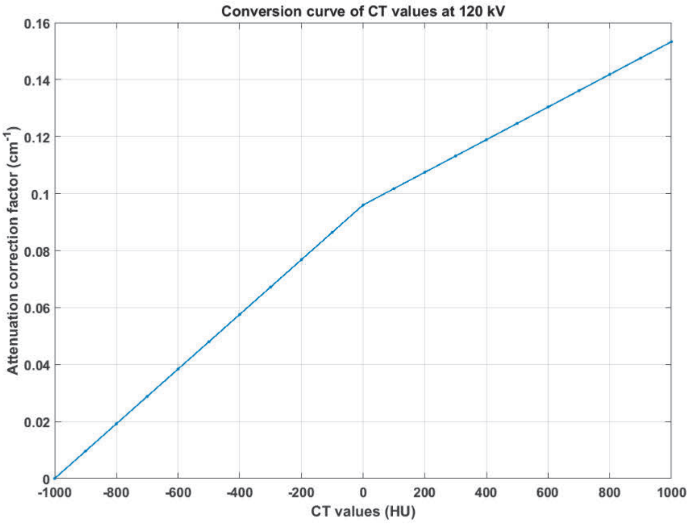

Figure 1. A simulated CT conversion curve from HU values to linear attenuation coefficients at tube energy of 120 kV using the transformation of Burger et al., (Burger et al., 2002).

In PET/MR, compared to standalone PET systems and PET/CT systems, there is no direct relation between MR signal intensity and photon attenuation (Hofmann et al., 2009; Mehranian et al., 2016). MR signal intensity is related to the proton density and individual T1 and T2 relaxation of the tissues, whereas photon attenuation at energies of 511 keV is related to the material atomic number Z and electron density (Hofmann et al., 2009; Mehranian et al., 2016). Thus, no direct transformation from an MR image to a PET attenuation map exists similar to TXAC or CTAC. Therefore, the MR-based attenuation map can only be an approximation of the true attenuation map.

In addition, bone and air may appear with similar intensity, dependent on the MR pulse sequence, although their attenuation coefficients are very different. For these reasons, the early implementations of MR-based attenuation correction considered soft tissues and air only, while bone was ignored entirely. Furthermore, hardware components in the MR field of view (FOV) remain invisible as well with conventional pulse sequences and need to be included in the patient attenuation map separately. A common approach to include the fixed hardware components such as the patient table and the MR coils is by registration of transmission- or CT-based templates into the patient attenuation map (Delso et al., 2010; Zhang et al., 2009) to compensate for their attenuation.

The clinical MRAC methods developed by Schultz (Schulz et al., 2011), Martinez-Möller (Martinez-Möller et al., 2009) and Wollenweber (Wollenweber et al., 2013) segment out the body tissues to three (soft tissue, air, lung) or four classes (soft tissue, fat, lung, air) either as discrete tissue classes or as a weighted average (Wollenweber et al., 2013b). The method described by Schultz is implemented as the MRAC method for the Philips Ingenuity TF PET/MR (Hu et al., 2009) while the method of Martinez-Möller is implemented in the Siemens Biograph mMR PET/MR. Both of these methods ignore bone in the head region, although the present Biograph mMR includes an alternative option to use UTE for bone delineation (Dickson et al., 2014). The method described by Wollenweber is implemented in the GE SIGNA PET/MR and uses an atlas-based method (Wollenweber et al., 2013a) for accounting for bone in the head region. Table 1 lists the commonly reported attenuation coefficient ranges for soft tissue, fat and bone.

Table 1. Commonly reported attenuation coefficients and their ranges in biological tissue (Mehranian et al., 2016). The bone ranges could be considered valid for a normal population. More variation could be expected in bone pathophysiology.

Tissue	Attenuation coefficient at 511 keV (cm-1)
Soft tissue	0.096
Fat	0.086 to 0.093
Spongeous bone	0.110
Cortical bone	0.130 to 0.172

As seen in (Table 1), bone tissue has much higher attenuation values compared to soft tissue. Replacing bone with soft tissue introduces a significant bias in the PET images, which is especially relevant in the brain region (Andersen et al., 2014). This effect is related to the attenuation path length of the two annihilation photos from the annihilation site to the coincidence detectors. A simple illustration of this phenomenon is shown in Figure 2. If the photon annihilation site is located close to the patient skull, such as in the cortical regions of the brain, the contribution to the total attenuation path length from the higher attenuation of the patient skull is larger than from the mid-brain region. For the annihilation sites in the mid-brain region, the contribution of brain and soft tissue is larger compared to the contribution of the skull to the total attenuation path length of both coincidence photons.

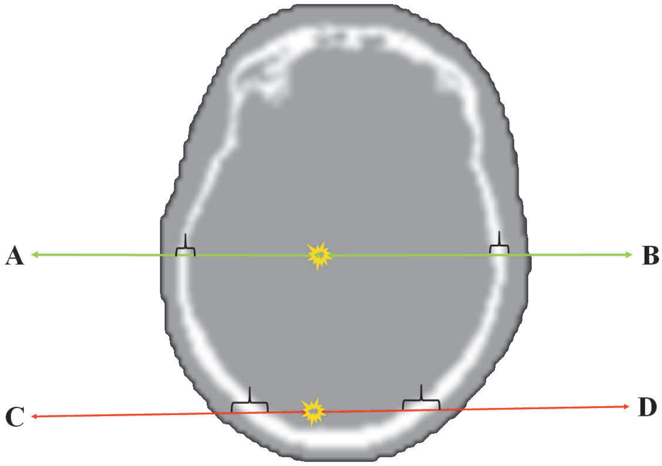

Figure 2. Illustration of the effect of ignoring bone in a patient (Andersen et al., 2014). The contribution of attenuation of the skull of mid-brain (green lines) and cortical regions (red lines) depends on the attenuation path length through bony tissue (black parentheses) of the photon to the detector pairs (A, B) and (C, D).

Several authors have reported a large regional bias in the cortical regions in ^{18}F-FDG PET images when using MRAC and ignoring bone in the MR-based attenuation map. The bias caused by MRAC is spatially variable being highest in the outer cortical structures and lower in the central brain, causing the activity in the cortical regions to be underestimated and the central region to be overestimated (Andersen et al., 2014). If the bias would be more systematic and uniform across the brain (a level bias), it could be more easily ignored. Andersen et al., reported a negative bias of 5-10 % in the central regions and 25 % in the cortical regions in a phantom and patient study (Andersen et al., 2014), Hitz et al., reported a mean negative bias of 15 % globally and in the range of 15 % to 20 % in cortical regions (Hitz et al., 2014) while Dickson et al., reported a bias of 21.3 % and 19.8 % at maximum (range 21 % to 11 %) when using a Dixon-based sequence and a bias of 15.7 % and 17.3 % at maximum (range 17 % to 4 %) when using a UTE-based sequence to account for bone (Dickson et al., 2014), a surprisingly large bias even when using UTE.

These reports concluded unanimously that the lack of bone in the MR-based attenuation map contributed to the bias seen in the PET images. The bias is most prominent with ^{18}F-FDG and other radiotracers with large cortical uptake. Furthermore, the bias was determined to be regionally varying. Therefore, the attenuation of the skull bones needs to be accounted for in MR-based attenuation correction for visually and quantitatively accurate PET images on PET/MR systems. In recent years, the field of MR-based attenuation correction has been a very active and rich area of research in search of a method which could compensate bone most effectively or even create a patient-specific CT substitute (pseudo-CT).

2.3 Methods to account for bone in MR-based attenuation correction of the head region

To account for bone tissue in MRAC of the head, a multitude of methods have been introduced. These methods can be generally divided into segmentation-based, atlas- or template-based and emission- or reconstruction-based methods. In the following sections, we describe each of the main categories of MRAC methods in detail.

2.3.1 Segmentation-based MRAC

Segmentation-based methods are generally based on separating the tissues in MR images into three (soft tissue, air and bone) or more tissue classes by image segmentation. Segmentation is usually performed on images acquired either with a specialized MR sequence (e.g. UTE, ZTE) or can be performed based on anatomical T1-weighted, T2-weighted or Dixon images collected as part of the routine examination (Mehranian et al., 2016; Keereman et al., 2013; Wagenknecht et al., 2013). Thereafter, each tissue class is assigned an attenuation coefficient corresponding to its expected (e.g. the mean) attenuation properties. Thus, tissue homogeneity inside a specific volume of tissue and within a specific population is assumed. These are the natural limitations of segmentation-based MRAC using discrete tissue classes, as a single attenuation coefficient cannot be considered to account for all the inter- and intra-patient variations of biological tissue.

To delineate bony tissues and to account for bone, UTE-based methods were initially introduced (Keereman et al., 2010; Catana et al., 2010) and are also clinically implemented in the present Biograph mMR PET/MR system. Multiple methods based on segmentation of T1-weighted, T2-weighted and Dixon attenuation images have also been presented as well. Zaidi and Fei proposed using T1-weighted MRI images, which are co-registered to PET data and segmented by fuzzy C-means clustering to air, scalp, skull, gray matter, white matter and nasal sinuses (Zaidi et al., 2003b; Fei et al., 2012). Andearsen proposed using a patch-based method for generation of pseudo-CT from T1-weighted images (Andearsen et al., 2015). Anazodo (Anazodo et al., 2014) initially suggested the use of Dixon images with bone component added from T1-weighted images by segmentation in SPM8, whereas a similar clinical prototype has been introduced recently by Koesters (Koesters et al., 2016) allowing bone (continuous or discrete) to be added to Dixon MRAC images (Rausch et al., 2017).

Compared to methods that do not account for bone, UTE-based methods have been shown to improve both the visual and quantitative accuracy of PET images (Keereman et al., 2010; Catana et al., 2010; Berker et al., 2012). However, several authors have reported inconsistencies in bone delineation with UTE-based attenuation maps as well (Dickson et al., 2014; Delso et al., 2014a), which have led to the development of more advanced segmentation methods and adaptation of new MRI sequences and image segmentation techniques. These include short echo time (STE)/Dixon and fuzzy clustering (Khateri et al., 2015), improved UTE using point-wise encoding time reduction with radial acquisition (PETRA) (Grodzki et al., 2012) or likewise a fast dual-echo ramped hybrid encoding (dRHE) (Jang et al., 2017), reduction of eddy current artifacts (Aitiken et al., 2014), zero echo time (ZTE) sequences (Delso et al., 2015; Wiesinger et al., 2016; Sekine et al., 2016c; Yang et al., 2017) or by using triple UTE (Aitiken et al., 2014; Berker et al., 2012; Su et al., 2015). These methods have been shown to outperform the clinically used UTE-based method in terms of accuracy of the attenuation map, PET image quality and quantitative accuracy.

In clinically used segmentation-based MRAC, the number of tissue classes is either three or four tissues independent of the acquisition type. It has been shown that increasing the number of tissue classes in segmentation-based MRAC, the absolute quantification errors in each different tissue class decrease (Ouyang et al., 2013). Akbarzadeh et al., confirmed that the accuracy of segmentation-based MRAC improves as the number of tissue classes increases (Akbarzadeh et al., 2011; Akbarzadeh et al., 2013). Keereman et al., showed in their simulation study that at least six tissue classes (air, lung, soft tissue, fat, spongious and cortical bone) should be identified in MRAC to reduce quantification errors to less than 5 % (Keereman et al., 2011). Therefore, increasing the number of tissue classes in the attenuation map has been considered beneficial, at least to a certain degree.

The largest limitation generally considered for segmentation-based MRAC methods is their reliance on discrete tissue classes and attenuation coefficients, which do not model the heterogeneity of individual tissues or patients well. While most segmentation-based methods rely on discrete attenuation coefficients, methods which derive continuous attenuation coefficients for bone have been introduced recently (Navalpakkam et al., 2013; Lagefoed et al., 2015; Juttukonda et al., 2015;

Cabello et al., 2015; Khalife et al., 2017). In general, the methods of (Lagefoed et al., 2015; Juttukonda et al., 2015; Cabello et al., 2015) are based on advanced segmentation procedures and a derived model between the relationship of R2* values from UTE images and HU values from CT images to derive patient-specific bone attenuation values. Similarly to UTE, a linear model between ZTE intensity and CT HU values has been recently shown to be applicable to derive continuous bone values (Khalife et al., 2017; Yang et al., 2017b). Performance of methods using continuous attenuation values is generally considered superior over discrete-tissue methods.

In summary, while segmentation-based methods were limited to discrete attenuation coefficients in the past, new methods have recently become available that allow us to derive patient-specific, continuous linear attenuation coefficients for bone. In general, segmentation-based MRAC methods have shown good performance with more complex approaches for MRAC, achieving good quantitative and visual accuracy in PET. As segmentation-based approaches are simple to implement, time efficient in acquisition- and processing-wise and generally considered robust, they remain popular in vendor-based implementations of clinical MRAC and in the research setting.

2.3.2 Template- and Atlas-based MRAC

Atlas- or template-based methods are based on co-registration between a database of CT and MR image parts, which are matched either on a volume-by-volume, slice-by-slice or voxel-by-voxel basis based on a predefined similarity metric. A CT substitute or a “pseudo-CT” is typically created which corresponds to the subject anatomy with continuous attenuation coefficients for the whole imaging volume. A collection of atlases, template registration to the target subject or the use of machine learning techniques with trained classifiers or mapping functions is used to create the pseudo-CT (Mehranian et al., 2016). While these methods allow to derive very accurate subject-specific attenuation maps, their disadvantage is the added complexity and computational cost.

These methods can be based either on a single atlas or a multiple atlas approach (Sekine et al., 2016b). A single-atlas method is currently vendor-implemented for clinical attenuation correction of brain studies on the SIGNA PET/MR. The method is based on MRI/CT pairs to derive the approximate size and location of bones and air cavities (Wollenweber et al., 2013a) in the head region. Initial evaluations of this method have shown that with patients with normal anatomy, the method achieves quantitative accuracy similar to that of CTAC (Sekine et al., 2016a, Yang et al., 2017a), although a bias in the cerebellum region has been reported (Yang et al., 2017b). Yang (Yang et al., 2017a) hypothesized that registration errors between the CT atlas and in-phase MR images would be the largest cause of errors in the atlas-based attenuation map. Large evaluations of the performance of the method with patients with abnormal anatomy have not yet been performed, to the best knowledge of the author.

The simplest and most straightforward template-based methods to implement are those which involve registration and non-linear wrapping of predefined TXAC or CTAC template to individual subject anatomy which are then used for attenuation correction (Kops et al., 2008; Kops et al., 2015). Templates can be created by taking an average of multiple co-registered CTAC or TXAC images to represent mean attenuation coefficients and anatomical variability in a given population (Zaidi et al., 2007). A natural limitation of single-template methods is that inter-subject variation of attenuation coefficients are ignored. Another limitation is that only a single anatomical transformation is performed, which may suffer from registration errors or inter-patient anatomical variability (Mehranian et al., 2016). Thus, the method accuracy is affected by the accuracy of the registration. Despite these shortcomings, single template-based and single-step registration methods have been shown to have good quantitative accuracy (Wollenweber et al., 2013a) and (Kops et al., 2015) when compared to CTAC or TXAC.

Multiple atlas registration was initially suggested to overcome and minimize non-systematic registration errors (Mehranian et al., 2016). Multiple methods using this approach have been introduced recently. More complex approaches can be based on pairs of CT and UTE images using clusters or patches in tissue delineation (Delso et al., 2014b; Roy et al., 2014) or using pairs of CT and anatomical MR images (Andreasen et al., 2015; Bourgos et al., 2014; Bourgos et al., 2015; Izquierdo-Garcia et al., 2014; Merida et al., 2017; Schreibmann et al., 2010; Sekine et al., 2016b; Torrado-Carvajal et al., 2016). Probabilistic measurers or machine learning techniques can also be applied for pseudo-CT creation (Chen et al., 2015; Chen et al., 2017; Hofmann et al., 2008; Johansson et al., 2011; Johansson et al., 2014; Larsson et al., 2013; Navalpakkam et al., 2013; Poynton et al., 2014). There is evidence that multi-atlas approaches are generally superior to single-atlas approaches, mainly due to better delineation of the patient anatomy and improved registration accuracy (Sekine et al., 2016b).

Atlas-based pseudo-CT generation methods have been shown to exhibit good performance and quantitative accuracy (< 5 %) when compared to CTAC (Mehranian et al., 2016; Ladefoged et al., 2017). A suggested challenge for atlas-based methods are patients with abnormal or deformed anatomy if the atlas is constructed using normally corresponding subjects. In addition, specified templates or atlases are needed for pediatric patients (Berzukow et al., 2015). However, no large comparisons between atlas-based and segmentation-based methods have been performed with large patient groups with deformed anatomy or patient groups with a known condition of reduced bone mineral density (osteopenia or osteoporosis). There is evidence that atlas-based methods would maintain good performance even in the presence of deformed anatomy or brain tumors (Izquierdo-Garcia et al., 2014) in addition to advanced segmentation-based methods (Lagefoed et al., 2017).

In general, atlas-based methods allow deriving continuous attenuation values by either registration of a CT/TX-template or creation of a patient-specific pseudo-CT. Several methods, especially those based on the multi-atlas approach, have been introduced recently for MRAC. Atlas-based methods achieve a good quantitative and visual performance compared to CTAC, at the level of PET reproducibility (±5 % bias compared to CTAC). A drawback of atlas-based methods is the increased computational complexity and the need to construct an atlas or database of subject CT and MRI images, compared to segmentation-based approaches.

2.3.3 Emission- or reconstruction-based MRAC

Emission– or reconstruction-based methods generally allow deriving an attenuation map based on reconstruction of emission data alone, by combination of jointly reconstructed emission and transmission data or by the use of information from scattered coincidences. The early attempts to derive the attenuation coefficients were based on emission data by using the consistency conditions of the Radon transform such as the Helgason-Ludwig principle (Natterer et al., 1992, Natterer et al., 1993) or time of flight (TOF) attenuated Radon transform (Defrise et al., 2012), allowing us to derive the attenuation factors up to a constant scaling factor. TOF allows measuring the location of annihilation by an uncertainty determined by the timing resolution of the system (Meheranian and Zaidi et al., 2016). Extensions of the work of Defrise (Defrise et al., 2012) included the extension to 3D PET and addition of prior information from MRI (Rezaei et al., 2012b; Li et al., 2015). To the best knowledge of the author, these methods have not been extensively examined for clinical use.

The maximum-likelihood reconstruction of both attenuation and activity (MLAA) was originally proposed by Nuyts et al., (Nuyts et al., 1999), based on a concept introduced by Censor et al., (Censor et al., 1979). The MLAA method is based on simultaneous reconstruction of both attenuation and activity using maximum likelihood expectation maximization (MLEM) algorithm and enables deriving of an attenuation sinogram up to a constant using emission data only. The inherent issues with MLAA are cross talk artifacts between attenuation and emission data and dependence on good count statistics, i.e. high quality of the emission data (Mehranian et al., 2016); these have limited its applicability to non-TOF imaging until recently (Benoit et al., 2015). Another approach is to jointly estimate the emission distribution and the attenuation correction factors, avoiding the reconstruction of the attenuation map. Rezaei et al., (Rezaei et al., 2014) proposed a maximum likelihood algorithm to jointly estimate the activity distribution and attenuation correction factors (MLACF), up to a scaling constant. A scale corrected MLACF has recently been shown to provide images that quantitatively and visually correspond to CTAC reconstructed PET images (Bal et al., 2017).

To reduce the cross-talk and dependence on count statistics in MLAA, use of TOF information with MLAA has been shown to be beneficial (Rezaei et al., 2012a) in addition to incorporating spatial constraints e.g. from MRI data to improve the MLAA estimate (Salomon et al., 2011). Another suggested approach is to use MRI-guided MLAA, imposing MRI spatial and CT statistical constraints with a Gaussian mixture model and Markov random field smoothness prior (Mehranian et al., 2015b). However, a recent study comparing MLAA and atlas-based MRAC showed that the MLAA approach might be limited for brain PET/MR imaging (Mehranian et al., 2016b), although advanced MLAA methods with additional penalty functions might offer better performance in brain imaging (Mehranian et al., 2017). Recently, Cheng et al., also proposed a method to initialize the joint reconstruction with initial average μ-value to improve TOF-MLAA (Cheng et al., 2016). Additionally, the use of MR-based attenuation image was proposed to circumvent the TOF requirement (Benoit et al., 2015) and to limit both the scale problem and cross-talk. It can be seen that MLAA remains an active and popular field of research, although with the exception of (Benoit et al., 2015) and (Mehranian et al., 2016b), no large clinical studies have been performed. It remains to be seen whether TOF-MLAA could be a promising reconstruction technique to enhance the quantitative accuracy of PET/MR studies as proposed by (Boellaard et al., 2014).

Instead of using emission data alone, it might be beneficial to estimate the attenuation coefficients using the joint reconstruction of emission and transmission data. The concept was introduced by Clinthorne et al., (Clinthorne et al., 1991). The main problem was to reduce the cross-contamination between emission and transmission data. Based on TOF capability to separate emission and transmission data, Moellet et al., were able to implement simultaneous transmission and emission scanning, using an annulus-shaped transmission source (Mollet et al., 2012; Mollet et al., 2014). However, the limited TOF resolution of current PET systems does not allow perfect separation of transmission and emission data (Mollet et al., 2014). In addition, the use of transmission source or LSO background radiation has been proposed to further improve and stabilize the MLAA estimation (Panin et al., 2013; Rothfuss et al., 2014; Watson et al., 2013). Although these methods can be used to stabilize and improve the quantitative performance of the emission-only MLAA algorithm, their clinical use remains limited. Finally, the use of scattered coincidences to improve the estimated attenuation coefficients in MLAA has been suggested. Berker et al., proposed to reconstruct PET attenuation coefficients from scattered photon energies in the range of 248-478 keV (Berker et al., 2014).

Incorporating TOF information in PET image reconstruction has also been proven beneficial concerning quantitative and visual accuracy of PET images. The additional information TOF offers allows to update the image voxels along segments of response instead of the whole LOR, reducing the cross-dependencies between individual image voxels (Meheranian and Zaidi et al., 2016). This reduces the sensitivity of TOF reconstruction to errors. Conti et al., (Conti et al., 2011) showed that TOF reconstruction is less sensitive to inconsistencies in emission data and data corrections such as attenuation, normalization and scatter. Quantification errors caused by imperfect attenuation correction are reduced by TOF as was proved in a simulation study by (Boellaard et al., 2014), in whole-body examinations (Meheranian and Zaidi et al., 2016) and recently in brain imaging (Khalife et al., 2017). It may be expected that second-generation PET/MR systems with increased TOF timing resolution will offer improved quantitative accuracy and will be less limited by the inaccuracies of MRAC.

In general, reconstruction-based methods remain an active area of research for MRAC. There have only been a few initial clinical evlauations and reports in neurological imaging. The quantitative performance of the methods has not been extensively compared in clinical studies. The greatest limitation of the emission-based methods is their dependence on the radiotracer accumulation, dependence on the availability of TOF data and the need to achieve high data quality (assuming that PET data corrections such as scatter correction will not introduce more errors), which limits their applicability to clinical practice. As most of the methods are applied to ^{18}F-FDG data only, their applicability to other radiotracers with different activity distributions from ^{18}F-FDG would be an interesting field of study.

Although for the moment it seems that the reconstruction-based methods have not yet reached full maturity compared to segmentation- or atlas-based methods, they will certainly remain an intriguing option and research field to derive MRAC for whole-body examinations and clinical brain ^{18}F-FDG PET/MR imaging. The advantage of the emission-based methods referred to in this section is flexibility: they are not specifically limited to either whole-body or brain imaging only and can be applied to any specific situation.

2.4 Validation and evaluation of MR-based attenuation correction methods in the head region

MR-based attenuation correction methods need to be evaluated and compared based on their performance in realistic PET data. As stated by Berker et al.„ two different attenuation maps can be considered to be equally suited for attenuation correction as long as their forward projections (the attenuation correction sinograms) are similar enough on LORs with high attenuation or with LORs containing many counts (Berker et al., 2016). The evaluation with PET and transmission (CT or TX) data should be performed while keeping this in mind.

There is currently no mutually agreed standard on MRAC method validation. Differences exist in the analysis methods used for method evaluation and validation in the literature, hindering comparison between the MRAC methods (Ladefoged et al., 2017; Rausch et al., 2017). It was recently shown (Rausch et al., 2017) that there is a need to agree on a common evaluation standard to achieve a more reliable comparison between different methods. This would also be helpful in interpreting the numerical results reported in a clinically meaningful way. As the relative errors measured with any of the advanced MRAC methods for the head region are in the magnitude of few percentages (from 2 % to 7%) (Ladefoged et al., 2017), small differences in data processing, creation of a reliable reference data and PET data evaluation will certainly create some deviation. Moreover, whether these differences are really meaningful from a clinical perspective should also be clearly stated. However, some common metrics can be found; these are collected below.

In general, the comparison of MR-based attenuation maps is made against either CT-based or TX-based attenuation correction. Both the MRAC and CTAC/TXAC are visually or quantitatively compared on the accuracy of bone delineation on the MR-based method against the CTAC/TXAC reference. The following discussion refers to the works of (Bezrukov et al., 2013; Hofmann et al., 2009; Keereman 2013c; Mehranian et al., 2016; Wagenknecht et al., 2013), unless otherwise stated. Typically, a visual inspection of PET images reconstructed with the MRAC method against CTAC/TXAC reconstructed images is performed. Finally, quantitative analysis of PET images using CTAC/TXAC reconstructed PET as the reference is made. In quantitative analysis, an automatic or semi-automatic VOI analysis is the most common metric, performed with a large number of VOIs in cortical regions or other specified regions of interest. The number of regions used varies from study to study. Quantitative analysis might also include pixel-wise calculation of bias or ratio images to differentiate regions not specified in the VOI analysis for comparison of quantitative performance in PET on a global and local scale.

The MR-based attenuation maps should be validated against the reference attenuation data (CTAC/TXAC) for accuracy of bone delineation and/or attenuation values. The accuracy of bone delineation is usually determined either by visual evaluation of bone structures in MRAC versus CTAC or by quantitative analysis. In quantitative analysis, comparison of similarity in bone delineation can be performed by evaluation of similarity in amount of overlapping structures of segmented bone between MRAC and CTAC. Metrics such as Dice coefficient (eq. 5) or Jaccard index (eq. 6) are commonly used for this purpose.

$$Dice\ coefficent = \frac{2|A \cap B|}{|A|+|B|} \tag{5}$$

$$Jaccard\ index = \frac{|A \cap B|}{|A \cup B|} \tag{6}$$

These metrics (eqs. 5 and 6) describe the overlap between CT-based and MR-based bone voxels in co-registered and segmented attenuation maps. Direct voxel-wise differences of the attenuation maps in CT- and MR-based methods may also be calculated.

The evaluation with PET data is similarly performed. PET data reconstructed with CTAC or TXAC are considered as the reference data. The relative differences of MRAC reconstructed PET data are compared to reference attenuation reconstructed PET data, either by radioactivity values (kBq/mL), normalized activity values (SUV) or SUV ratio (SUVr) by semi-automatic VOI analysis in certain regions of interest. Thereafter, the bias, correspondence to CTAC reconstructed PET and the remaining error in the MRAC reconstructed PET are determined by additional analysis.

Common error metrics include: mean relative difference, mean average error (MAE), standard average error (SAE), slope and fit against reference data in linear regression analysis, comparison of coefficient of determination R^2 and Pearson linear correlation coefficient p. It should be noted that metrics such as R^2 and correlation coefficient p will only allow to determine which MRAC method gives a better correlation against CTAC, which does not explicitly imply good agreement between the two methods. Therefore, to analyze the agreement between MRAC and CTAC reconstructed PET images, Bland-Altman analysis should be conducted. Statistical testing using a two-tailed Student's t-test or Wilcoxon rank sum test may be performed to investigate whether regional differences in MRAC reconstructed PET are significantly different from CTAC reconstructed PET. In addition, voxel-wise difference or ratio images may be calculated to investigate the voxel-wise regional bias throughout the brain in regions which are not covered by the VOI analysis.

Recently, efforts have been made to validate MRAC by its effect on dynamic PET images and kinetic modeling (Merida et al., 2017). Although only a small number of reports exists, the analysis is made by inspection and comparison of regional time-activity curves and the derived modeling parameters (Merida et al., 2017). However, no large evaluations on the effect of MRAC on quantitative parameters derived by kinetic modeling have been performed so far. Recent studies have shown that improving the accuracy of the MRAC is beneficial for modeling purposes and the derived parameters, e.g. receptor binding potential (Merida et al., 2017). It is expected that the MRAC methods applied for static PET imaging will be validated and applied for dynamic PET as well using similar metrics as in static PET.

Eventually, the results from the MRAC method validation and evaluation should be transferred to clinically meaningful and interpretable information. There have been only a few extensive clinical reports of analysis and validation from different MRAC methods with large patient cohorts in neurological ^{18}F-FDG imaging, using the metrics applied commonly in clinical routine.

2.4.1 Acceptable clinical limit for accuracy of PET image quantification and visual accuracy with MRAC

The information gained in the evaluation of MRAC methods needs to be converted to a clinically interpretable information. The challenge is to present performance criteria which would be meaningful concerning the usability of any MRAC method in clinical routine and whether the use of MRAC would significantly impair or improve the diagnostic confidence of PET findings. Evaluations of this kind have been widely performed for lesion quantification using SUV for whole-body PET/MR imaging. However, the criteria in these evaluations could be applied for clinical brain PET/MR imaging as well.

In essence, the MRAC method performance evaluation presented in the previous section is usually focused on determining significant differences both in the attenuation correction factors and bone delineation between CTAC and MRAC and to determine whether these will create significant regional activity differences between CTAC and MRAC reconstructed PET (Bezrukov et al., 2013; Hofmann et al., 2009; Keereman et al., 2013c; Mehranian et al., 2016; Wagenknecht et al., 2013). These criteria are more of a general measure of MRAC performance in regard to quantitative neuro-analysis and evaluation. On the other hand, the impact of MRAC on clinical reading is generally determined by visual analysis, presence of visible artifacts in MRAC or PET, lesion detectability and SUV quantification accuracy in PET (Mehranian et al., 2016). These measures have different error criteria and error tolerance compared to what is commonly conduced in method performance evaluation and comparison.

Recent studies have proposed that standardized, clinical metrics need to be taken into use for MRAC method evaluation, to make direct comparison and summarization of methods less challenging (Rausch et al., 2017; Ladefoged et al., 2017). One such natural criterion would be to suggest would be the accuracy of SUV in terms of quantification and repeatability, which is well-evaluated for whole-body imaging. The impact of MRAC on SUV quantification has been evaluated in a number of clinical studies, which have focused mostly on whole-body PET/MR in oncology. Originally, underestimations of up to 10 % and an overall bias of less than 7 % in lesions have been reported (Hu et al., 2009; Schultz et al., 2011) when using three-class attenuation correction and a mean SUV error of -8 % when using 4-class attenuation correction (Martinez-Möller et al., 2009), in the body with MRAC ignoring bone. All of the authors concluded that these biases would be clinically irrelevant (Mehranian et al., 2016), which is certainly valid for soft tissue lesions. However, for osseous lesions, a large range of bias has been reported by different authors in the range of 5% to 15 % and up to 23 % which could demonstrate that bone cannot be safely ignored if lesions near or in the bone are to be quantified (Mehranian et al., 2016).

Based on the findings of these authors in whole-body PET/MR (Hu et al., 2009; Martinez-Möller et al., 2009; Schultz et al., 2011; Schramm et al., 2011) it could be suggested for brain imaging as well that an SUV bias of 10 % at maximum in soft-tissue lesions could be considered clinically irrelevant. It is interesting to note that several of the proposed MRAC methods for brain PET/MR fall into the range (SUV bias of < 10 %) of this acceptable SUV bias and have demonstrated significant improvements compared to vendor-based implementations of MRAC with no bone. Moreover, several methods claim to achieve a quantitative bias in PET of less than 5 % compared to CTAC reconstructed PET images (Ladefoged et al., 2017). This bias is of the same magnitude as the dose calculation accuracy criteria in radiotherapy planning (5 % error criterion) (Mehranian et al., 2016) and achieves accuracy within the reproducibility of PET (±5%) in terms of PET image quantification (Ladefoged et al., 2017). In a recent study, Ladefoged et al., (Ladefoged et al., 2017b) assessed a segmentation-based MRAC with a large group of neurological patients and defined the absolute error criterion to be within 5 % to be acceptable. Therefore, a tighter error criterion based on these margins of allowing a maximum of 5 % error could be recommended for more advanced applications with a high demand of quantitative accuracy in PET for brain imaging. Although not very recently proposed, Cherry et al., suggested that quantitative errors in the range of 10-30 % in radiotracer modelling studies are often found to be significant and suggested that errors be reduced to below 10 % (Cherry et al., 1995;

Zaidi et al., 2004). In terms of visual accuracy of PET images, recent studies have shown that for ^{18}F-FDG, even a 10 % quantitative error does not hinder visual evaluation and diagnosis (Werner et al., 2016).

Thus, a growing consensus in whole-body, oncologic PET/MR seems to be developing that ignoring bones and tissue variability in three- or four-class MRAC does not significantly impair lesion detectability and in general, the diagnostic confidence of PET findings (Arabi et al., 2015; Martinez-Möller et al., 2009, Mehranian et al., 2016), if no artifacts are present in the MRAC images. It could be argued that the impact of artifacts and inaccuracies in MRAC is expected to decrease when new guidelines and procedures are adopted for PET interpretation and reading (Brendle et al., 2015; Mehranian et al., 2016). Moreover, the diagnostic confidence can be significantly increased by interpreting non-attenuation corrected (NAC) PET images in conjunction of MRAC PET images (Brendle et al., 2015; Mehranian et al., 2016). While the opinion whether bone could be ignored in clinical routine is more divided concerning neurological PET/MR, there have been reports showing that neurological imaging without bone in MRAC might be feasible for clinical routine. A study from Rausch et al., showed no significant change in diagnosis even when an attenuation map without bone was used (Rausch et al., 2017) in brain tumors. Studies of Su et al., (Su et al., 2016) and Werner et al., (Werner et al., 2016) showed that an attenuation map without bone is also sufficient for visual interpretation and clinical diagnosis when using ^{18}F-Florbetapir to determine either amyloid positive or negative status and ^{18}F-FDG in suspected dementia and movement disorders.

Eventually, the accuracy of any MRAC method should be evaluated using clinical criteria along with the non-clinical metrics used in MRAC method performance comparison. In essence, a significant difference concerning MRAC performance in clinical reading could be summarized as a difference which would result in change of diagnosis (true or false positive or negative), which would be due to the use of MRAC alone. Therefore, the next natural step would be to conduct clinical studies with large patient populations to evaluate the applicability, robustness and the quantitative accuracy of MRAC methods in clinical workflow and to differentiate what standardized metrics need to be implemented for evaluation, reading of PET and adoption of new MRAC methods. Evaluating MRAC based on metrics used for diagnostic criteria will therefore play an important role in increasing the clinical applicability and promoting the value of new MRAC methods.

Interestingly, since the introduction of 3D PET, a similar and extensive effort of the scientific PET community was made to introduce a robust method for scatter correction. This effort was finally realized by the modeling of single Compton scatter events in a simulation using measured emission and transmission data. This allowed deriving of an estimation of the spatial location and magnitude of single scattered photons, that is, to calculate their contribution to measured emission data. The physical theory of photon scatter at energies of 511 keV with the theory, practice and implementation aspects behind the single scatter simulation algorithm are discussed in the following paragraphs, as scatter correction has important implications for neurological PET/MR imaging as well.

2.5 Scatter Correction

2.5.1 Physical process of photon scattering in positron emission tomography

Correction of scattered photons is essentially required for quantitative PET reconstruction. Scattering, if neglected causes degradation of image quality, loss of contrast and inaccurate quantification (Bendriem and Townsend et al., 1998). Scatter correction can be considered to be one of the major quantitative corrections implemented in PET reconstruction in addition to attenuation correction. The magnitude of scatter in PET depends on the acquisition mode, the energy window width, the anatomy being imaged and the patient size (Zaidi et al., 2007). In 3D acquisition mode, it is estimated that 30 % to 35 % scatter fraction in brain studies (scattered versus un-scattered photons) can be expected (Zaidi et al., 2004). Before moving into scatter modeling and estimation, physical interactions of 511 keV gamma photons in tissue with regard to the scattering angle, PET energy window setting and the energy of the scattered photon should be shortly reviewed.

In PET, scattering refers to Compton (incoherent) scattering where either one or both emission photons undergo one or multiple interactions with tissue (Zaidi et al., 2004). Other scattering processes such as Rayleigh (coherent) scattering can be neglected due to their relatively small contribution and/or occurrence (Zaidi et al., 2004; Zaidi et al., 2007b). In Compton scattering, the photon 1) changes direction and 2) loses part of its energy. Both of these phenomena are important to for the scatter correction in PET as the first (change of direction) is what calls for correction and the second (energy loss) is what allows removal of the scattered events of too low energy (Zaidi et al., 2004).

The energy E′ of the scattered photon of original energy E after Compton interaction at a scattering angle θ relative to the incoming direction can be written as:

$$E' = \frac{E}{1+E/m_e c^2(1-\cos\theta)}, \tag{7}$$

where m_o is the rest mass energy of an electron and c is the speed of light. It can be seen from (eq. 7) that the energy of the photon decreases at the increasing scattering angle θ. This loss of energy is important to consider as events outside the energy window of the PET acquisition are removed. Thus, the energy window setting serves to eliminate the contribution of scattered photons which are of lower energy than the discriminator setting (Zaidi et al., 2004; Zaidi et al., 2007b). Therefore, only those scattering events captured by the system energy window in the ranges of e.g. 440 keV to 660 keV need to be estimated, modeled and subtracted from the emission data by scatter correction. The formula which gives the probability of a Compton scatter from a free electron through a given angle is the Klein-Nishina equation (eq.8) (Klein and Nishina et al., 1929; Evans et al., 1995; Zaidi et al., 2004).

Thus, this equation is crucial if an accurate representation of the scatter distribution needs to be derived by modeling and simulation of scattered counts. The probability of Compton scattering, i.e the differential scattering cross section $d\sigma/d\Omega$ as a function of scattering angle θ is given by:

$$\frac{d\sigma}{d\Omega} = \frac{{r_e}^2}{2}(1 + cos^2\theta)\left[\frac{1}{1+\alpha(1-cos\theta)}\right]^2\left[1 + \frac{\alpha^2(1-cos\theta)^2}{[1+\alpha(1-cos\theta)](1+cos^2\theta)}\right], \qquad (8)$$

where $\alpha = E/m_0c^2$ and r_e is the classical radius of the electron. As all un-scattered events in PET are assumed to be 511 keV before scattering, $\alpha = 1$ for the first scatter (Zaidi et al., 2004; Zaidi et al., 2007b) and the differential Compton scattering cross section relative to that for un-scattered annihilation photons becomes:

$$\frac{d\sigma}{d\Omega} = \frac{{r_e}^2}{2}\left[\frac{1}{(2-cos\theta)^2}\right]\left[1 + cos^2\theta + \frac{(1-cos\theta)^2}{(2-cos\theta)}\right], \qquad (9)$$

giving the differential scattering probability. The integral of (eq. 9) from 0° to any angle gives the integral cross section, giving information about what fraction of scattered photons will be scattered with a given half-angle. Using these equations, Zaidi et al., (Zaidi et al., 2004; Zaidi et al., 2007b) noted that small-angle scattering is more likely than large-angle scattering and that the most probable scattering angle is around 35°. The corresponding energy of the Compton-scattered photon at this angle is approximately 433 keV, which is within the acquisition energy window of most PET systems (Zaidi et al., 2004; Zaidi et al., 2007b). Thus, the majority of the scatter events needed to be corrected from the emission data are of small-angle scattering.

In general, the purpose of any scatter correction method in PET is to create a representation of the scattered counts (in magnitude and spatial distribution) that corresponds to a particular activity distribution and attenuation map of the object (Zaidi et al., 2004). This distribution is dependent on the size and density of the object and system-related parameters such as geometry, energy resolution, and the PET energy window. Only scattered photons that have undergone a single Compton interaction are modeled as they amount to 75–80% of the scattered coincidences, with the exact percentage depending on the source and attenuator geometries (Watson et al., 1996; Ollinger et al., 1996). Multiple scattering and photons coming from outside the FOV are usually neglected. How these are eventually accounted for depends on the specific implementation of the scatter correction method. It should be noted here that outside FOV scatter is not usually considered a critical issue in ^{18}F-FDG brain imaging as it has more effect in whole-body studies and in specific acquisition conditions using certain radiotracers (e.g. ^{15}O).

Although the gantry, table and other hardware components contribute to scatter, the contribution of such events is neglected, although they may be relevant in physical measurements (Zaidi et al., 2004). It is thus assumed, that the majority of the scattered events are considered to have originated within the patient (Zaidi et al., 2004). Interestingly, a recent simulation study showed that while the majority (85 % to 95 %) of scattered events come from the imaged object (patient, phantom), there is a scatter contribution from the physical hardware components in the range of 5 to 15 % (Hirano et al., 2017). To the best knowledge of the author, no studies have been made so far to evaluate the scatter originating from the fixed hardware components in the PET/MR field of view.

Historically, there have been many approaches for scatter correction in PET imaging. One such approach called the single scatter simulation (SSS) algorithm and presented in detail in the next sections, assumes: 1) scatter is due to single Compton scatter events 2) single scatter distribution can be calculated by application of the Klein–Nishina formula (eq. 8) using the known emitter density and attenuation coefficients from emission and transmission data and 3) the derived scatter estimate can be scaled to the emission data tails for subtraction. Before moving into the details of SSS, scatter correction approaches for PET imaging with focus on SSS are briefly discussed.

2.5.2 Scatter correction approaches in PET imaging

Originally, quite a number of scatter correction methods for PET were proposed in the literature: these which are summarized in the following books and review articles (Bendriem and Townsed et al., 1998; Valk et al., 2003; Zaidi et al., 2006; Zaidi et al., 2001; Zaidi et al., 2004; Zaidi et al., 2007). These methods could be roughly divided into four broad categories: multiple-energy window (spectral-analytic), convolution/deconvolution-based, direct estimation of scatter distribution and statistical reconstruction-based scatter compensation approaches (Zaidi et al., 2004). In addition, hardware approaches such as using coarse septa or beam stoppers made from lead were suggested (Zaidi et al., 2007). Much effort was put into developing approximate scatter correction techniques for 3D PET (Barney et al., 1991; Chen et al., 1998; Adam et al., 1999; Bailey et al., 1994; Cherry et al., 1995; Adam et al., 1998; Zaidi et al., 2000) in addition to investigating the use of full Monte Carlo (MC) methods (Adam et al., 1999; Levin et al., 1995, Holdsworth et al., 2002). MC methods were considered computationally too intensive for clinical routine in PET for years. They have recently re-emerged as graphical processing units (GPUs) which have made it possible to achieve the required computational speed without extensive hardware costs (Gaens et al., 2013). Eventually, two methods based on direct estimation of scatter distribution became most widely adopted, generally denoted as the single scatter simulation (SSS) algorithm of Watson (Watson et al., 1996) and the model-based single scatter approach of Ollinger et al., (Ollinger et al., 1996) which are incorporated as part of the iterative reconstruction loop in PET/CT and PET/MR systems to this day. The specific aspects of the implemented scatter correction method are, however, very vendor-dependent.

The SSS algorithm was originally introduced by Watson et al., (Watson et al., 1996) while a model-based approach based on simulation of single scattered photons was introduced almost simultaneously by Ollinger et al., (Ollinger et al., 1996). Both algorithms approximate the scatter distribution from the volume covered by emission and transmission images. There are considerable differences in implementation of how single Compton scattered events are modeled between these two approaches. The SSS algorithm by Watson et al., does not explicitly account for multiple scatter in the scatter model (Watson et al., 1996), while the approach of Ollinger et al., accounts for multiple scatter by inclusion of a separate model to derive multiple scatter as a convolution of the single scatter distribution (Ollinger et al., 1996). The details of the model-based implementation by Ollinger (Ollinger et al., 1996) with later modifications are described in detail in the following references (Ollinger et al., 1996; Wollenweber et al., 2002; Iatrou et al., 2006, Iatrou et al., 2007). However, for the sake of the context of this thesis, the following sections will focus on the details of the SSS algorithm which are derivatives or extensions of Watson's approach from (Watson et al., 1996).

Considering SSS, while the scattering algorithm kernel is in most components the same as introduced in (Watson et al., 1996), there have been extensions and modifications to the original work which are described in the following references (Watson et al., 1997; Watson et al., 1999; Watson et al., 2004; Watson et al., 2007). The SSS algorithm implementations also vary to some extent across different PET system vendors e.g. comparing the approach of Siemens Healthcare (Watson et al., 2004) to Philips Healthcare (Accorsi et al., 2004) and GE Healthcare (Wollenweber et al., 2002). With the increasing interest in TOF PET, a concept introduced already in the 1980s (Ter-Pogossian et al., 1981), the SSS and the model-based implementation of Ollinger et al., were later extended to TOF imaging (Werner et al.; 2006; Watson et al., 2007; Iatrou et al., 2007) to incorporate TOF-dependent scatter estimates. As multiple scatter interactions are not modeled explicitly by the algorithm in (Watson et al., 1997; Watson et al., 2007) and in (Accorsi et al., 2004), it is assumed that scaling to emission sinogram tails (presented in detail in section 2.5.4) will be sufficient to account for multiple scattering in the data.

This assumption is based on empirical findings that scaling the single-scatter distribution should approximate the multiple scatter distribution present in the emission data, although this relation cannot be proven theoretically (Watson et al., 1997). In addition, this approach has been justified by the use of an appropriate energy window setting, which should eliminate most multiple scattered coincidences which do not have enough residual energy to be registered as true coincidences. The original implementation did not account for out-FOV scatter (Watson et al., 1997), although model-based implementations of (Ollinger et al., 1996) and later implementations of SSS account for this as well (Watson et al., 2004; Accorsi et al., 2004), where both approaches assume that to a certain extent outside the imaged FOV, the spatial distribution and shape of emission and transmission images and scatter beyond the imaged FOV remains continuous. It should be added that out-FOV scatter contribution is usually considered significant for whole-body only.

For estimating the scatter distribution, the approaches based on direct scatter estimation evolve around the following principle: the scatter component in a given LOR can be approximated by simulating the contribution of single Compton scattered events (Watson et al., 1996,;Ollinger et al., 1996; Werling et al., 2002; Accorsi et al., 2004) to that particular LOR by using the emitter distribution from emission images and the measured attenuation coefficients from transmission images with the direct application of the Klein-Nishina formula (eq. 8). This is made computationally feasible by recognizing that the contribution of small scattering regions (scatter sample points) to an LOR passing through the object can be merged into an analytical formula using the Klein Nishina equation (eq. 8) (Watson et al., 1996; Watson et al., 1997; Accorsi et al., 2004). A prerequisite for calculation of the scatter distribution (by spatial location and magnitude) is therefore an estimate of the activity distribution (from emission images) and the attenuation coefficients (from transmission images) in the volume (Ollinger et al., 1996; Watson et al., 1997) and a physical model of photon scattering, detector geometry and acquisition parameters (Accorsi et al., 2004).

The SSS algorithm implementation of Accorsi et al., (Accorsi et al., 2004) is introduced in detail in the following sections for the sake of the context of this thesis.

This is the standard implementation of SSS in the Philips Ingenuity TF PET/MR system. The implementation of Accorsi (Accorsi et al., 2004) compared to Watson's implementation (Watson et al., 1996; Watson et al., 1997) is quite similar, so only their differences are shortly discussed for historical reasons. The model-based implementation of Ollinger (Ollinger et al., 1996) compared to the simulation-based approaches of Accorsi (Accorsi et al., 2004) and Watson (Watson et al., 1996) differ quite much from each other. Therefore, the implementation similarities between Accorsi (Accorsi et al., 2004) and Ollinger (Ollinger et al., 1996) are only discussed in part where the two algorithms overlap. These three algorithms by Watson, Ollinger and Accorsi cover the basis of the PET scatter correction methodologies used by all three PET/MR vendors in modern PET/MR systems (Siemens Healthcare, GE Medical Systems and Philips Healthcare).

2.5.3 The single scatter simulation algorithm

The contribution of scatter can be considered to be additive, adding or misplacing activity to true emission LORs. The contribution of scattering in a volume can be simulated by sub-sampling the volume to scattering points which contribute scatter to emission LORs. This is illustrated for one scatter point in Figure 3. Selecting an emission LOR, simulating the number of events that each scatter point in the volume contributes to that LOR and finally repeating the calculations for the remaining emission LORs allows to estimate the scatter in the volume (Accorsi et al., 2004). This defines the basic assumption of the SSS algorithm: total contribution of single scatter events to an emission LOR can be expressed as the superposition (or volume integral) of the contributions of many scatter points, which are randomly distributed throughout the object (Watson et al., 1996; Watson et al., 1997; Accorsi et al., 2004).

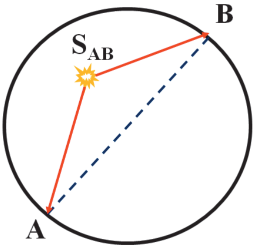

Figure 3. Illustration of contribution of a scatter point S_{AB} (red line) to the emission LOR (dashed line) spanning across two detectors A and B (Watson et al., 2007).

For each emission $\mathrm{LOR_{EM}}$(A,B) between detector A and B, a scatter point S_{AB} adds a number of scattering events which can be estimated. The scatter point S_{AB} contributes a total amount of single scatter events ES_{total}, which can be divided into two distinct contributions: ES_A and ES_B (Watson et al., 1996). ES_A gives the contribution of the emitters from S_{AB} to detector A while ES_B gives the contribution of emitters from S_{AB} to detector B (Watson et al., 1996). The total scatter contribution ES_{total} can then be expressed as:

$$ES_{total} = ES_A + ES_{B,} \tag{10}$$

where the proportional (relative) contribution from ES_A to an emission LOR is expressed below in mathematical form by Accorsi et al., (Accorsi et al., 2004):

$$ES_A \propto \sum_S \varepsilon_A \int_A^S \lambda(x)dx\, \mathrm{e}^{-\int_A^S \mu(x,E_0)dx} \frac{\mu_{c(S,E_0)}}{\sigma}\frac{d\sigma}{d\Omega}\Omega_B \times \mathrm{e}^{-\int_B^S \mu(x,E')dx}\, \varepsilon_B, \tag{11}$$

where S is the scatter point, A and B are the detectors identifying the $\mathrm{LOR_{EM}}$(A,B), λ is the linear activity concentration, x is an integration variable spanning a straight line between integration limits, μ is the linear attenuation coefficient due to all interactions that remove the photon from a straight line as a function of space and energy, E_0 is the energy of the un-scattered photon (511 keV), μ_c is the attenuation coefficient related to Compton interactions, σ is the Klein-Nishina total cross section, $d\sigma/d\Omega$ is the Klein-Nishina differential cross section calculated at an angle spanning across the detectors A and B where scatter point S is the vertex (defined $\angle ASB$), Ω_B is the solid angle under which detector B is seen from S, E' is the energy of the scattered photon and ε_A and ε_B are the factors related to detection efficiency of the detectors. ES_B is analogous, where detectors A and B are interchanged.

Therefore, equations (10 and 11) simply express the possibility of scatter occurring around the scattering point S to be detected by the detector pair A and B (Watson et al., 1996). The probability of detectors A and B detecting the scatter event can be expressed as joint probabilities of: a single Compton scatter event occurring at angle $\angle ASB$ expressed as term ($\frac{\mu_{c(S,E_0)}}{\sigma}\frac{d\sigma}{d\Omega}$), the probability of the photon not having any other Compton interaction between scatter point and detector (terms $\mathrm{e}^{-\int_A^S \mu(x,E_0)dx}$ and $\mathrm{e}^{-\int_B^S \mu(x,E')dx}$expressing attenuation of un-scattered and scattered photon), the probability of positron annihilation between scatter point S and detector A (term $\int_A^S \lambda(x)dx$) and the probability that each of the detectors capture such an event (terms ε_A and ε_B). Although no details are given in the report of Accorsi et al., (Accorsi et al., 2004) about the solid angle factor (Ω_B), we assume it is calculated as the ratio of the cross section of detector B (σ_B) to the distance from the scatter point S to B (R_B), given as ($\Omega_B = \sigma_B/{R_{BS}}^2$). Finally, the total sum of these contributions over all scatter points gives the contribution from ES_A and likewise the contribution from ES_B.

The detection efficiency factors (terms ε_A and ε_B) are calculated as given by (Accorsi et al., 2004):

$$\varepsilon = \frac{1}{\sqrt{2\pi}\sigma_{\Delta E}} \int_{E_{LLD}}^{\infty} e^{-\frac{(E-E_\gamma)^2}{2\sigma_{\Delta E}^2}} dE = \frac{1}{2}\left[1 - erf\left(\frac{E_{LLD}-E_\gamma}{\frac{E_0 \Delta E}{2\sqrt{\ln(2)}}}\right)\right], \tag{12}$$

where $\sigma_{\Delta E}$ is the standard deviation of the Gaussian function modeling the energy resolution of the crystals with a full width half maximum ΔE at 511 keV, E_γ is the energy of the incoming photon and $E_{\gamma LLD}$ is the energy setting of the lower energy discriminator. Dependence of efficiencies on energy, angle of incidence and depth of interaction are not modeled (Accorsi et al., 2004).

The scatter contribution of single scatter events to an LOR is expressed by Watson as a volume integral of scatter points over the scattering object, where the volume integral is estimated by evaluating (eq. 13) at an array of scatter points S_{AB} in the object (Watson et al., 1996). For each combination of sampled emission LOR and a scatter sample point in the object, a scatter contribution to the LOR is computed (Watson et al., 1996). The sum over all scatter points determines the total contribution of scatter to that LOR (Watson et al., 1996). Similarly to (eq. 10), the single-scatter contribution can be expressed as the mean total coincidence rate $R_{scatt} = R_{scatt}(A) + R_{scatt}(B)$ in an LOR for the detector pair (A,B) and scatter point S, where $R_{scatt}(A)$ is (modified from Watson et al., 1996):

$$R_{scatt}^{(A)} = \int_{V_S} \left[\int_S^A \lambda(x)dx\right] e^{-\int_S^A \mu(E,x)dx} \left(\frac{\sigma_A dV_S^{\frac{2}{3}}}{4\pi_{R_{AS}^2}}\right) \times$$

$$\left[\frac{d\mu(E,\Omega_S)}{d\Omega} dV_S^{\frac{1}{3}} \left(\frac{\sigma_B}{R_{BS}^2}\right)\right] e^{-\int_S^B \mu(E',x)dx} \epsilon_A(E)\epsilon_B(E')\ , \tag{13}$$

which is similar to (eq. 11) as we will see in detail.

As in (eq. 11), the first term in (eq. 13) gives the linear activity concentration λ between scatter point S and detector A defined by integration path x. The second term and the fifth exponential terms in (eq. 13) represent the attenuation of un-scattered and scattered photon as in (eq. 11). The third term gives the solid angle factor, giving the cross section for the emitted photons to intersect detector A and the scattering volume dV_s about the scatter point S (Watson et al., 1996). The fourth term gives the probability that a photon entering the volume dV_s from scatter point S in a path to detector A will scatter through an angle Ω_s into the solid angle subtended by detector B (Watson et al., 1996). Finally, the sixth and the seventh terms represent the detection efficiency of detectors A and B for probability of detection for the un-scattered and scattered photon.

Interestingly, no details of the solid angle factor calculation were given in (eq. 11) by (Accorsi et al., 2004) contrary to Watson (Watson et al., 1996), where the third factor in (eq. 13) gives the solid angle factor. Otherwise, as can be seen, with the exclusion of the solid angle factor, both (eq. 11) and (eq. 13) are quite similar. Although (eq. 13) offers a mathematically cleaner presentation, (eq. 11) is easily understandable in algorithm form. The main difference in expression of the contribution of the scatter points by Accorsi et al., (Accorsi et al., 2004) which is described as the sum of the contributions of individual emitter points from the scatter point S to the detector side A in emission $LOR_{EM}(A,B)$ contrary to the volume integral by Watson et al., (Watson et al., 1996). In practice, the volume integral is eventually evaluated by summation over all the selected scatter points by discrete sampling technique (Watson et al., 1996).

Computationally, the most time-consuming task in scatter calculation is the evaluation of the line integrals in (eq. 11), which must be evaluated for each possible ray from the scatter point to the LOR defined between detectors A and B (Werling et al., 2002). Due to the low frequency character of scatter, a coarse set of LORs can be used to reduce the computational load and the sub-sampled scatter estimate can be interpolated to full sinogram space. For practical calculation of the first two line integrals in (eq. 11), the algorithm implementation of SSS by (Accorsi et al., 2004) calculates for each sampled detector pair the efficiency ε_A and solid angle Ω_B, an emission integral $\int_A^S \lambda(x)dx$ and attenuation integral $e^{-\int_A^S \mu(x,E_0)dx}$ evaluated at energy E_0 for a given scatter point S. The minimum of the solid angles is not considered. The line integrals are calculated from expressions in the form:

$$\sum_{i=1}^{N_v} f_i dl_i, \tag{14}$$

where $N_v$is the number of voxels in the path of the photon, f_i is the value of the quantity assigned to voxel i along the integration path and dl_i is the length of the photons' path through the ith voxel (Accorsi et al., 2004). A short description of the algorithm using the energy of the scattered photon (eq. 7), Klein-Nishina equation (eq. 8), scatter contribution (eq. 11) and detection efficiency (eq. 12) follows (Accorsi et al., 2004).

The results of calculation of each integral for the current scatter point are stored and combined in LORs by table lookup method. Afterwards, the scatter angle θ is calculated and entered to the Klein-Nishina differential cross section (eq. 8) and of the energy of the scattered photon (eq. 7). This is used to calculate the attenuation coefficients for scattered photons in the third integral $e^{-\int_B^S \mu(x,E')dx}$ in (eq. 11) and is needed to calculate efficiency ε_B from (eq. 12). The calculation is then executed as a loop over scatter points and contributions to LORs are added accordingly in a lookup table (Accorsi et al., 2004). The final result is a matrix in LOR space, containing the *relative* scatter count rates for each detector pairs. Therefore, the scatter count rates are calculated within a *scaling coefficient.* The calculation of scaling coefficient is addressed in section 2.5.4.

When the scaled scatter contribution is known both in spatial location and magnitude, it must be removed from the emission data. As the physical effect of scattering can be considered to be additive (Watson et al., 1997), where scatter erroneously contributes (or mislocates) activity to true emission LORs, correction operation in the simplest form is subtraction of the simulated scatter distribution from the emission data (Accorsi et al., 2004). To describe this process in algorithmic form, SSS can be implemented as follows (Accorsi et al., 2004); this is the standard method for scatter correction on the Philips Ingenuity TF PET/MR system.

The following steps are conducted during SSS in its most basic version (Accorsi 2004):

1. Define activity and attenuation distribution from the scatter-uncorrected emission and transmission image.

2. Randomly distribute scatter points within the scatter volume.

3. Select an LOR

4. For a given scatter point, calculate the number of events it contributes to this LOR from the following and using (eq. 11):

    - activity distribution estimate,
    - Klein–Nishina cross section,
    - Compton scattering relationships,
    - solid angles,
    - scatter medium distribution.

5. Repeat for all scatter points and add all contributions to the LOR.

6. Repeat steps 3 to 5 for all LORs.

7. Interpolate in LOR space to obtain the scatter sinogram.

8. Scale and subtract the scatter sinogram from the measured sinogram.

9. Reconstruct the image.

To derive accurate shape of the scatter with SSS, assumptions about the nature and consistency of the emission and transmission data need to be made (Ollinger et al., 1996; Watson et al., 1996; Accorsi et al., 2004). These can be shortly listed as follows: 1) the data corrections made to emission data such as randoms, attenuation and dead-time have been performed accurately, 2) most of the emitter activity is contained inside the FOV, 3) the transmission images are complete and accurate, containing the entire scattering object in the FOV, 4) the emission and transmission images are known for most of the regions that contribute scatter to the data.

There are natural limitations in using scatter-uncorrected emission and transmission data for scatter estimation (Watson et al., 1997; Accorsi et al., 2004). These measurements always exhibit a small factor of errors and noise due to the image acquisition and reconstruction process. Another limitation is that the scatter distribution is always derived from a preliminary estimate of the activity distribution reconstructed from scatter-uncorrected data, containing a scatter bias (Werling et al., 2002). One solution to this problem is to iterate the SSS estimate and reuse the emission data from earlier calculations (Werling et al., 2002) as is applied by all of the three methods (Watson et al., 2007; Wollenweber et al., 2002; Accorsi et al., 2004), allowing more accurate scatter estimate. Three iterations have been considered sufficient (Accorsi et al., 2004; Watson et al., 2004; Wollenweber et al., 2002).

Finally, the derived single scatter estimate needs to be scaled to match the emission data (Watson et al., 1996; Ollinger et al., 1996; Werling et al., 2002; Accorsi et al., 2004). In theory, the approximated scatter component can be scaled to the normalized emission data by applying a single scale factor for all tilts and slices although typically slice-by-slice and tilt-by-tilt factors are used (Accorsi et al., 2004). This scaling factor can be determined from comparing the regions of the sinogram (sinogram tails) that contain no direct LOR data, but only scattered (background) events. This region is derived by using an inverse mask of the transmission sinogram, isolating all the emission events located outside the patient contour which are assumed to consist only of purely scattered events (Ollinger et al., 1996; Watson et al., 1996; Accorsi et al., 2004). Thus, all the points used for scatter scaling should be located outside the transmission volume and outside the main activity distribution. Thereafter, the approximated single scatter distribution can be scaled to emission data by solving the appropriate scaling parameters in the form of ($ax + b$) analytically (Accorsi et al., 2004). While tail scaling is the most common approach, methods such as scaling to the normalized emission sinogram (Holdsworth et al., 2002) have been investigated. The sinogram scaling is expected to compensate for the majority of multiple scatter present in the data, as there is no explicit treatment of multiple scatter in the SSS algorithm (Accorsi et al., 2004; Watson et al., 1997). A summary of these scaling methods is described in detail in the following section.

2.5.4 Methods for scaling the SSS derived scatter distribution

The most common method for scatter scaling is tail fitting. An illustration of the tail fitting procedure is shown in Figure 4. The scatter-only regions corresponding to emission sinogram tails are extracted from the emission sinogram data by using a segmented mask from the transmission data (Accorsi et al., 2004; Werling et al., 2002). The mask is created by forward projection of the object contour obtained from the transmission image. In the projection (sinogram) space, a binary mask is obtained where pixels outside the object contour are assigned the value 1 while other pixels are assigned a value of 0 (Accorsi et al., 2004; Werling et al., 2002). The emission data are then masked to exclude the counts contained in the object. The masking operation ensures that only data points from the scatter-only background region of the emission sinogram contribute to the scaling parameters. For added robustness, certain regions close to the patient boundary (<1 cm in Accorsi et al., 2004) or below a certain threshold calculated from the emission data (Watson et al., 2004) can be excluded as well. This is done to ensure that no emission contamination is present in the background region, resulting in over-scaling and over-subtraction.

An appropriate scaling coefficient is usually estimated by least squares fitting between the tails and the scatter sinogram estimate (Accorsi et al., 2004; Werling et al., 2002) or by minimization of an L_1-norm in the scatter-only region (Watson et al., 1996). The scaling procedure was later updated to derive plane-by-plane scaling factors by a weighted least squares fit between scatter sinogram and emission sinogram (Watson et al., 2004). Later implementations also included two options for scaling the scatter sinogram, either relative (tail fitting) or absolute (forward model using initial activity estimate) in magnitude (Heußer et al., 2017), where the latter offers more robustness in terms of over-subtracting scatter but ignores multiple scatter and out-FOV activity. Another approach to reduce the effect of over-subtraction is to set an upper limit (called the “scatter limit”) to the scaling factors of the sinogram tails (Miwa et al., 2015), which has similar limitations to those of absolute scaling. It should be noted that the issues described in (Heußer et al., 2017) and (Miwa et al., 2015) are related to specific conditions in whole-body imaging.

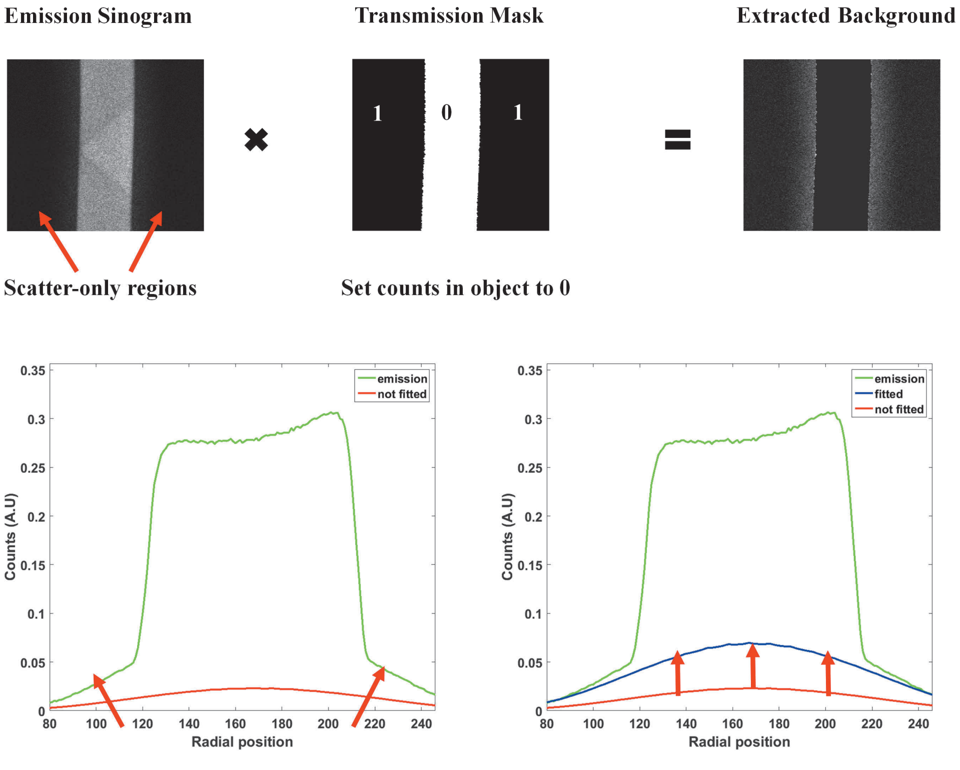

Sinogram tail regions **Estimate scaling coefficient and fit**

Figure 4. A diagram with illustration of the tail fitting procedure with simulated data. The upper row shows how the background regions (sinogram tails) consisting of scattered events are extracted from the emission sinogram. The lower row shows a line profile over the sinogram data, showing how the extracted tails are used to find a scaling coefficient ($ax + b$) for the estimated scatter and the scaled scatter distribution before and after fitting to sinogram tails.

Moreover, plane-by-plane scaling factors can also be averaged across a number of planes for increased robustness in case of poorly segmented or noisy tail data (Accorsi et al., 2004). In the model-based scatter correction of Ollinger (Ollinger et al., 1996), the scaling parameters are calculated based on the integral of the estimated scatter and emission data in the tail region. The later implementations seem to follow this approach by calculating a scaling coefficient from the integral or sum of the emission sinogram tails (Wollenweber et al., 2002; Itarou et al., 2006). Other estimator functions to derive the scaling factor based on the sinogram tails have aslo been investigated (Werling et al., 2002), to increase robustness in case of noise or poorly segmented tails.

In particular, the scatter scaling procedures using the traditional tail fitting methods are sensitive to the quality and consistency of the available emission and transmission data. Tail fitting is more prone to errors if the quality of the extracted emission tails is low. Noise or out-FOV activity increases the background counts in the tail region and the poor quality or segmentation of the transmission map may lead to over-scaling and over-subtraction of scatter. The segmentation quality is a more common issue in whole-body imaging compared to the brain, especially with obese patients or where the transmission data are truncated (Miwa et al., 2015). However, head motion between the emission and transmission scan will have a similar impact on the scatter scaling procedures, especially with radiotracers with high skin accumulation (Mansor et al., 2016).

Alternative methods which would be more robust and less dependent on the quality of the emission tails are thus desirable. One such an approach for scatter scaling is to apply a fast Monte Carlo (MC) simulation (Ye et al., 2014) to derive the scaling parameters instead of fitting to emission tails. The Monte Carlo single scatter simulation algorithm (MC-SSS) derives the scaling parameters by using MC in combination with SSS. The SSS is used to estimate the shape and magnitude of the relative scatter contribution from the emission and transmission data as described previously (Accorsi et al., 2004), while the MC simulation uses the available emission and transmission data to derive an estimate of the true scatter fraction SF during the PET study (Ye et al., 2014).

The contribution of all scatter counts (total scatter, C_S) are expressed using the following equations (Magota et al., 2017):

$$C_S = SF \times C_{EM}, \tag{15}$$

where SF denotes the scatter fraction and C_{EM} denotes the total emission counts in the scatter uncorrected, measured emission data. The contribution of all scatter counts can be also expressed as (Magota et al., 2017):

$$C_S = k \times C_{SSS}, \tag{16}$$

where k is the scaling factor needed to be solved to correctly scale the SSS derived scatter estimate (C_{SSS}) to match the emission data (C_{EM}). Thereafter, the scaled scatter contribution can be extracted from the emission data similarly to the tail-fitted scatter contribution. The two parameters that need to be derived are the scaling factor k and the scatter fraction SF, where the SF can be estimated by MC simulation. As the SSS derived scatter estimate and the emission data are already known, the scaling factor k for C_{SSS} can then be derived using MC simulation from (Magota et al., 2017):

$$k = SF \times \frac{C_{EM}}{C_{SSS}}, \tag{17}$$

where the scatter fraction SF is the scatter fraction calculated from the MC simulation consisting of simulated true counts and scattered counts:

$$SF = \sum C_S / \sum (C_T + C_S), \tag{18}$$

where C_T denotes the true counts without scatter contribution and C_S denotes the contribution of scatter counts. Since only the scatter fraction SF needs to be calculated for estimating the scaling factor, a large number of events is not required in the MC simulation (Ye et al., 2014; Magota et al., 2017). The scaling factor can be specific to a portion of the measured sinograms or global across all the measured sinograms (Ye et al., 2013; Kolthammer et al., 2016).

It is evident that this approach has advantages over traditional tail fitting, as the scaling factor k is no longer dependent on quality, segmentation or noise bias existing in the sinogram tails. However, this method does not resolve any errors already existing in the SSS derived scatter estimate (C_{SSS}) and the emission data (C_{EM}) as it is only intended to alleviate errors in the scatter scaling where traditional tail fitting fails. The SSS derived scatter estimate is affected by the quality of the emission and transmission images used to calculate the scatter estimate (Watson et al., 1997), as seen from (eq. 11) and (eq. 13). The errors in transmission and emission data may therefore be reflected in the amplitude and spatial distribution of the computed scatter profiles, affecting PET image quantification. Thus, scatter scaling will not compensate for the errors that already exist in the shape of the spatial distribution of the computed scatter component (Watson et al., 1997; Werling et al., 2002), although alternatives for scatter scaling are much desired in specific study conditions. Initial reports of the MC-SSS are promising in unique cases which are a challenge to traditional tail-fitting methods such as in ^{15}O gas inhalation studies (Magota et al., 2017).

Moreover, scaling the scatter sinograms to the emission sinogram tails can be challenging due to a multitude of reasons. These include noisy emission data (Werling et al., 2002), which usually lead to over-subtraction of scatter and image artefacts if the scaling factors are overestimated due to the noise in the tails. External scatter may not be completely compensated for in all cases, as it is assumed that most of the activity is contained in the FOV (Watson et al., 2004). Out-FOV scatter may potentially change the emitter distribution inside the FOV, affecting SSS calculation (eq. 11) and thus lead to scatter overcompensation, as the scatter shape is linearly dependent on the magnitude of emitter density (Watson et al., 2004), while the increase of activity in the background (tail) region will affect tail fitting as well. These situations mentioned above are normally not an issue for 18F-FDG brain imaging, but for studies such as O-15 gas inhalation, alternative methods for scatter scaling (Magota et al., 2017) or when to apply or not to apply out-FOV scatter compensation procedures (Hori et al., 2015) should be considered.

However, no extensive evaluations have been performed to investigate the accuracy of scatter correction methods in ^{18}F-FDG brain PET/MR imaging when

MRAC is used. Using MRAC without compensating for attenuation of the skull may theoretically result in changes of scatter amplitude and shape if the attenuation coefficients in MR-based attenuation maps are underestimated. Therefore, assuring how scatter correction accuracy is not affected when using MRAC with or without bone is important for brain PET/MR imaging.

2.5.5 Scatter correction and MRAC

In general, both algorithm implementations of (Watson et al., 1997; Ollinger et al., 1996) assume that the attenuation map used in single scatter estimation would be consistent and free from any significant errors. This creates a logical link between scatter correction and the accuracy of MRAC, as the MR-based attenuation map is used in SSS to derive an estimate of the magnitude and spatial distribution of scatter contribution - the scatter sinogram. However, to the best knowledge of the author, there have been no studies investigating a possible bias of the calculated scatter distribution due to errors in the estimated attenuation coefficients. Ideally, this should be addressed by a simulation study to remove additional factors present in the measured data.

It is assumed that the attenuation coefficients in the transmission sinogram would be accurate to a degree, while in MRAC these attenuation coefficients are generally underestimated. Therefore, one might expect that the accuracy of MR-based attenuation maps has an effect on the accuracy of scatter correction, although at the same time it is worth noting that the scatter simulation is not very sensitive to fine details in the estimated emission or transmission images (Watson et al., 2004). This is due to the inherent smoothness or low frequency profile of the scatter distribution. This is also in part the reason why scatter simulation can be performed using highly under-sampled emission and transmission images, a small set of LORs and quite large voxel sizes within the simulated space (10 mm in Watson et al., 2004).

It is natural to assume that artifacts, high levels of noise or the presence of uncorrected scatter in the data may result in errors in scatter calculations (Watson et al., 1997). These situations are evident in PET/MR imaging if the MRAC images used for attenuation correction include areas void of signal due to implants or truncation, which are more of a problem in whole-body than in the brain. The effects of such errors are also due more to the contribution of incorrect attenuation correction than incorrect scatter correction. Very few reports have been published so far about the accuracy of scatter correction and how MRAC affects it, especially for brain PET/MR imaging. Historically, the work of Zaidi et al., (Zaidi et al., 2003) investigated the use of MRAC for attenuation and scatter correction and concluded that using the method of choice based on MR images would be feasible for such a purpose. Since then, there have been just two reports investigating the relation of MRAC and scatter correction where both (Burgos et al., 2014) and (Merida et al., 2017) concluded that PET quantification errors are mostly due to attenuation and not to scatter correction. Although (Son et al., 2010) did not specifically study the effect of MRAC, they also concluded that the main contributor of errors is attenuation correction and not scatter correction.

Whether the accuracy of SSS and scaling of the SSS estimate could be considered robust for brain ^{18}F-FDG PET/MR imaging using less than optimal MRAC has not been specifically studied. We focus in part on this specific issue in the methodological section of this thesis.

3 AIMS OF THE STUDY

1) To investigate whether MR-based attenuation correction is the largest contributor to the quantitative bias reported in neurological ^{18}F-FDG PET with hybrid PET/MR systems (**Study I**). Our purpose was to show that by implementing a unified and accurate method for attenuation correction by the use of CTAC both in PET/MR and PET/CT systems, the quantitative bias could be minimized to a level where it corresponds to the reproducibility of PET imaging (±5% error). This would imply the following: using either measured attenuation correction from CTAC or TXAC or an approximation of CTAC - an MRAC method with accuracy close to CTAC or TXAC, the quantitative bias between PET/CT and PET/MR systems could be effectively minimized.

2) To develop and implement a new MRAC method (**Study II**) to account for the skull attenuation lacking from the vendor-supplied MRAC of the head region. The method should be effective in minimizing the quantitative bias in PET for ^{18}F-FDG imaging up to the level of SUV reproducibility (< 10 % bias) and should improve the accuracy from the vendor-supplied MRAC implemented on the Ingenuity TF PET/MR system. The requirements for the method should be low enough for standard clinical practice, be viable to use retrospectively as well, with the only prerequisite in having access to T1-weighted MRI data available in the PET/MR system, preferably using the same acquisition as the vendor-supplied MRAC. The method should have a low computational complexity to be implemented as part of the clinical routine (low execution time) and should not require proprietary components or software to be applicable and distributable across multiple PET/MR systems. Thus, any PET/MR user should be able to use, redistribute and modify the method freely by using already available software.

3) In **Study III** the purpose was to develop the method further to achieve quantitative accuracy to a level reported with more advanced methods in the literature, the level of PET reproducibility (< 5 %). Our aim was to improve the accuracy of the method by including additional tissue classes for the brain, allowing us to account for the higher attenuation of brain tissue compared to soft tissues. As continuous attenuation values for bone are considered to improve PET quantification, a continuous tissue class for bone was also added. The requirement would be to achieve PET image quantification accuracy close to acceptable limits of SUV reproducibility (±10%) and fi-

nally, reproducibility of PET imaging (±5%). At the same time, the requirements of study (II) should be preserved to keep the complexity of the method low enough to be applicable for clinical routine.

4) In **Study IV** we investigated the effect of MRAC on the accuracy of scatter correction, particularly by using two methods for scatter scaling, the standard method tail-fitted SSS (TF-SSS) and a prototype Monte Carlo SSS (MC-SSS). Our aim was to investigate whether the quantitative accuracy of PET due to scatter correction is further compromised when an MR-based attenuation map is used in part of the scatter correction estimate. Furthermore, we also set out to investigate whether using an MR-based attenuation map changes the shape or the scaling of the SSS calculated scatter estimate significantly and whether this has a degrading effect on PET image quantification.

4 MATERIALS AND METHODS

Before going into the Materials and Methods of each individual study, a description of the performance of the Philips Ingenuity TF PET/MR system with considerations of the characteristics of the PET image reconstruction, attenuation correction and scatter correction algorithms of the system is shortly given. This is important especially in the light of studies (II, III, IV) and partly study (I). After the introduction of the Ingenuity TF system, we move on to describe the Materials and Methods of each individual study.

4.1 The Philips Ingenuity TF PET/MR

Studies (II, III, IV) were conducted on the Philips Ingenuity TF PET/MR system installed in the Turku PET Centre. The system was also included in the multicenter comparison in Study (I). The Philips Ingenuity TF PET/MR represents the first commercial whole-body hybrid PET/MR system introduced in 2010 (Figure 5). The system consists of a separate MR and PET systems combined with a rotating patient table, allowing sequential acquisition of both MR and PET without moving the patient relative to the patient table. The PET gantry is set 4.2 m apart from the MR system and operates inside the MR scan room. Both PET and MR system hardware have been modified to minimize mutual interference.

Figure 5. Ingenuity TF PET/MR system at Turku PET Centre.

The MR system is based on a Philips Achieva 3T X-series MR, which includes multi-transmit capabilities. The MR system has a maximum gradient strength of 40 mT/M and a slew rate of 200 T/m/s. The PET system is based on a Philips Gemini TF introduced in 2007 (Surti et al., 2007), with TOF capabilities available clinically in static whole-body imaging. The PET system consists of 4x4x22 mm^3 lutetium oxyorthosilicate (LYSO) crystals in 28 detector modules. The bore diameter is 707 mm in PET with a 576 mm transverse and 180 mm axial reconstruction FOV for PET imaging. Compared to the Philips PET/CT systems, reconstruction with a 676 mm transverse PET FOV size is not available in clinical routine. The coincidence window width is 6 ns and the energy acquisition window is 460 to 665 keV. The axial spatial resolution of the system is 4.8 mm. More details are available in the respective performance article (Zaidi et al., 2011).

4.1.1 PET reconstruction of the system

The PET reconstruction system is based on the implementation described in (Wang et al., 2006), although TOF-based reconstruction in the brain could not be applied due to technical limitations in the reconstruction system during the years 2013 to 2017. This mainly concerns the PET data in studies (I to IV). The workflow of the PET reconstruction of the system is explained in detail in (Wang et al., 2006). Although the system was initially marketed by the manufacturer as a TOF-capable system, a vendor-implemented TOF reconstruction is possible only in static whole-body reconstruction protocols unless modifications are implemented on the reconstruction system and the reconstruction protocols.

4.1.2 Vendor-supplied MR-based attenuation correction

The vendor-supplied MRAC of the Ingenuity TF PET/MR system is based on a method described by Schultz and Hu et al., (Schultz et al., 2011; Hu et al., 2009). The method uses a 3D T1-weighted fast field echo (FFE) sequence with echo time of 2.16 ms, repetitition time of 4.18 ms and flip angle of 10 degrees with a total acquisition time of 84 s and an isotropic voxel size of 2 mm. The sequence is intended to produce low-contrast, low-resolution T1-weighted images for attenuation correction purposes only, referred to as attenuation MR (atMR).

In the body region, the method includes segmentation of the patient body in three separate tissue classes depending on the area of interest. The segmentation algorithm is described in (Schultz et al., 2011; Hu et al., 2009). Soft tissues, air outside, air inside (in whole-body studies) and lungs are differentiated as separate tissue classes. For each tissue class a fixed attenuation coefficient is defined as follows: soft tissue (0.096 cm-1), lung (0.022 cm-1), air (0.0 cm-1).

In the head region, the patient head is delineated by image segmentation of the head contour and assignment of a discrete attenuation coefficient of soft tissue (0.096 cm-1) for the entire head contour, ignoring air cavities and bone inside the head region.

Attenuation correction of fixed components in the PET and MR FOV such as the system head coils and the patient bed is implemented by using predefined templates which are added automatically to the attenuation map during PET image reconstruction (Hu et al., 2009). Flexible components of the coils are not compensated in the attenuation map and must be removed from the frontal part of the patient during the PET acquisition to avoid image artifacts. For example, the anterior section of a torso coil can be removed before the PET examination while the fixed posterior section is compensated by an attenuation template.

4.1.3 Implemented scatter correction methods

The SSS algorithm implementations are described in (Accorsi et al., 2004, Wang et al., 2006; Ye et al., 2014; Magota et al., 2017; Werner et al., 2006) for the Philips Ingenuity TF PET/MR system. The SSS algorithm kernel is based on implementation described by (Watson et al., 1996; Watson et al., 1997; Watson et al., 1999; Accorsi et al., 2004), while the scaling of the scatter distribution to emission data is implemented either by tail fitting (TF-SSS) as described in (Accorsi et al., 2004) or by using a fast Monte Carlo simulation (MC-SSS) as described in (Ye et al., 2014). It should be noted here that the MC-SSS on the system is a prototype and not a finished clinical product. The SSS implementation takes into account out-FOV scatter (Accorsi et al., 2004) by extension of scattering points outside the axial field of view (by 16 cm) and has been extended to derive TOF-based scatter estimates (Wang et al., 2006; Werner et al., 2006), although we were unable to investigate the effect of TOF throughout our study due to technical limitations of our reconstruction system.

The TF-SSS relies on extracting the emission tails by using segmented transmission sinograms to identify object boundaries and averages fitting coefficients over adjacent slices (Accorsi et al., 2004). This method has two drawbacks: 1) it is sensitive to noise in the sinogram tails and 2) alignment mismatch between the segmented transmission and emission data, resulting in over-fitting the SSS estimate to true events which causes over-subtraction of scatter. These effects are naturally minimized in high-count, low-noise ^{18}F-FDG data as the quality of the emission tails is high. In addition, registering attenuation maps to the NAC-PET images minimizes any potential alignment mismatch between emission and transmission data. It should be noted that the potential mismatch becomes relevant when it becomes larger than the PET spatial resolution.

The MC-SSS uses a fast Monte Carlo simulation to derive a scaling parameter to scale the SSS derived scatter estimate to emission data (Ye et al., 2014; Magota et al., 2017). The benefit over TF-SSS is that the scaling parameter is no longer dependent on the quality of the emission tails or the accuracy of the tail fitting. In theory, this makes the MC-SSS algorithm more robust to emission-transmission mismatches, noisy emission data or poorly segmented sinogram tails. In these cases, over-subtraction of scatter should no longer occur with MC-SSS compared to TF-SSS (Magota et al., 2017). However, the SSS derived scatter estimate is still used to calculate the scatter distribution in MC-SSS (eq. 17), which means that MC-SSS is still reliant on the quality of the transmission and emission images.

This ends the description of the Ingenuity TF PET/MR system. The following paragraphs describe the Materials and Methods for each individual study from Study I to Study IV in detail.

4.2 STUDY I: Evaluation of the effect of attenuation correction in neurological PET/MR imaging in a multi-center setting

4.2.1 PET/CT and PET/MR phantom study

In study (I), the objective was to determine whether attenuation correction is the largest factor affecting regional quantification between PET/MR and PET/CT systems in a multi-center setting. A phantom study was conducted to investigate the effect of MRAC on the quantitative and visual performance of PET/CT and PET/MR systems in ^{18}F-FDG brain imaging in a controlled manner. CTAC was used as the reference method for attenuation correction on all of the PET/MR systems.

A multi-center study was conducted to investigate the quantitative accuracy between different PET/MR and PET/CT systems, between 4 imaging centers, 4 PET/CT and 3 PET/MR systems. Systems of all major PET vendors (GE Healthcare, Philips Healthcare, and Siemens Medical Systems) were included in the evaluation of both the PET/MR and PET/CT systems. The performance characteristics of each system are referred to in (Delso et al., 2011; Zaidi et al., 2011; Grant et al., 2016; Surti et al., 2007; Bettinardi et al., 2011; Jakoby et al., 2011).

An anatomical 3D printed brain phantom with a dedicated gray matter and a skull compartment was imaged in each center and in each system (Iida et al., 2013). The phantom allows to model a non-pathological uptake of ^{18}F-FDG in the gray matter. The phantom has a realistic head contour, includes air spaces and the attenuation effect of the bone by using K_2HPO_4 solution in a dedicated skull compartment. K_2HPO_4 solution with a concentration of 100 g in 67 g of water has an attenuation coefficient of 0.1514 cm-1 at photon energy of 511 keV, which is close to cranial bone (Dreuille et al., 1997). The main material of the phantom is a transparent photo-curable polymer with a linear attenuation coefficient of 0.101 cm-1 at 511 keV. Therefore, the attenuation of soft tissue, air and bone in the head are simulated.

4.2.2 PET and CT image acquisition

The same phantom was used in three imaging centers (Turku, Zurich, Copenhagen) and a phantom from a different manufacturing batch was used in the 4th imaging site at Sapporo. K_2HPO_4 solution was filled from the same batch at Turku and Zurich, while separate batches were used in Sapporo and Copenhagen. The details of the PET measurements are summarized in Table 2. Each of the measurements was performed in list-mode with a 15 to 20 minute acquisition time.

Anatomical reference images were collected with a separate CT scan in addition to acquiring CTAC for attenuation correction. PET reconstruction parameters are summarized in Table 2. To minimize reconstruction-specific bias between the systems, a static high-iteration dataset was reconstructed to achieve reconstruction convergence and to minimize partial volume effects. To match the reconstruction parameters, TOF and point spread function (PSF) reconstruction were also excluded. Minimal post-filtering to images was applied as all post-filtering was applied in the post-processing phase.

PET/CT attenuation correction was performed with the standard low-dose CTAC using a tube voltage of 120 keV. For PET/MR systems, both the standard clinical MRAC and CTAC were applied in each PET/MR system. Each site applied their own post-processing pipelines for inserting CTAC maps into the PET/MR reconstruction system. In short, these pipelines included segmentation of the phantom volume from CTAC images, registration to PET images, HU value conversion to linear attenuation coefficients by an appropriate bi-linear transform of the system and finally, reconstruction of the corresponding PET images in the PET/MR system.

Table 2. Acquisition and reconstruction details of the phantom study. Modified from Study I. This research was originally published in JNM. Teuho et al., 2016. Effect of Attenuation Correction on Regional Quantification Between PET/MR and PET/CT: A Multicenter Study Using a 3-Dimensional Brain Phantom. JNM. 2016;57:818–824. © by the Society of Nuclear Medicine and Molecular Imaging, Inc.

Acquisition and Reconstruction Parameters							
Institution	**System**	**Activity (MBq)**	**Acquisition duration**	**Algorithm**	**Iterations/ subsets**	**Matrix size**	**Voxel size (mm)**
Turku		97					
	Ingenuity TF	82	15	LOR-RAMLA	10/33	128x128x90	2x2x2
	Discovery 690	48	20	3D-OSEM	10/21	256x256x47	1.38x1.38x3.27
Copenhagen		37					
	mMR	26	15	OP-OSEM	8/21	344x344x127	0.83x0.83x2
	mCT	23	15	OP-OSEM	8/21	344x344x127	0.83x0.83x2
Zurich		78					
	Discovery 690	46	20	3D-OSEM	3/18	256x256x47	1.38x1.38x3.27
	SIGNA	40	20	3D-OSEM	2/28, 10/28	256x256x89	1.17x1.17x2.8
Sapporo		50					
	Gemini TF 64	39	15	LOR-RAMLA	10/33	128x128x90	2x2x2

4.2.3 Quantitative and visual analysis of CT and PET images

All of the PET image data were collected and processed in a centralized manner. An automated PET image processing pipeline was implemented for PET image analysis, to standardize data analysis for each system and each imaging center (Joshi et al., 2009). The pipeline included automatic co-registeration, resolution matching, count-normalization and VOI analysis of PET image data, similarly to neurological PET studies. PET images were co-registered and re-sliced to a reference volume using rigid registration on SPM8. The reference volume was 140x140x140 in size with 1.22-mm isotropic resolution. 3D Gaussian post-filtering was applied for negating the remaining differences due to scanner resolution and image noise, using an 8-mm filter as recommended (Joshi et al., 2009). An automatic VOI analysis was implemented by using eight 3D anatomical VOIs in the phantom gray matter. VOIs were divided into a deep-brain region and 7 cortical regions. Digital phantom data were obtained for reference from the physical phantom (Iida et al., 2013). The digital reference served as the gold standard for visual evaluation. We report the results of the visual analysis in Results section 5.1, Figure 10.

The phantom MRAC, CTAC and PET data were evaluated visually and quantitatively. In visual comparison of MRAC and CTAC, MRAC images were compared with CTAC images at each site. In the quantitative evaluation of CTAC data, the CTAC images were co-registered and re-sliced to the reference volume. Thereafter, HUs were extracted using anatomical VOIs from the PET evaluation. We report the mean HU of each VOI and PET/CT system at each institution in Results section 5.1, Figure 11.

Post-processed PET images were compared using VOI analysis. For each VOI, we evaluated the relative difference %Δ between a target PET system PET_{targ} and a reference PET PET_{ref} system, expressed generally as follows:

$$\%\Delta = \left(PET_{targ} - PET_{ref}\right)/PET_{ref} \tag{19}$$

For PET/CT, a target system $PETCT_{target}$ was compared to three systems $PETCT_N$ located outside the institution. From this, the relative mean difference of a target system to these three systems was calculated as $\%\Delta PETCT_{all}$ defined in:

$$\%\Delta PETCT_{all} = \frac{\sum(PETCT_{target} - PETCT_N)/PETCT_N}{3} \quad N = 1..3, \tag{20}$$

where, for example, a PET/CT in institution 1 was compared to PET/CTs at institutions 2, 3 and 4.

For PET/MRs, a target system was compared to: 1) a PET/CT at the institution 2) three PET/CTs outside the institution. For onsite comparison, the relative difference $\%\Delta PETMR_{onsite}$ of a target system $PETMR_{target}$ to a reference $PETCT_{onsite}$ was calculated as:

$$\%\Delta PETMR_{onsite} = (PETMR_{target} - PETCT_{onsite})/PETCT_{onsite} \tag{21}$$

Then, similarly to, a target system $PETMR_{target}$ was compared to three systems $PETCT_N$ located outside the institution. From this, the relative mean difference of a target system $\%\Delta PETMR_{all}$ to these three PET/CT systems was calculated as:

$$\%\Delta PETMR_{all} = \frac{\sum(PETMR_{target} - PETCT_N)/PETCT_N}{3} \quad N = 1..3 \tag{22}$$

We report the results from (eq. 20) and (eq. 22) for each PET/CT and PET/MR as a function of VOI in Results section 5.1 in Figure 12. We report the results from (eq. 21) for PET/MR as function of the VOI in Results section 5.1 in Figure 13.

Statistically significant differences between VOIs across all systems and between systems across all VOIs were determined by statistical testing using a student's paired t-test with a significance threshold of ($p=0.05$) denoting a statistical significant difference.

4.3 STUDIES II, III and IV

4.3.1 *Subject population*

CTAC, MR and PET data of seven diagnostic patients suspected of memory disorders from a combined PET/CT and PET/MR study were used. All patients gave their informed consent. The data were used for development of a tissue probability-based attenuation correction (TPB-AC) in studies (II and III) and the evaluation of scatter correction in study (IV). The CTAC from PET/CT was used as a reference method for attenuation correction in all of the studies. Patients were administered ^{18}F-FDG depending on their body weight. Median and range of age, weight and dose were: 47 (26-74) years, 77 (47-80) kg and 274 (199-299) MBq, respectively.

All patients underwent a clinical routine PET/CT examination either with the Discovery VCT PET/CT (General Electric Healthcare, Milwaukee, US) or Discovery 690 PET/CT (General Electric Healthcare, Milwaukee, US) in addition to a PET/MR examination on the Philips Ingenuity TF PET/MR system. All CTAC data were collected using the standard low-dose acquisition protocol of 120 keV and 10 mA using dose modulation. All CTAC voxel values were transformed from HU to linear attenuation coefficients in cm-1 by using the transform of Burger et al., (Burger et al., 2002) appropriate for tube energy of 120 keV.

4.3.2 *Vendor-supplied MRAC*

For attenuation correction in clinical studies, the standard atMR acquisition was used for the anatomical MR series, which was automatically segmented inside the PET/MR system vendor-supplied MRAC-algorithm (Hu et al., 2009) to form the MR-based attenuation map used in clinical routine. Attenuation correction of the head coil and the patient table are included automatically within the attenuation correction method.

4.3.3 *PET acquisition details*

All PET/CT and PET/MR acquisitions were performed using the standard protocol for neurological imaging at our institute. The PET/MR PET acquisition was performed with a transaxial acquisition FOV of 256 mm, over one bed position covering the entire head region. The acquisition duration was 15 minutes, while the mean and standard deviation of the scan start times were 80 ± 20 minutes after injection. In three cases, subjects were imaged with PET/CT first and in four cases PET/MR was performed first.

4.3.4 PET image reconstruction

All image reconstructions were performed using LOR-RAMLA with 3 iterations and 33 subsets, matrix size of 128x128x90 and voxel size of 2 mm. All reconstructions included the necessary corrections for image quantification, including randoms, scatter, dead-time, decay and normalisation. The head coil template and patient table are inserted automatically by the reconstruction software if they are connected during the MR image acquisition. Neither TOF nor PSF could be applied due to technical limitations in the reconstruction system.

4.3.5 Attenuation Coefficient Selection

Attenuation coefficient selection for segmentation-based MRAC is a trade-off between bias and variability, if discrete tissue classes are implemented in the attenuation correction method. Therefore, attenuation coefficient selection in studies (II, III and IV) should be briefly discussed.

In study (II), discrete attenuation coefficients were assigned to soft tissue, bone and air. Soft tissue and air were assigned attenuation coefficients of 0.096 cm-1 and 0.0 cm-1, respectively. The bone attenuation coefficients were 0.135 cm-1 and alternatively 0.145 cm-1, which were selected based on the literature search. In accordance with (Catana et al., 2010), a bone value of 0.135 cm-1 was selected with the attenuation coefficient of lowest variance and 0.145 cm-1 as a trade-off between bias and variance (Catana et al., 2010) in addition to its use in a previous study (Anazodo et al., 2015). Additionally, four different attenuation coefficients for bone of 0.135 cm-1, 0.145 cm-1, 0.151 cm-1 and 0.171 cm-1 were tested with a single patient in study (II).

In study (III), a literature review of prior attenuation coefficients reported in different tissues in brain MRAC was conducted based on (Bezrukov et al., 2013; Hofmann et al., 2009; Keereman et al., 2013; Ladefoged et al., 2015; Mehranian et al., 2016; Wagenknecht et al., 2013 and Zaidi et al., 2003b). The results of the literature review are summarized in Table 3. The attenuation coefficients in Table 3 were then used as a theoretical starting point for fixing the attenuation coefficients for each tissue. As can be seen, there is a large variation in attenuation coefficients reported especially for bone. Furthermore, in cases where the attenuation coefficient is reported based on *CT measurements*, care should be taken to confirm which bi-linear conversion curve (Bai et al., 2003; Burger et al., 2002; Carney et al., 2006) is used to derive the reported coefficient.

As this hinders the selection of a proper attenuation coefficient, we performed a measurement of attenuation coefficients in different tissues from a group of 11 patients who had undergone a head MRI and a PET/CT examination. This resulted in the median attenuation coefficients of: 0 cm−1 (air), 0.0956 cm−1 (soft tissue), 0.1521 cm−1 (bone), 0.0989 cm−1 (GM), 0.0983 cm−1 (WM), and 0.0981 cm−1 (CSF) derived based on CT images using the transform of (Burger et al., 2002). These attenuation coefficients were then fixed for each tissue class across the whole patient group.

Table 3. List of most commonly used attenuation coefficients (all units in cm-1) in head MRAC for each tissue class and each MRAC method reported in the literature. Modified from Study III. © 2017 IEEE

Attenuation Coefficients for Different Tissues (cm-1)				
Air	**Skull or bone**	**Soft tissue**	**Brain tissue**	**References**
0.0	0.11 0.13-0.172	0.086-0.093 0.094-0.100	0.095	Bezrukov et al., 2013, Mehranian et al., 2016, Wagenknecht et al., 2013, Keereman et al., 2010
0.000105	0.116	0.086 (soft), 0.064 (fat)	0.096	Malone et al., 2011, Berker et al., 2012, Bezrukov et al., 2013, Mehranian et al., 2016, Wagenknecht et al., 2013
0.003	0.12	0.095	0.099	Berker et al., 2012, Keereman et al., 2010, Bezrukov et al., 2013, Mehranian et al., 2016, Wagenknecht et al., 2013
0.0536	0.136, 0.143, 0.151, 0.157, 0.171, 0.180	0.092 (fat)	0.0993	Zaidi et al., 2003, Catana et al., 2010, Malone et al., 2011, Zaidi et al., 2003
0.054	0.143, 0.152, 0.172	0.094	0.097 (CSF), 0.1 (GM, WM)	Wagenknecht et al., 2013, Berker et al., 2012 Malone et al., 2011,
0.066	0.143		0.096 (CSF), 0.099 (GM, WM)	Malone et al., 2011, Zaidi et al., 2003, Ladefoged et al., 2015
0.06	0.143, 0.151		0.0974 (measured from CT)	Andersen et al., 2014, Berker et al., 2012, Wagenknecht et al., 2013, Zaidi et al., 2003
	0.143		0.098 (observed in brain region)	Wagencknecht et al., 2013, Andersen et al., 2014
	0.0925 (skull base) 0.11 (mastoid process)			Ladefoged et al., 2015
	0.140			Andersen et al., 2014
	0.135, 0.145, 0.151, 0.171			Teuho et al., 2016

In study (IV), the attenuation coefficients for bone, soft tissue and air were selected as 0.151 cm-1, 0.096 cm-1 and 0.0 cm-1 based on the literature (Catana et al., 2010). On the basis of our experience in Studies (II) and (III), we chose 0.151 cm-1 as appropriate attenuation coefficient for the bone and not (0.135 cm-1, 0.145 cm-1 and 0.1521 cm-1) as used in those studies.

4.4 Development of tissue probability-based attenuation correction (TPB-AC)

In study (II), an MRAC method called TPB-AC was developed to improve the attenuation correction provided with the Ingenuity TF PET/MR system. The main idea of TPB-AC is based on using the tissue probability maps derived from segmentation of T1-weighted MRI images given by the New Segement function of SPM8 software. This allows to derive a subject-specific attenuation map including soft tissue, air and bone by using the standard T1-weighted atMR acquisition of the PET/MR system. The purpose of the study was to validate the method in comparison against CTAC and vendor-supplied MRAC and to show that TPB-AC offers superior accuracy compared to vendor-supplied MRAC by adding bone to the attenuation map.

The segmentation of the T1-images is based on the New Segment function in SPM8 (and potentially SPM12) to derive the tissue probability maps. The New Segment function combines affine registration to the International Consortium for Brain Mapping (ICBM) Tissue Probabilistic Atlas and image segmentation based on the Unified Segmentation principle described in (Ashburner et al., 2005). Bias field correction is included to account for MR image intensity non-uniformities for improved segmentation accuracy (Ashburner et al., 2005).

To briefly describe Unified Segmentation, the intensity distribution of tissue types in the input MR image is determined using a mixture of Gaussians model and spatial priors from the ICBM Atlas of T1-weighted images (Ashburner et al., 2005). The segmentation result is a series of tissue probability maps, where a voxel corresponds to a probability between 0 and 1 of a particular tissue type to exist in that particular voxel (Ashburner et al., 2005). Probabilities are distributed across the maps in such a way that the total sum of tissue probabilities in a voxel over all maps is always one (Ashburner et al., 2005).

The tissue probability maps are readily given as a result of the segmentation by the New Segment function and represent: gray matter (GM), white matter (WM), cerebrospinal fluid (CSF), scalp, skull and air. In study (II), we used only the scalp, skull and air while in study (III), additional tissue classes for the brain were implemented using GM, WM and CSF tissue classes. An example of the T1-weighted MR and the non-processed probability maps is shown in Figure 6 for reference.

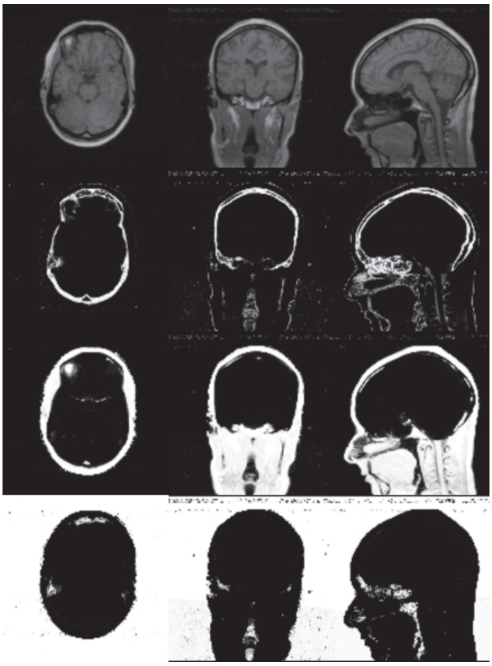

Figure 6. Anatomical MR image used for segmentation (top 1st row) with the non-processed tissue probability maps for bone (2nd row), scalp (3rd row) and air (4th row) from the New Segment function of SPM8. The tissue classes are well-separable. Modified from Study II. © 2016 IEEE

The tissue probability maps need to be post-processed to be usable for MRAC. One of the main goals of study (II) was to implement an image processing pipeline to create an MR-based attenuation map. In this way, patient data could be processed in an automated fashion. Image segmentation and filtering procedures to derive the final attenuation map were performed using the commonly available functions in image and signal processing toolboxes in MATLAB. The final workflow of the method used in study (II) is shown in Figure 7.

Discrete tissue volumes as logical binary masks for each tissue are derived from the probability maps by a simple threshold operation. This value achieved a good delineation of bone, air and soft tissue volumes in each individual mask. The only processing applied after thresholding operation to air volume is de-noising. The soft tissue volume for the head is derived by morphological closing and flood-fill operation, resulting in a uniform head volume. The skull volume is extracted by finding the largest connected structure in the skull mask by connected component analysis. Finally, a filtering step is applied to remove residual noise.

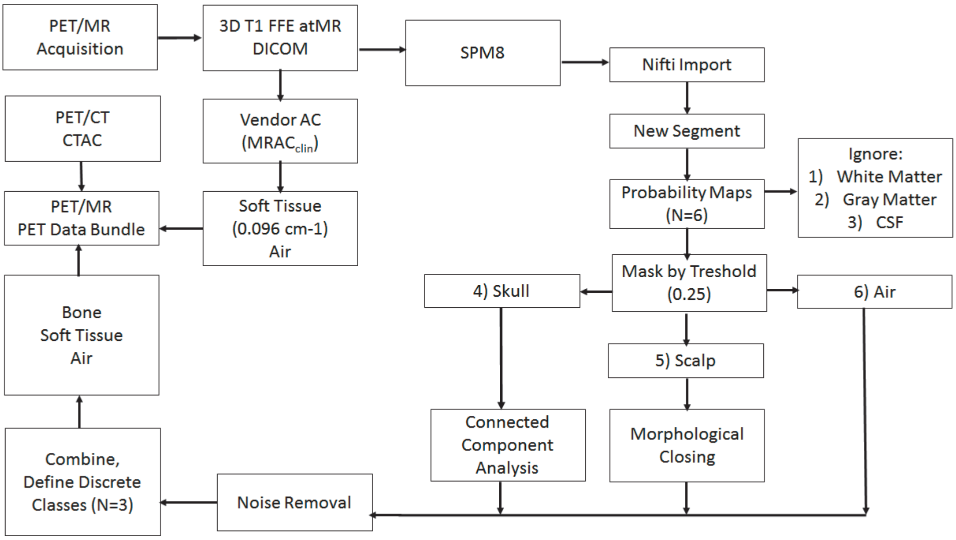

Figure 7. Workflow of the MRAC method used throughout study (II). Bone and soft tissue attenuation values can be modified freely. Modified from Study I. © 2016 IEEE

Attenuation coefficients are assigned when combining the masks to form the final three-class attenuation map. The assignment of bone values in studies (II and III) is discussed previously (section 4.3.5). The final step of the processing pipeline is to combine the tissue masks. Skull and soft tissue volumes are combined by a logical indexing operation. First, the whole soft tissue volume is assigned a value of 0.096 cm-1. Thereafter, the skull volume is added by assigning a discrete attenuation coefficient of bone for all voxels where the skull mask equals a value of 1. In this study, values of 0.135 cm-1 and 0.145 cm-1 were used for bone. Third, air is included by a logical indexing operation, where any structures with the value of 1 in the air mask are assigned the attenuation coefficient of air.

4.4.1 Using TPB-AC and CTAC mu-maps in the PET reconstruction

The TPB-AC attenuation maps were re-aligned, resolution matched and co-registered to vendor-supplied MRAC using rigid image registration and normalized mutual information in SPM8. The CTAC was converted from HU values to linear attenuation coefficents by using a bi-linear transformation appropriate for tube energies of 120 keV (Burger et al., 2002). All off-line attenuation maps were smoothed to a PET resolution of 5 mm FWHM by spatially invariant Gaussian filtering as described in (Schramm et al., 2013). This is performed to ensure that the resolutions of PET and implemented attenuation maps match. If the attenuation map resolution differs from the PET resolution significantly, artifacts will occur (Khalife et al., 2017; Meikle et al., 1993).

4.4.2 Method validation

The relative differences between attenuation coefficients in CTAC and TPB-AC attenuation maps were compared by VOI analysis, where three tissue volumes consisting of whole head, skull and soft tissue VOIs were automatically segmented. The attenuation coefficients from these tissue volumes were extracted from co-registered CTAC and TPB-AC attenuation maps for the whole head, skull and soft tissue. The relative difference between attenuation coefficients in CTAC (μ_{CTAC}) and TPB-AC (μ_{TPB-AC}) was calculated using:

$$\%\Delta = \frac{\mu_{TPB-AC} - \mu_{CTAC}}{\mu_{CTAC}} * 100 \tag{23}$$

We report the mean difference from (eq. 23) and the R^2 value from the head region in Results section 5.2.

The PET images were evaluated quantitatively, using an atlas-based automatic VOI analysis and comparison of regional cross-correlation, using CTAC reconstructed PET data as a reference. Automatic analysis employed a well-established anatomical atlas image provided in automated anatomical labeling (AAL) software (Tzourio-Mazoyer et al., 2002), using 28 VOIs. Individualization of the atlas was based on the spatial mapping from the Montreal Neurological Institute (MNI) space to individual space as provided by Unified Segmentation in SPM8. Finally, the atlas image was masked in the individual space using a binary grey matter probability map with a lower threshold of 0.5. The mean relative difference between CTAC, TPB-AC and vendor-supplied MRAC in addition to regional standard deviation were calculated using:

$$\%\Delta = \frac{PET_{MRAC} - PET_{CTAC}}{PET_{CTAC}} * 100\,, \tag{24}$$

where PET_{CTAC} denotes PET activity values in CTAC reconstructed PET and PET_{MRAC} denotes PET activity values in TPB-AC or vendor-supplied MRAC reconstructed PET, respectively. The mean relative difference and standard deviation are reported in Results section 5.2, Table 4. The results from the cross-correlation analysis is given in Results section 5.2, Figure 15.

Finally, to evaluate the computational efficiency of the method, several cycles of the processing chain were run on an Intel Core i3-4130 with 4 GB of memory and 32-bit Windows 7 OS running MATLAB 2011a and SPM8. For each cycle, the time to create the tissue probability maps in addition to post-processing time was measured. We report the mean computational time of the measurements in Results section 5.2.

4.5 Further development of TPB-AC by addition of brain tissue classes and CT-template based continuous bone

In (Study III), the method developed in (Study II) underwent further development to include separate tissue classes for the brain and continuous bones for the patient skull and optionally, the patient sinus cavities. The purpose was to improve the method by accounting for additional tissue classes for the brain and to add continuous attenuation values to the skull. Potentially, this would allow to achieve a level of quantitative accuracy in PET feasible for kinetic modelling and other demanding applications (< 5 % and < 10 % error). A thorough analysis of the method performance against CTAC data was performed.

Several modifications for the TPB-AC method processing pipeline were implemented, which are described in detail in Figure 8. Two main modifications can be summarized as follows: 1) a CT template can be registered to individual anatomy by non-linear registration in SPM8, allowing the inclusion of a continuous skull and/or nasal sinuses 2) brain tissues (GM, WM, CSF) can be included in the attenuation map as individual tissues (6-class attenuation map), mean of the three brain tissues (4-class attenuation map) or by combination of GM and WM with a separate class for CSF (5-class attenuation map).

4.5.1 Implementing a continuous skull and sinuses from a CT template

For the CT template, we used a freely available, modern, open-source CT template for SPM8, originally developed by Rorden et al., (Rorden et al., 2012). The CT template was converted from HU to attenuation coefficients by using the transform of (Burger et al., 2002). Some additional processing is required to registration for the template to each individual subject, as described below.

The inverse transformation of the CT template from MNI space to individual space was carried out using the deformation fields given by the New Segment function of SPM8, performed by using the Deformation Utility in SPM8. This resulted in a wrapped CT template (wCT) matching the individual subject anatomy. To extract the skull from wCT, the discrete skull mask was dilated by using a structuring element in the shape of a disk with a radius of two pixels. Thereafter, the sinus region can be included by either using the entire skull from masked wCT or by assigning a discrete attenuation coefficient with an additional sinus mask.

To create discrete sinuses, the skull from the wCT was segmented out by a threshold of 0.125 cm-1, and dilated by a disk of radius of 3 pixels, resulting in a binary mask. This binary mask contains only the skull region in wCT as the attenuation values in the sinus region are below the threshold of 0.125 cm-1. This binary skull mask was then extracted from a binarised bone probability map. The largest binary component was then extracted by connected component analysis with three-dimensional regional connectivity of 6 voxels, resulting in a binary mask of the sinus region. This mask was used to assign a custom attenuation coefficient to the sinus region.

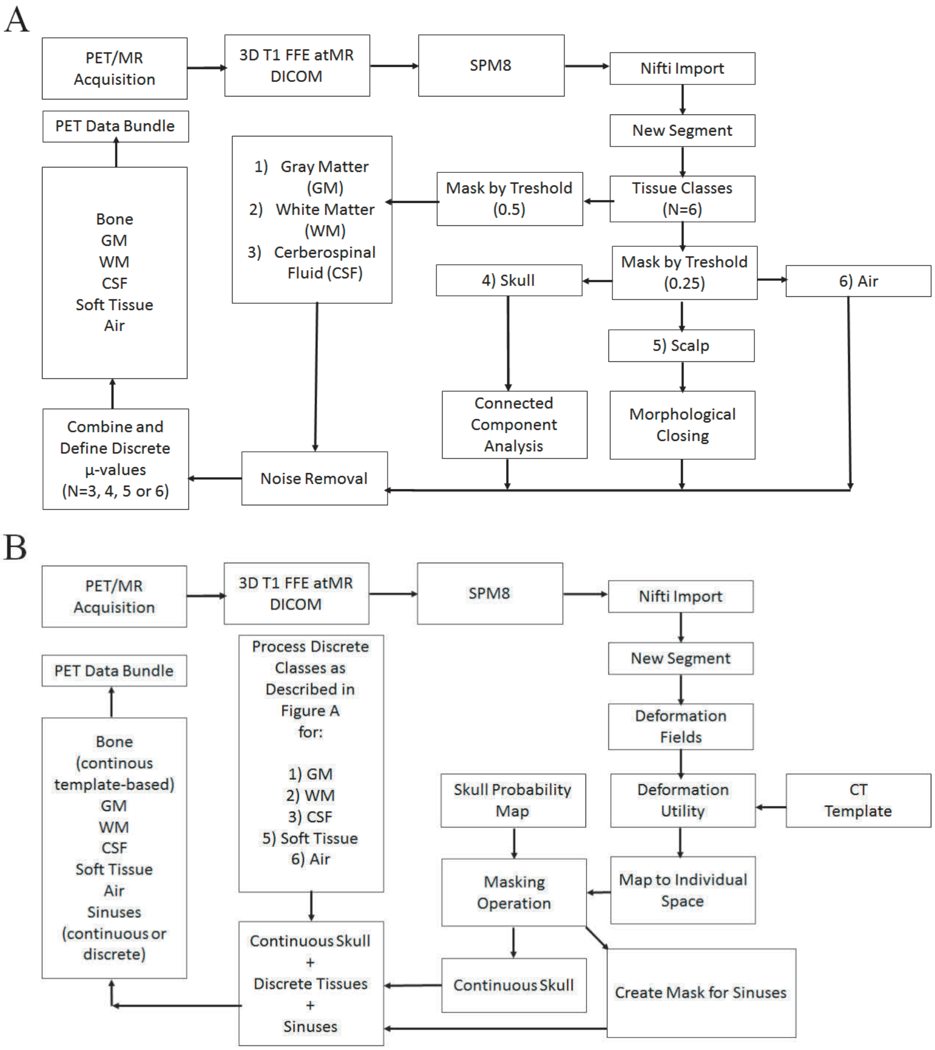

Figure 8. Workflow of deriving MR-based µ-maps with either (A) discrete segmentation-based or (B) continuous template-based skull. The additional discrete tissue classes of GM, WM, CSF, soft tissue, and air are processed similarly in (A) and (B). The sinus mask in (B) is optional, allowing the sinuses to be included by either MR-based segmentation (discrete sinuses) or by the CT template (continuous sinuses). The attenuation coefficients in the discrete tissue classes can be modified freely. Modified from Study III. © 2017 IEEE

4.5.2 Implementing brain tissue classes

The MR images were segmented with the New Segment as in (Study II) and a modified processing pipeline described in (Figure 8) was implemented. The GM, WM, and CSF masks were converted to logical binary masks. The brain tissue masks were then combined individually to the final attenuation map by logical indexing operation before segmenting out air. In the 4-class attenuation map, a single brain tissue class consisting of the mean value of GM, WM, and CSF (0.0985 cm−1) was used. In the 6-class μ-map, the attenuation coefficients for GM (0.0989 cm−1), WM (0.0983 cm−1), and CSF (0.0981 cm−1) were assigned individually. Optionally, a 5-class attenuation map can be created from GM + WM (0.0989 cm−1) and CSF (0.0981 cm−1), although we did not evaluate it in this study.

4.5.3 MRAC and CTAC Image Reconstruction

The MRAC and CTAC maps were imported to PET/MR reconstruction similarly as in (Study II). To minimize any errors that might cause an attenuation mismatch (e.g., by patient motion) due to the sequential nature of our PET and MR system, both the CTAC and MRAC images were realigned and co-registered to non-attenuation corrected PET images using rigid image registration with normalized mutual information in SPM8.

4.5.4 Method Comparison

The similarity between CTAC and MRAC was compared by dice coefficient analysis. The dice coefficient was calculated as follows from co-registered MR-based and CT-based attenuation maps:

$$Dice\ coefficeint = \frac{2|CTAC \cap MRAC|}{|CTAC|+|MRAC|}, \tag{25}$$

where CTAC denotes the tissue volume segmented from CTAC and MRAC denotes the tissue volume segmented from MRAC. The tissue volumes were segmented using the following ACFs as threshold: air (μ < 0.05 cm−1), soft tissue (0.05 cm−1 < μ < 0.11 cm−1), brain tissue (0.097 cm−1 < μ < 0.11 cm−1), and bone (μ > 0.11 cm−1) (Kops et al., 2015), which were then evaluated for similarity. The results from (eq. 25) are reported in Results section 5.3.

The PET data reconstructed using MRAC were evaluated quantitatively by regional VOI and ratio image analysis against CTAC reconstructed PET data. VOI analysis was performed using anatomical atlas provided in AAL software and a total of 35 anatomical VOI. The names of the anatomical regions are included in Appendix, Table I. Individualization of the atlas was based on the spatial mapping from the MNI space to individual space as provided by Unified Segmentation in SPM8. Finally, the atlas image was masked in the individual space using summed tissue probability maps from GM, WM, and CSF with a lower threshold of 0.5.

For each VOI, the mean relative difference and the mean absolute difference were calculated between CTAC and MRAC reconstructed PET, in addition to regional standard deviation. The relative difference was calculated as:

$$\%\Delta = \frac{(PET_{MRAC} - PET_{CTAC})}{PET_{CTAC}} * 100 \qquad (26)$$

where PET_{MRAC} denotes the activity measured from MRAC reconstructed PET with different MR-based attenuation maps, while PET_{CTAC} denotes the activity measured from CTAC reconstructed PET. The results from (eq. 26) are reported in Results section 5.3, Figure 18 and Figure 19. The mean absolute difference was calculated as:

$$|\%\Delta| = \frac{|PET_{MRAC} - PET_{CTAC}|}{PET_{CTAC}} * 100. \qquad (27)$$

The results from (eq. 27) are reported in Results section 5.3, Figure 19.

In the ratio image evaluation, mean and standard deviation “bias atlas” images were calculated for each MRAC method as described by Ouyang et al.,. (Ouyang et al., 2013) across the patient group for each MRAC method, respectively. Ratio images were masked by using summed tissue probability maps from GM, WM, and CSF with a lower threshold of 0.5. This allowed us to study the bias in each method in a pixel-wise analysis. The results of the ratio image analysis are reported in Results section 5.3, Figure 20. Finally, the computational efficiency of the modified method was re-evaluated as described in Study (II) to ensure that the processing time of the method did not increase significantly.

4.6 Evaluation of scatter correction accuracy when using MRAC

In the final part of the study (Study IV), a phantom and patient study was conducted to investigate the effect of MRAC on scatter correction in PET. We investigated the effect of different MRAC methods on the shape, the scaling and the quantitative accuracy of PET when using SSS derived scatter estimates. Two different methods for scatter sinogram scaling with three different attenuation maps (CTAC, MRAC with bone, MRAC without bone) were evaluated.

4.6.1 Patient MRAC

The subject population with the PET acquisition and reconstruction parameters are described previously in section 4.3.1. Three attenuation maps were used to evaluate the effect of MRAC on the performance of scatter correction in the patient study. For MRAC, a 3-class attenuation map with bone ($MRAC_{3class}$) and a 2-class attenuation map without bone ($MRAC_{2class}$) were used. CTAC was used as the reference method for attenuation correction.

$MRAC_{3class}$ and $MRAC_{2class}$ for patients were created using a method described in Study (II). $MRAC_{3class}$ was created similarly as in Study (II) while $MRAC_{2class}$ was created by replacing the voxels inside the skull with soft tissue, therefore ignoring the higher attenuation of the patient skull. The attenuation coefficients in the patient study were assigned as follows: air (0.0 cm-1), soft tissue (0.096 cm-1) and bone (0.151 cm-1) (Catana et al., 2010). For creating a reference CTAC, the head of each subject was carefully segmented out by semiautomatic regional contouring tools in Carimas 2.8 (Turku PET Centre, Turku, Finland). Thereafter, the CT HU values were converted to attenuation coefficients by a bi-linear transformation (Burger et al., 2002).

4.6.2 Phantom evaluation

A phantom scan was performed to complement the patient data. A standard NEMA scatter phantom and a 3D printed anatomical brain phantom (Iida phantom) were used (Iida et al., 2013). The NEMA scatter phantom was placed approximately 8 cm apart from the brain phantom to simulate scatter originating from the patient body in a clinical brain scan. Phantoms were fixed by straps to prevent motion in the MR and PET scans. Foam pads were used to support the phantom head on the bed.

The phantom measurements were done on the same PET/MR and PET/CT systems as the patient scans, using a similar scan protocol for PET, MR and CT. All PET scans were performed in list-mode, with scan duration of 15 minutes without a head coil on the PET/MR. Afterwards; the phantom was transferred to the PET/CT, where a standard low-dose CTAC using a tube voltage of 120 kV was collected for reference method for PET/MR attenuation correction.

The brain phantom gray matter compartment was filled with 40 MBq of radioactivity in 750 ml of water while the NEMA scatter phantom was filled with 105 MBq of radioactivity from the same batch. The brain phantom skull compartment was filled with a K_2HPO_4 solution supplied with the phantom, with a concentration of 100 g of salts in 67 g of water. A gamma counter (1480 Wizard 3”, Perkin Elmer, Turku, Finland) was used to determine the absolute activity concentration in the brain phantom at the PET/MR scan start time. Finally, the attenuation coefficients of the phantom skull were measured from the acquired CT images.

The MR-based attenuation maps for the phantom were created using MATLAB2011b (Mathworks Inc. Natick, US) and in-house software. $\mathrm{MRAC}_{\mathrm{2class}}$ was created by assigning an attenuation value of soft tissue (0.096 cm-1) for the entire phantom volume segmented from CTAC. To create $\mathrm{MRAC}_{\mathrm{3class}}$, bone was added by segmentation of the phantom skull from the CTAC and assignment of a discrete bone attenuation coefficient to the region of the skull. The bone was assigned an attenuation value of 0.128 cm-1, as measured from the CT scan. CT-based attenuation maps were created by segmenting out the phantom from the CTAC and by conversion of Hounsfield unit values to attenuation coefficients (Burger et al., 2002). Example attenuation maps of the phantom are presented in Figure 9.

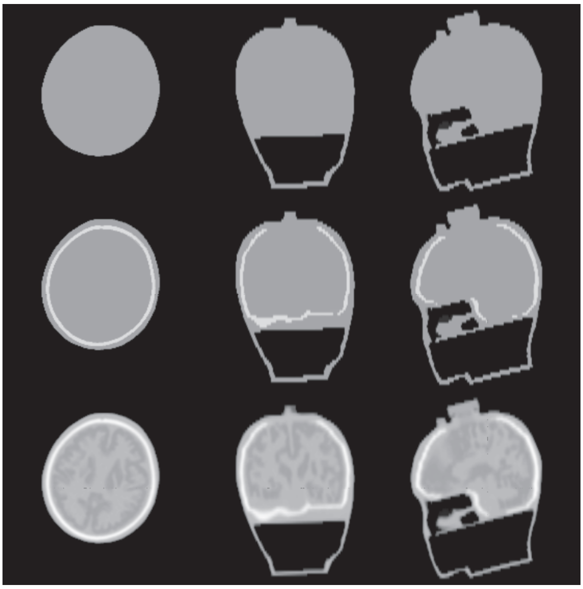

Figure 9. Visualization of CT- and MR-based attenuation maps of the phantom. $\mathrm{MRAC}_{\mathrm{3class}}$ and $\mathrm{MRAC}_{\mathrm{2class}}$ are presented in 1st and 2nd row while the CT-based attenuation maps are presented in the 3rd row. The window level between the phantom images is set to be the same based on the minimum and maximum value of the CT. This research was originally published in JNM. Teuho et al., 2017. Quantitative Evaluation of 2 Scatter-Correction Techniques for 18F-FDG Brain PET/MRI in Regard to MR-Based Attenuation Correction. JNM. 2017;58:1691-1698. © by the Society of Nuclear Medicine and Molecular Imaging, Inc.

4.6.3 PET image reconstruction and scatter correction

PET images were reconstructed using tail fitted SSS (TF-SSS) and Monte Carlo SSS (MC-SSS). For both scatter correction methods, three attenuation maps were used: CTAC, $\mathrm{MRAC}_{3\mathrm{class}}$ and $\mathrm{MRAC}_{2\mathrm{class}}$. All reconstruction parameters were fixed between TF-SSS and MC-SSS reconstructions, which are summarized in section 4.3.4. Reconstructions of the clinical subjects included the head coil template and the patient table, inserted automatically by reconstruction software. The phantom image reconstructions included only the patient table since no head coil was present. This was done to minimize the scatter originating from hardware components for creation of reference data, although this would not simulate the actual patient condition. All attenuation maps were registered to non-attenuation corrected PET images for best possible registration before image reconstruction. All attenuation images were smoothed to native PET resolution of 5 mm as in (Schramm et al., 2013).

4.6.4 TF-SSS and MC-SSS scatter sinogram analysis

Sinograms from TF-SSS and MC-SSS were extracted from the PET reconstruction system. The randoms-corrected emission, transmission and the final scatter sinogram from TF-SSS and MC-SSS were extracted. Sinogram radial profiles were then inspected. The profiles were averaged over all tilt angels (N=7) and drawn over central axial bin and phi angle. The results of the analysis are presented in the Results section 5.4, in Figures 21 and 22. For each method, the total scatter fraction $\mathrm{SF}_{\mathrm{tot}}$ from the measured sinogram data for the phantom and subjects was calculated as:

$$SF_{tot} = \sum_{i=0}^{n} C_{scatter} \,/\, \sum_{i=0}^{n}\left(C_{prompt} - C_{delay}\right), \tag{28}$$

where $C_{scatter}$ are the counts in the scatter sinogram, C_{prompt} are the counts in the prompt sinogram and C_{delay} are the prompts in the randoms sinogram calculated from delays. The results from (eq. 28) are presented in Results section 5.4..

4.6.5 Quantitative evaluation of phantom PET images

Quantitative assessment of absolute activity recovery in addition to regional VOI assessment was performed. Absolute activity recovery was measured with a single VOI covering the phantom gray matter volume from CTAC reconstructed PET images. Thereafter, the radioactivity from phantom PET images (A_{meas}) was measured and the recovery coefficient (%RC) against the value measured from the gamma counter (A_{calib}) was calculated as:

$$\%RC = \frac{A_{meas}}{A_{calib}} \times 100\%. \tag{29}$$

The results from (eq. 29) are presented in Results section 5.4, in Table 5.

4.6.6 Quantitative PET image evaluation of the clinical subjects

PET images were quantitatively evaluated by VOI assessment of regional radioactivity and by ratio image analysis for visualizing regional differences. The quantitative analysis was performed by using MATLAB2011b and SPM8. VOI analysis was performed automatically, employing an anatomical atlas from AAL software, using 35 cortical VOI (Appendix, Table 1) in the brain. Individualization of the atlas was based on the spatial mapping from the Montreal Neurological Institute space to individual space using Unified Segmentation in SPM8. The atlas image was masked in the individual space using summed tissue probability maps from Unified Segmentation from GM, WM and CSF with a lower threshold of 0.5.

The relative difference between TF-SSS and MC-SSS reconstructed PET images was assessed. The mean relative difference %Δ between TF-SSS and MC-SSS, with regional standard deviation was calculated for each VOI and for each attenuation map used in PET reconstruction. The mean relative difference %Δ between TF-SSS and MC-SSS was calculated for each VOI and attenuation map as:

$$\%\Delta = (PET_{MC-SSS} - PET_{TF-SSS})/PET_{TF-SSS}. \tag{30}$$

The results from (eq. 30) are reported in Results section 5.4, Figure 23.

Like in to Study (III), mean PET images across the whole study group were derived, from which the mean ratio images (eq. 26) across all subjects were calculated for TF-SSS and MC-SSS with all attenuation maps. The mean PET images were calculated from PET images normalized to MNI space in SPM8. The mean ratio images are showin in Results section 5.4, Figure 24. The mean PET images are shown in Results section 5.4, Figure 25.

5 RESULTS

5.1 Study I

Visual and quantitative differences between the PET/CT and PET/MR systems could be effectively minimized by using a standardized method for attenuation correction across the systems. This is well seen from Figure 10, which shows that when using CTAC for the attenuation correction method, all PET/CT and PET/MR systems follow the appearance of the digital reference. Reconstructed images are fairly well reproducible across different systems.

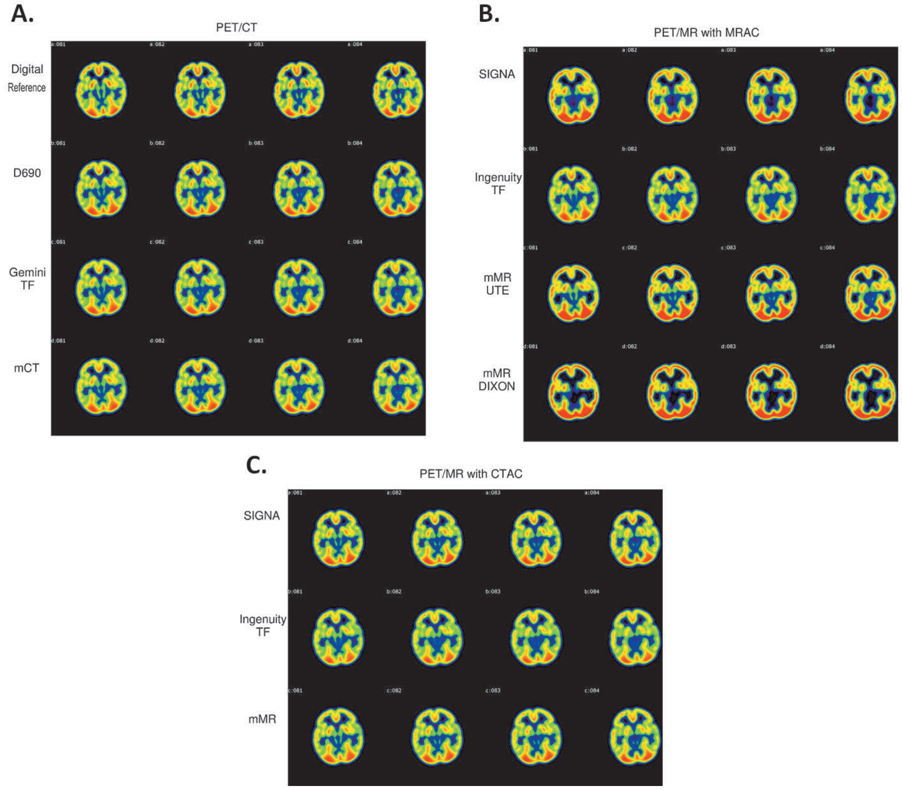

Figure 10. PET/CT and PET/MR images with the digital reference using CTAC and MRAC. (A) Digital reference and PET/CT images. (B) PET/MR images with MRAC. (C) PET/MR images with CTAC. The segmentation-based errors in MRAC corrected PET are evident, with the exception of Ingenuity TF, which provided nearly artifact-free MRAC among the PET/MR systems. CTAC brings PET/MR into agreement with the PET/CT and the digital reference. Modified from Study I. This research was originally published in JNM. Teuho et al., 2016. Effect of Attenuation Correction on Regional Quantification Between PET/MR and PET/CT: A Multicenter Study Using a 3-Dimensional Brain Phantom. JNM. 2016;57:818–824. © by the Society of Nuclear Medicine and Molecular Imaging, Inc.

Considering the possible range of HU from -1000 to 1000 and more, the HU values measured in the 8 VOI and shown in Figure 11 varied only slightly between the PET/CT systems. In particular, the VOI values in mediofrontal cortex, lateral frontal cortex, cerebellum, and parietooccipital cortex were consistent institution-wise. Differences were seen only in the Copenhagen and Sapporo measurements. However, in the range of the HU scale, these differences can be considered to be minor.

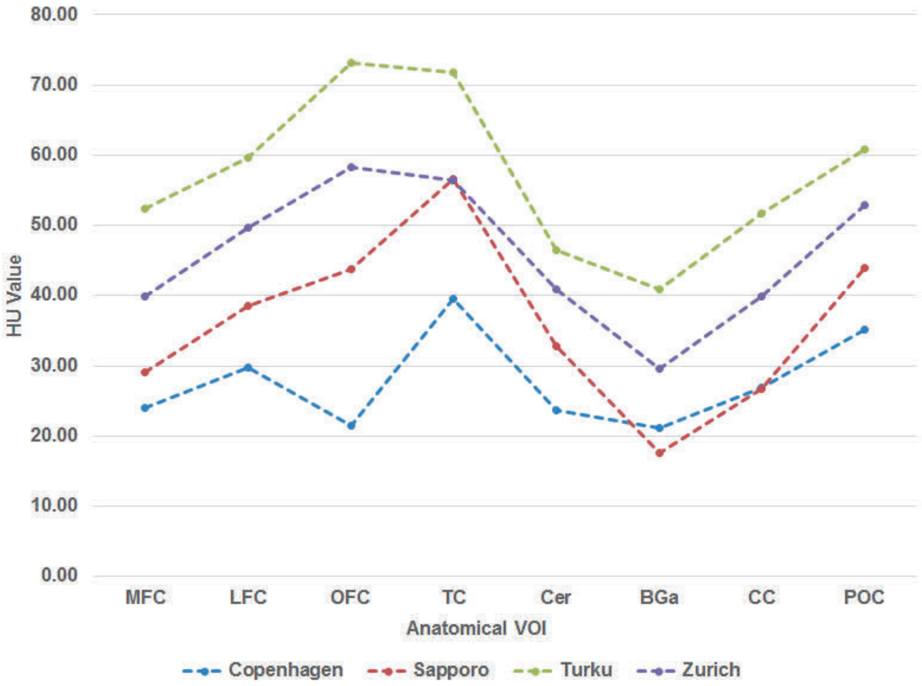

Figure 11. HUs measured from CTAC at each institution as a function of anatomical VOI, showing only minor variation especially between institutions where the same phantom was used. Modified from Study I. This research was originally published in JNM. Teuho et al., 2016. Effect of Attenuation Correction on Regional Quantification Between PET/MR and PET/CT: A Multicenter Study Using a 3-Dimensional Brain Phantom. JNM. 2016;57:818–824. © by the Society of Nuclear Medicine and Molecular Imaging, Inc.

The results of the quantitative evaluation of the PET images are shown in Figure 12, calculated from (eq. 20 and eq. 22) and Figure 13 calculated from (eq. 21) in Methods section 4.2.3. Intersystem differences between different institutions were below 4 % with PET/CT systems and below 5 % with PET/MR systems both region-wise and system-wise in the on- and off-site comparisons. No significant differences ($p>0.05$) between systems were detected when each of the PET/MR system was compared with a PET/CT within an institution.

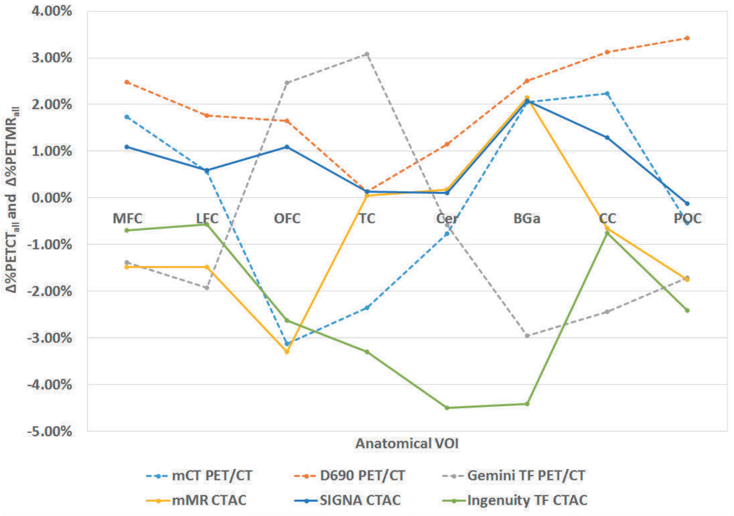

Figure 12. Regional comparison of PET/CT (eq. 20) and PET/MR systems (eq. 22) using CTAC, off-site comparison. Mediofrontal cortex, lateral frontal cortex, cingulate cortex, and parietooccipital cortex agree well between systems. MFC = medial frontal cortex; LFC = lateral frontal cortex; OFC = orbitofrontal cortex; TC = temporal cortex; Cer = cerebellum; BGa = basal ganglia; CC = cingulate cortex; POC = parietooccipital cortex. Modified from Study I. This research was originally published in JNM. Teuho et al., 2016. Effect of Attenuation Correction on Regional Quantification Between PET/MR and PET/CT: A Multicenter Study Using a 3-Dimensional Brain Phantom. JNM. 2016;57:818–824. © by the Society of Nuclear Medicine and Molecular Imaging, Inc.

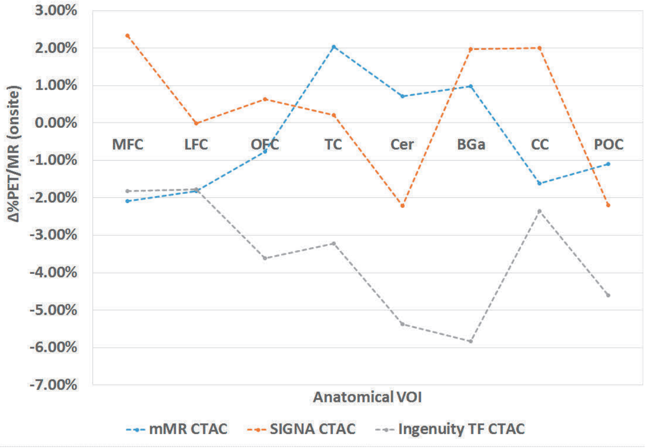

Figure 13. Regional comparison of PET/MR systems using CTAC against PET/CT systems, on-site comparison (eq. 21). Differences are plotted by region. All PET/MR systems agree well with the PET/CT systems within the institution. MFC = medial frontal cortex; LFC = lateral frontal cortex; OFC = orbitofrontal cortex; TC = temporal cortex; Cer = cerebellum; BGa = basal ganglia; CC = cingulate cortex; POC = parietooccipital cortex. Modified from Study I. This research was originally published in JNM. Teuho et al., 2016. Effect of Attenuation Correction on Regional Quantification Between PET/MR and PET/CT: A Multicenter Study Using a 3-Dimensional Brain Phantom. JNM. 2016;57:818–824. © by the Society of Nuclear Medicine and Molecular Imaging, Inc.

5.2 Study II

Figure 14 shows the post-processed tissue probability masks and the final attenuation map with two subjects in MRI FOV size and resolution and in PET FOV size and resolution.

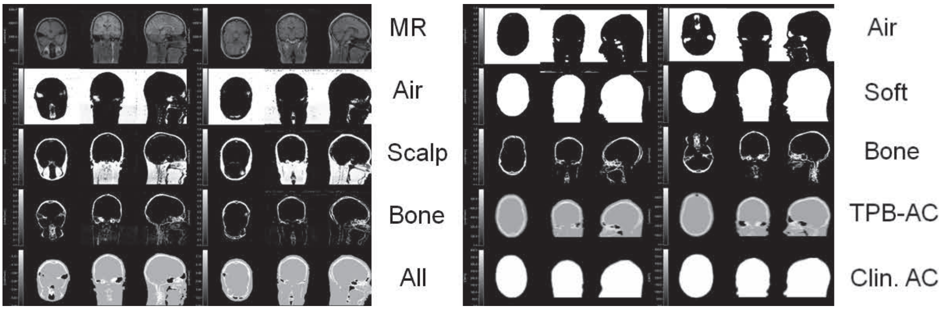

Figure 14. Patient MRI images, tissue probability masks before and after processing and the final TPB-AC attenuation map compared to the clinical MR-based attenuation map. Clin. AC denotes vendor-supplied MRAC. Modified from Study II. © 2016 IEEE

The relative difference (eq. 23, Methods section 4.4.2) of mean attenuation coefficients between TPB-AC and CTAC was in the range of -6 % to -1% across all patients when using 0.135 cm-1 for bone. This was reduced to -4.5 % to 0.4% when using 0.145 cm-1 for bone. In addition, the R^2–value varied from 0.82 to 0.89 when using 0.135 cm-1 for the bone and from 0.84 to 0.92 when using 0.145 cm-1 for bone. For the soft tissue VOI, the differences were minimal, in the range of -2.0 % to 1.4% and in the range of -1.4 % to 2% when using a higher attenuation coefficient for bone. For the skull VOI, there was much more variation patient-wise. When using 0.145 cm-1, the difference was -4.1 %, -8.2 % and -6.6 % for patients 2, 3 and 6, respectively. For the rest of the patients, the difference varied from -9.8 % to -11.6 %. When using 0.135 cm-1, the corresponding differences were much higher, -7.9 %, -12 % and -9.9 %, respectively. For the rest of the patients, the difference was in the range of -12.0 % to -15.1 %.

Table 4. VOI Analysis results of PET images (eq. 24, Methods section 4.4.2), comparison vendor-supplied MRAC and TPB-AC with two bone values (0.135 cm-1 and 0.145 cm-1) compared to CTAC corrected PET data. Mean relative difference and standard deviation of PET activity values across all VOI are given. Modified from Study II. © 2016 IEEE

Method	Vendor-supplied MRAC	TPB-AC (0.135 cm-1)	TPB-AC (0.145 cm-1)
Patient 1	-9 ± 4 %	-3 ± 1%	-2 ± 1 %
Patient 2	-8 ± 4 %	-2 ± 2 %	-1 ± 2 %
Patient 3	-9 ± 4 %	-5 ± 1 %	-4 ± 1 %
Patient 4	-3 ± 4 %	4 ± 3 %	-4 ± 3 %
Patient 5	-10 ± 4 %	-3 ± 1 %	-2 ± 2 %
Patient 6	-5 ± 4 %	-1 ± 2 %	-2 ± 2 %
Patient 7	-6 ± 3 %	0 ± 2%	-1 ± 2 %

Table 4 shows the results from the regional analysis of PET images in each subject. Across subjects, TPB-AC was closer to CTAC, while for the vendor-supplied MRAC the activity is underestimated compared to CTAC. The underestimation was decreased by 5 % on average and 7 % at maximum in TPB-AC reconstructed PET images compared to vendor-supplied MRAC reconstructed images. However, in one patient TPB-AC resulted in an overestimation of 4%. Increasing the bone value resulted in a 1% increase of mean activity in all patients except patient 4. In addition to having a smaller mean difference compared to CTAC across the regions, TPB-AC had a smaller standard deviation than in regional activity values across all subjects, with no changes between different attenuation coefficients for bone.

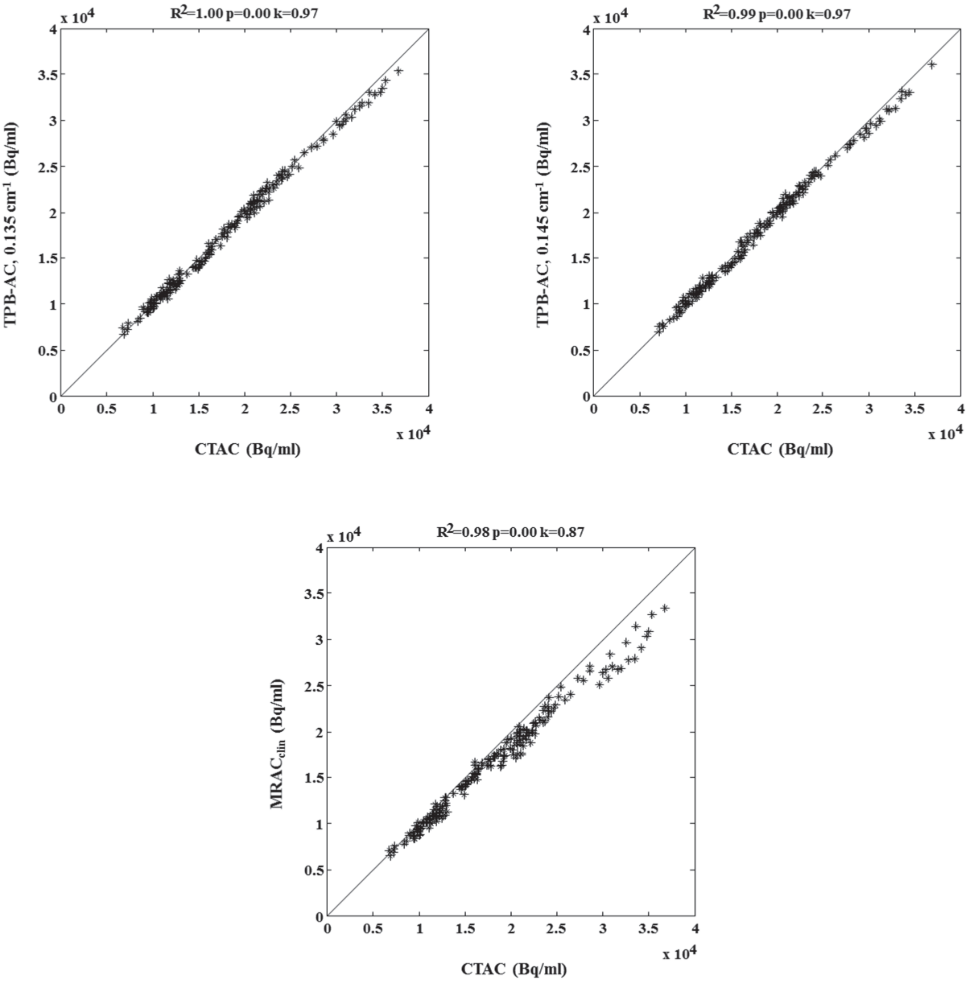

Figure 15. Scatter plot of regional radioactivity values measured from PET images reconstructed with CTAC, TPB-AC and vendor-supplied MRAC (MRAC$_{\text{clin}}$). The points correspond to 28 VOI values measured in 7 patients. Note that vendor-supplied MRAC tends to produce overall lower activity values across the scale compared to TPB-AC due to lack of bone. Modified from Study II. © 2016 IEEE

Finally, the correlation analysis supports the conclusion that TPB-AC with either of the bone attenuation coefficients yields a closer match to CTAC in comparison to vendor-supplied MRAC.

5.3 Study III

Figure 16 shows the comparison of bone delineation versus CTAC when using discrete and continuous bone in MRAC with 3 tissue classes while Figure 17 shows the difference between a 4-class and 6-class attenuation map using a segmentation-based skull. It can be seen from both Figure 16 and Figure 17 that with the modifications implemented in Study (III) compared to Study (II), two advantages are achieved: 1) the bone attenuation values are now continuous when derived based on the CT template 2) different brain tissues are now distinguishable especially in the 6-class MRAC. It should be noted that a slightly poorer bone lineation is achieved with continuous bone compared to discrete bone.

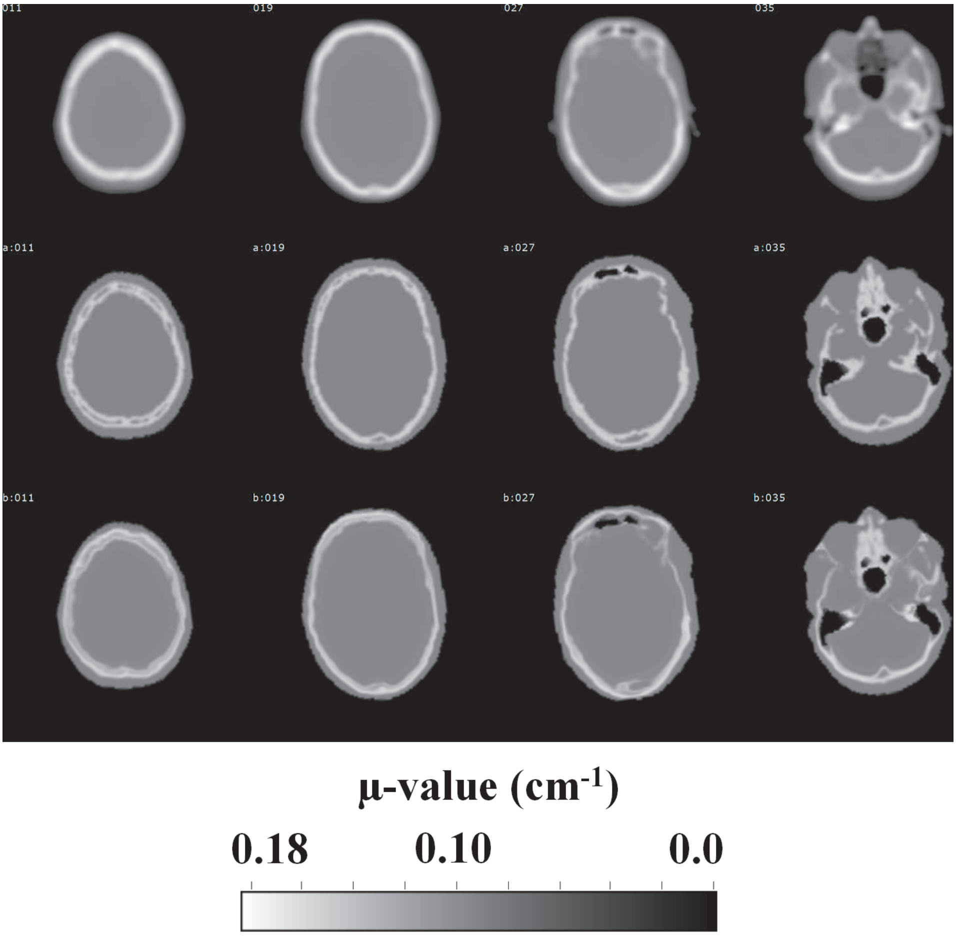

Figure 16. Comparison of μ-maps with CTAC in upper row, 3-class MRAC with discrete skull in middle row and 3-class MRAC with continuous skull and discrete sinuses in bottom row. Modified from Study III. © 2017 IEEE

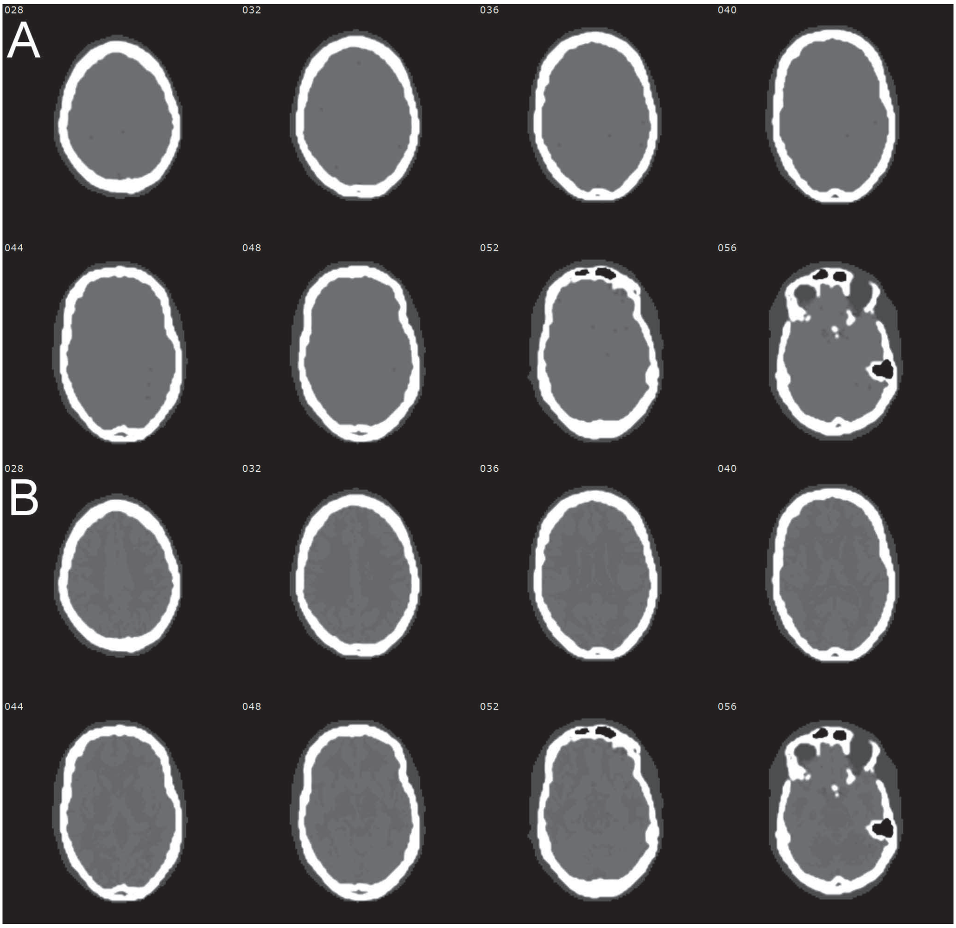

Figure 17. Visualization of different tissue classes in (A) 4-class and (B) 6-class μ-maps with discrete segmentation-based skull. Modified from Study III. © 2017 IEEE

All μ-maps achieved a good delineation of soft tissue with dice coefficients (eq. 25, Methods section 4.5.4) of 0.86 (±0.01) and 0.89 (±0.01) for template-based and segmentation-based methods, respectively. Similarly, the dice coefficients for brain tissue were 0.82 (±0.03) and 0.84 (±0.03). All methods delineated air well, with dice coefficients of 0.94 (±0.02) and 0.95 (±0.02). The methods with segmentation-based discrete skull had the highest mean dice coefficient of 0.76 (±0.05) when compared to CTAC. In comparison, template-based continuous skull had a dice coefficient of 0.67 (±0.06), which was increased to 0.69 (±0.05) when template-based sinuses were included.

Figure 18 shows the results from the VOI analysis of the PET images with the absolute mean relative difference (eq. 27, Methods section 4.5.4) with standard deviation of the absolute relative difference across all patients, for 3-, 4-, and 6-class MRAC.

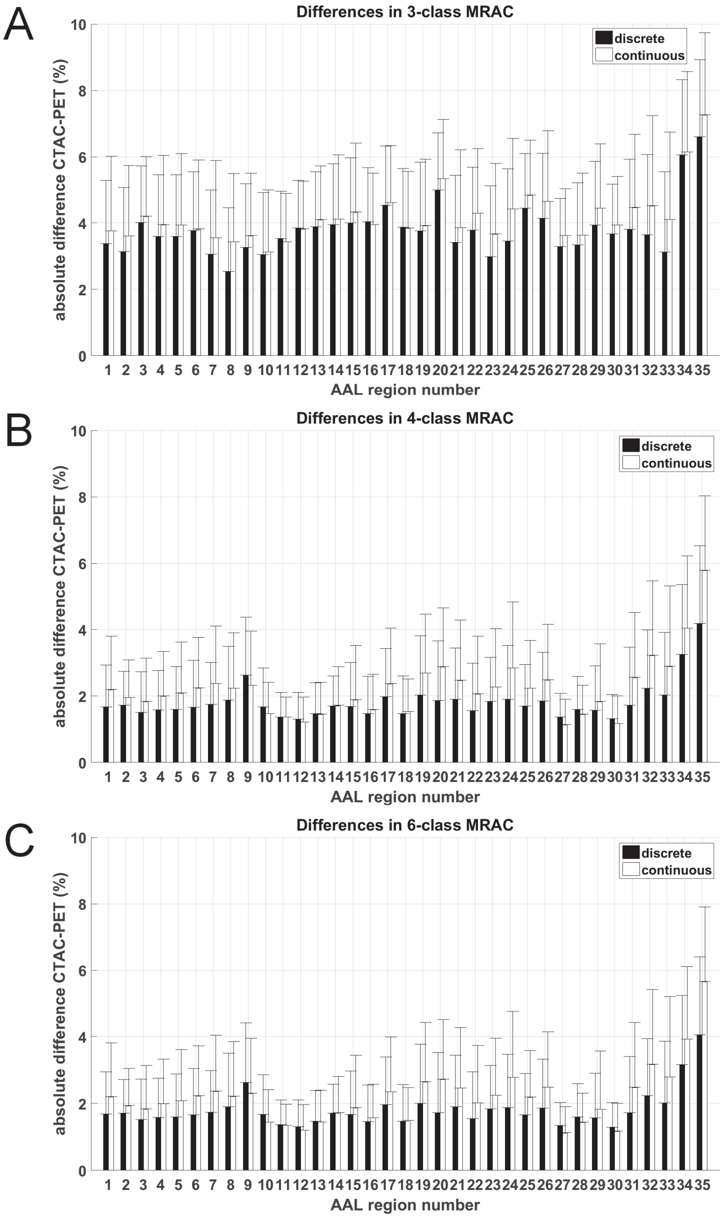

Figure 18. Results from the VOI analysis of PET images with (A) 3-class MRAC, (B) 4-class MRAC, (C) 6-class MRAC. Absolute mean relative difference with standard deviation of the absolute relative difference to CTAC reconstructed PET is shown (eq. 27, Methods section 4.5.4). Modified from Study III. © 2017 IEEE

Figure 19 shows the mean relative difference (eq. 26, Methods section 4.5.4) with 3-class MRAC when using discrete or continuous skull with either discrete or continuous sinuses with the mean relative difference (eq. 26) between 4-class and 6-class MRAC with discrete skull.

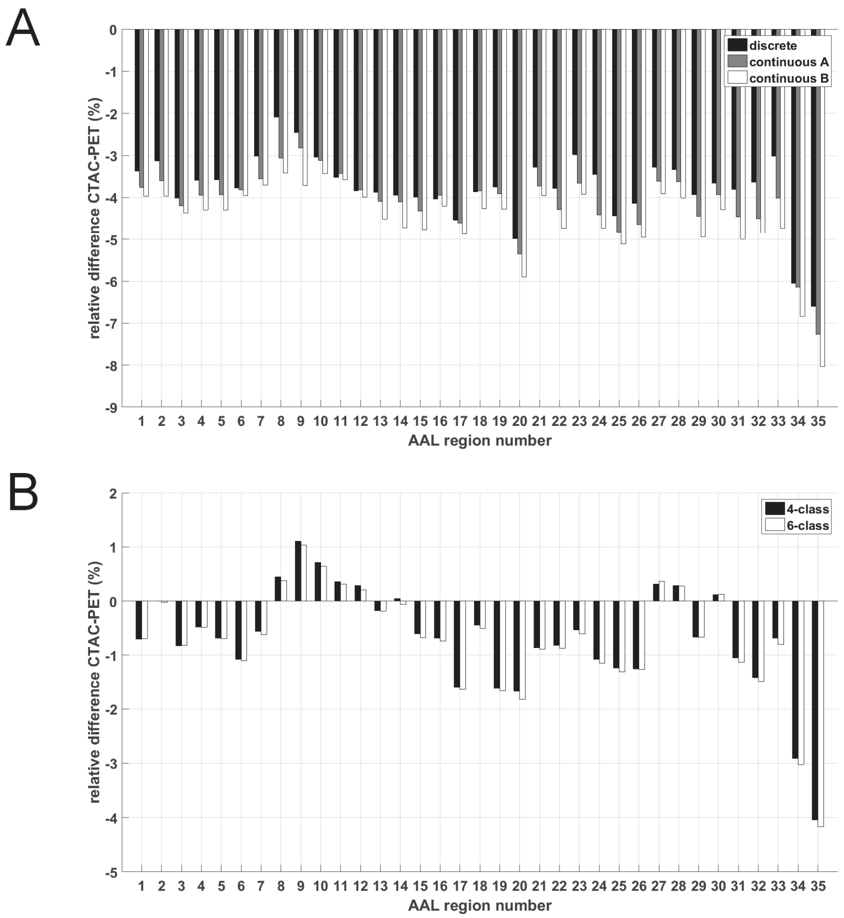

Figure 19. Results from the VOI analysis of PET images, (A) Differences in discrete segmentation-based skull to continuous template-based skull with discrete (continuous A) and continuous (continuous B) sinuses compared to CTAC (B) Differences in 4-class and 6-class MRAC compared to CTAC. Mean relative difference (eq. 26, Methods section 4.5.4) to CTAC reconstructed PET is shown. Modified from Study III. © 2017 IEEE

It is evident that three-class MRAC has higher mean and maximum absolute difference in all regions of the brain than the methods which add either one or three additional tissue classes for the brain. No large difference exists between continuous and discrete bone or between different methods of including the sinuses. Likewise, 4-class and 6-class MRAC perform in nearly the same way.

The mean relative difference and standard deviation compared to CTAC were: 3-class MRAC with discrete skull −3.77% (±1.95%), 3-class MRAC with continuous skull and discrete sinuses −4.14% (±2.07%) and template-based sinuses −4.52% (±1.79%), 4-class MRAC with discrete skull −0.74% (±2.07%), with continuous skull −1.70% (±1.96%), 6-class MRAC with discrete skull −0.69% (±2.07%), and with continuous skull −1.65% (±1.96%) across all regions and patients.

The largest bias with each method was detected in the cerebellum. The mean relative difference and standard deviation were: 3-class MRAC with discrete skull −6.60% (±2.31%), 3-class MRAC with continuous skull with discrete sinuses −7.26% (±2.48%) and continuous sinuses −8.03% (±2.26%), 4-class MRAC with discrete skull −4.17% (±2.36%), 4-class MRAC with continuous skull −5.78% (±2.24%), 6-class MRAC with discrete skull −4.04% (±2.36%), and 6-class with continuous skull −5.66% (±2.24%) across all patients.

Figure 20 shows the mean and standard deviation atlas images for all MRAC methods. The mean bias range was less than 5% on an absolute scale with 3-class MRAC and less than 3% with 4-class and 6-class MRAC inside the brain. However, addition of brain tissues results in slight overestimation in the range of 1% to 3% in mid-regions of the brain. This would imply that the brain tissue attenuation coefficients may be overestimated somewhat in some of the patients. Lower bias can be seen with the segmentation-based skull near the bone, although the difference is small. Lower standard deviation is seen with 4- and 6-class methods.

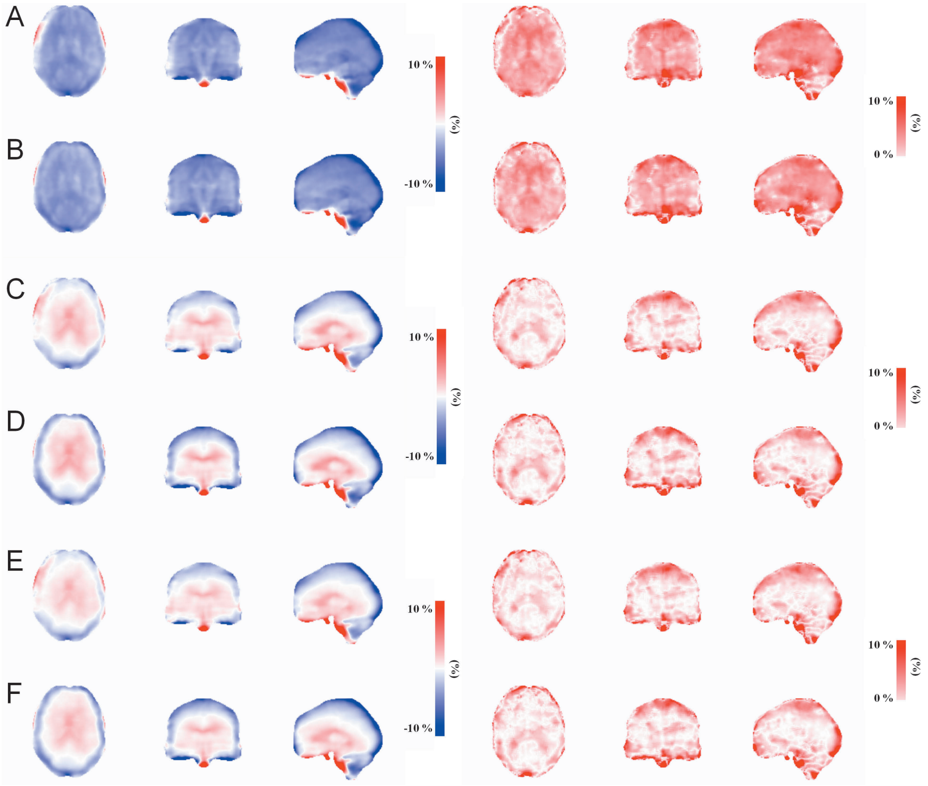

Figure 20. Atlas bias images (Ouyang et al., 2013), calculated across all the subjects for 3-class MRAC [(A) discrete, (B) continuous], 4-class MRAC [(C) discrete, (D) continuous], and 6-class MRAC [(E) discrete, (F) continuous] displaying the mean bias and the standard deviations (left and right row within each group). Modified from Study III. © 2017 IEEE

Finally, the computational time needed to create different MR-based attenuation maps was in the range of 5–14 s with discrete skull and 15–24 s with continuous skull. The creation of tissue probability maps was the most time-consuming process, taking approximately 129–210 s to complete. Therefore, the operational effort of the method was not significantly increased compared to the method in Study (II).

5.4 Study IV

The sinogram profiles (Methods section 4.6.4) for the scatter sinogram, emission sinogram and the transmission sinogram mask from the clinical subjects with three different attenuation maps used in scatter calculation are presented in (Figure 21). The measured sinogram profiles with three different attenuation maps for the phantom study are presented in (Figure 22). A minor difference in the scatter sinogram amplitude can be seen when using MC-SSS, where CTAC has the highest and $\mathrm{MRAC}_{2\mathrm{class}}$ has the lowest scatter profile. There is virtually no difference in the scatter sinogram profiles with TF-SSS when using different attenuation maps.

The calculated scatter fractions $\mathrm{SF}_{\mathrm{tot}}$ (eq. 28, Methods section 4.6.4) in the phantom study for TF-SSS were 19.25% with CTAC, 19.24% with $\mathrm{MRAC}_{3\mathrm{class}}$ and 19.23% with $\mathrm{MRAC}_{2\mathrm{class}}$. Similarly, the scatter fractions for MC-SSS were 19.95% with CTAC, 18.35% with $\mathrm{MRAC}_{3\mathrm{class}}$ and 17.84% with $\mathrm{MRAC2}_{\mathrm{class}}$. Thus, only minor differences were detected in the scatter fractions with the TF-SSS algorithm, while the MC-SSS algorithm shows a dependency on the attenuation map similarly to the phantom study.

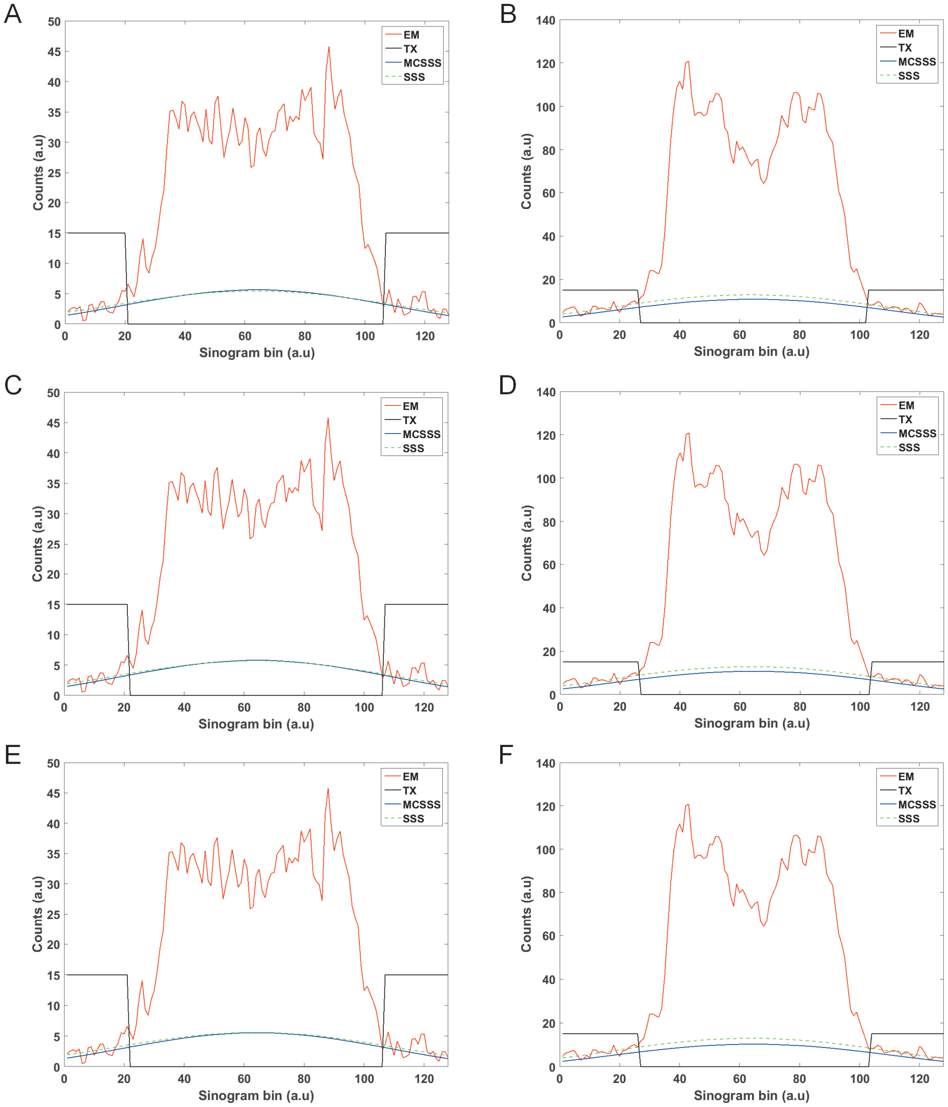

Figure 21. Measured sinogram profiles from randoms-corrected emission sinogram (EM), transmission sinogram mask (TX), and scatter sinograms from TF-SSS (SSS) and MC-SSS (MCSSS) for 2 subjects (subjects 4 and 1). Best (left) and worst case showing poorer fit for MC-SSS (right) are presented. Shown are the sinogram profiles when using CTAC (A and B), MRAC$_{3class}$ (C and D), and MRAC$_{2class}$ (E and F) in scatter calculation. This research was originally published in JNM. Teuho et al., 2017. Quantitative Evaluation of 2 Scatter-Correction Techniques for 18F-FDG Brain PET/MRI in Regard to MR-Based Attenuation Correction. JNM. 2017;58:1691-1698. © by the Society of Nuclear Medicine and Molecular Imaging, Inc.

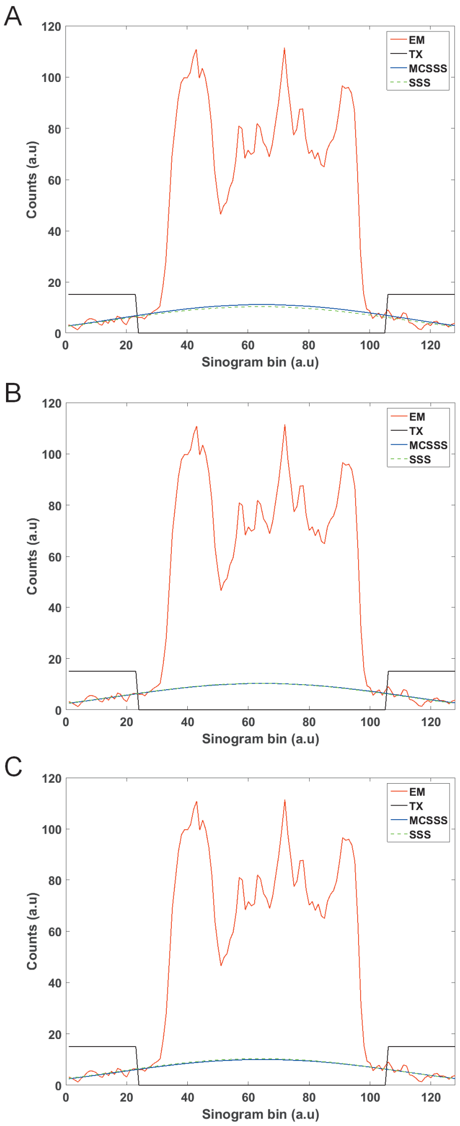

Figure 22. Measured sinogram profiles from randoms-corrected emission sinogram (EM), transmission sinogram mask (TX), and scatter correction sinograms from TF-SSS (SSS) and MC-SSS (MCSSS) for the phantom. Shown are the sinogram profiles when using CTAC (A), MRAC$_{3class}$ (B), and MRAC$_{2class}$ (C) in scatter calculation. This research was originally published in JNM. Teuho et al., 2017. Quantitative Evaluation of 2 Scatter-Correction Techniques for 18F-FDG Brain PET/MRI in Regard to MR-Based Attenuation Correction. JNM. 2017;58:1691-1698. © by the Society of Nuclear Medicine and Molecular Imaging, Inc.

Table 5 shows the results from the absolute activity measurement (eq. 29, Methods section 4.6.5) of the phantom with a whole brain VOI. The %RC was calculated using a value of 45.87 kBq/ml for true activity.

Table 5. Activity recovery (eq. 29, Methods section 4.6.5) in the whole brain VOI in the phantom study with each of the attenuation maps. This research was originally published in JNM. Teuho et al., 2017. Quantitative Evaluation of 2 Scatter-Correction Techniques for 18F-FDG Brain PET/MRI in Regard to MR-Based Attenuation Correction. JNM. 2017;58:1691-1698. © by the Society of Nuclear Medicine and Molecular Imaging, Inc.

	Scatter Algorithm	Mean (kBq/ml)	Standard Deviation (kBq/ml)	Maximum (kBq/ml)	Recovery Coefficient (%)
CTAC	**TF-SSS**	20.24	11.47	56.06	38.58
	MC-SSS	20.17	11.48	56.08	38.43
	Difference (%)	-0.35	0.09	0.04	
MRAC$_{3class}$	**TF-SSS**	18.07	10.43	51.16	34.43
	MC-SSS	18.00	10.42	51.07	34.30
	Difference (%)	-0.39	-0.10	-0.18	
MRAC$_{2class}$	**TF-SSS**	17.33	10.01	48.13	33.03
	MC-SSS	17.44	10.02	48.26	33.23
	Difference (%)	0.63	0.10	0.27	

The results show only minor differences between the two scatter scaling algorithms, independent of the underlying attenuation maps. The VOI analysis results of the clinical subjects are presented in (Figure 23). The mean relative difference between TF-SSS and MC-SSS reconstructed PET is smaller than 2.1 % while the maximum difference is 4.2 %. The differences between the two algorithms in both the phantom and the clinical study were of similar range.

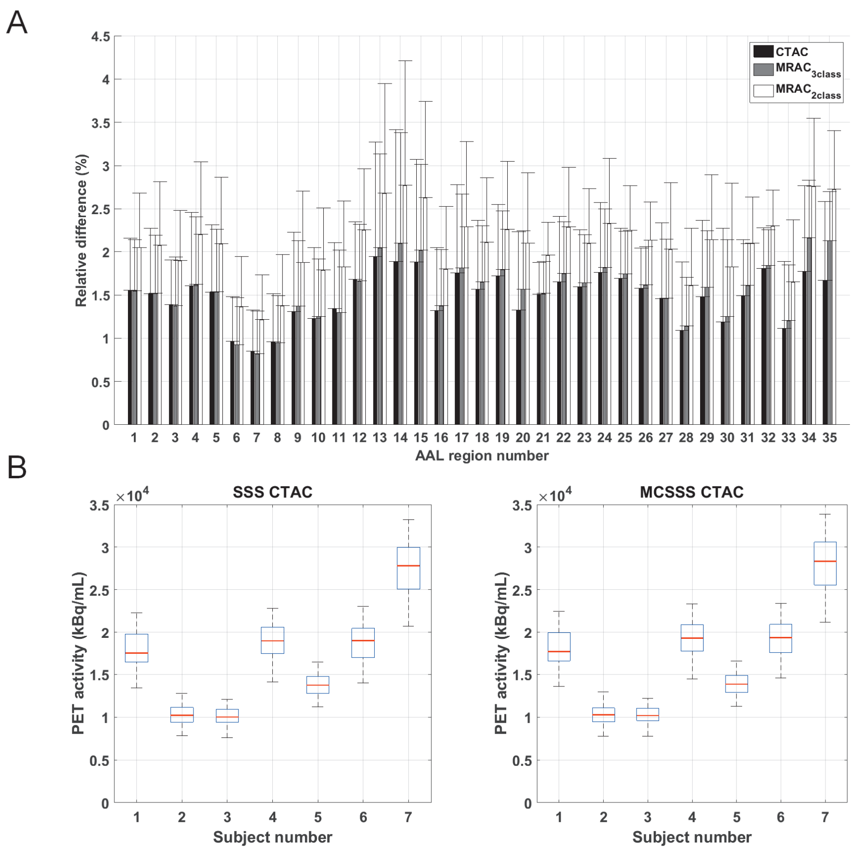

Figure 23. VOI analysis results of subjects between TF-SSS and MC-SSS using different µ-maps. The mean and standard deviation of the relative difference (eq. 30, Methods section 4.6.6) are shown in Figure 23 (A).Regional differences between TF-SSS and MC-SSS remain the same regardless of the µ-map used (A) and remain small subjectwise as well (B). MCSSS results in higher reconstructed activity in A and B by 2%. The largest differences exist with $\mathrm{MRAC2_{class}}$. This research was originally published in JNM. Teuho et al., 2017. Quantitative Evaluation of 2 Scatter-Correction Techniques for 18F-FDG Brain PET/MRI in Regard to MR-Based Attenuation Correction. JNM. 2017;58:1691-1698. © by the Society of Nuclear Medicine and Molecular Imaging, Inc.

The comparison of mean ratio and PET images across the subjects showed only minor differences between the algorithms. Figure 24 shows mean PET ratio images of TF-SSS versus MC-SSS reconstructed PET over all subjects with each attenuation correction method. In the ratio images, a slight dependency in the MC-SSS is again found similarly to the scatter fraction and VOI measurements although the magnitude of the positive bias in MC-SSS reconstructed PET can be considered to be small (< 5 %).

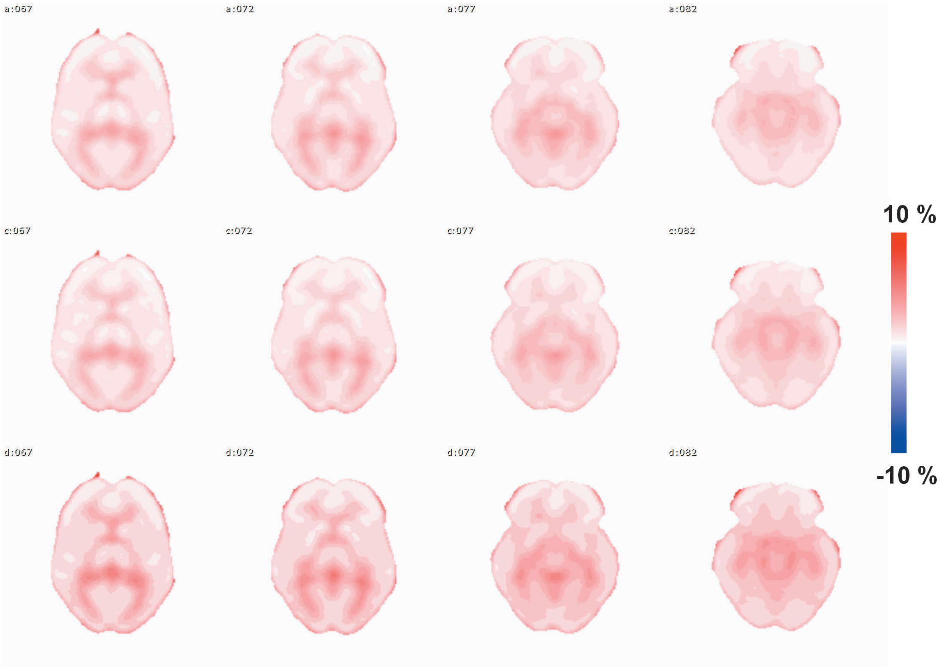

Figure 24. Mean ratio images calculated over all subjects, pixel-by-pixel comparison of TF-SSS versus MC-SSS. First row shows CTAC-reconstructed PET and second and third rows show $\text{MRAC}_{3\text{class}}$- and $\text{MRAC}_{2\text{class}}$-reconstructed PET, respectively. A small positive bias (< 5 %) in MC-SSS reconstructed PET can be detected. This research was originally published in JNM. Teuho et al., 2017. Quantitative Evaluation of 2 Scatter-Correction Techniques for 18F-FDG Brain PET/MRI in Regard to MR-Based Attenuation Correction. JNM. 2017;58:1691-1698. © by the Society of Nuclear Medicine and Molecular Imaging, Inc.

Finally, Figure 25 shows mean PET images over all subjects, showing a visual comparison of TF-SSS and MC-SSS reconstructed PET with different attenuation maps. No visual differences could be detected between the scatter algorithms.

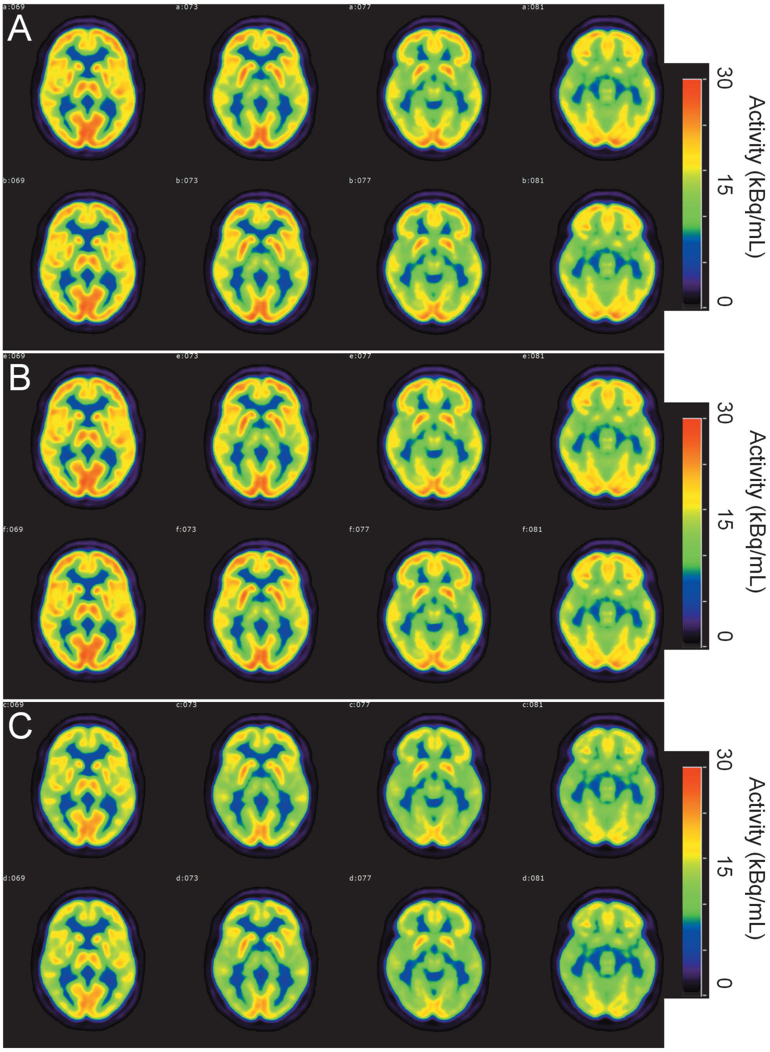

Figure 25. Mean PET images calculated over all subjects. No difference can be detected visually between TF-SSS and MC-SSS reconstructed PET images. (A) CTAC-reconstructed PET. (B and C) $MRAC_{3class}$ and $MRAC_{2class}$-reconstructed PET, respectively. This research was originally published in JNM. Teuho et al., 2017. Quantitative Evaluation of 2 Scatter-Correction Techniques for 18F-FDG Brain PET/MRI in Regard to MR-Based Attenuation Correction. JNM. 2017;58:1691-1698. © by the Society of Nuclear Medicine and Molecular Imaging, Inc.

6 DISCUSSION

The main findings and conclusion of the individual studies (I to IV) are briefly discussed and summarized in sections 6.1 to 6.4, while the limitations and future directions are summarized in section 6.5.

6.1 STUDY I:

6.1.1 Establishing a baseline of the quantitative accuracy of PET/MR systems for ^{18}F-FDG imaging

The first step in evaluating and improving the quantitative accuracy of ^{18}F-FDG neurological PET/MR imaging was to evaluate whether MRAC is the largest factor affecting the quantitative bias between PET/MR and PET/CT systems. It is evident that when a standard and fairly accurate attenuation correction method is implemented for the PET/MR systems, the inter-center variations are reduced to a level found with the PET/CT systems. In this case, CTAC serves as the “silver” standard for attenuation correction. It should be noted that the HU values were quite repeatable between PET/CT systems. Although each site used its own conversion method from HU to linear attenuation coefficients, the PET values were quite reproducible between individual systems.

Our results complement the studies of Andersen et al., (Andersen et al., 2014) and our earlier study (Teuho et al., 2014) where a critical need to implement an MRAC method which would include bone attenuation was shown. Thus, bringing the quantitative accuracy of the PET/MR systems up to the level of PET/CT systems in ^{18}F-FDG imaging is to provide a more accurate attenuation estimate, which takes into account soft tissue, air and bone at a minimum. Our results are complemented by the later study of Lagefoed et al., (Lagefoed et al., 2017) which showed that several promising MRAC methods are available to address this MRAC problem. Therefore, we state on the basis of the results of both our phantom study the study of Lagefoed et al., (Lagefoed et al., 2017) that several methods which allow accuracy close to CTAC are now available. Thus, by adoption of these methods there should be no longer be any reason why performance in neurological PET/MR imaging would not be at the level of PET/CT.

Furthermore, our study serves in part to establish a common baseline and a target criterion for quantitative accuracy to be achieved when new MRAC methods are to be developed. Based on the results in both PET/CT and PET/MR systems, the criterion for the MRAC method would be ideally to achieve an accuracy close to the maximal variations measured in this study with the system of poorest performance: 6 % in the regional analysis and less than 5 % in system-wise analysis. The total range covering all variation regionally and between systems would be 10 %. This would serve as the criterion to be achieved with any MRAC method developed to minimize the bias due to attenuation correction. It should be noted that an error < 10 % is considered feasible for SUV quantification and an error < 5 % is considered feasible for repeatability in PET imaging (Schultz et al., 2011; Ladefoged et al., 2017).

6.1.2 Residual variation in PET images

A residual variation of VOI values exists in the PET/MR systems, but it is very important to note that variation in the VOI is also found in the PET/CT systems as well. Regionally, the orbitofrontal cortex, temporal cortex, and cerebellum had the largest variations, and these were statistically significant. Therefore, while the use of CTAC or a similar method allows minimizing the bias due to MRAC, the performance differences between individual systems cannot be entirely negated. This is expected as there are several factors (e.g. resolution uniformity across PET FOV) other than attenuation correction which affect the remaining bias both in the magnitude and spatial location of PET images even after post-processing of the PET images (Joshi et al., 2009).

The remaining differences between the systems are probably due to resolution differences within the axial FOV, differences in calibration and implemented reconstruction algorithms and their convergence rate or data correction procedures such as attenuation and scatter correction. Corrections for both dead time and, randoms, normalization, and calibration were not evaluated, each of which has an effect on image quantification. Technical factors such as phantom orientation, filling, VOI definition, remaining resolution differences after filtering, image registration, and interpolation will introduce variability, in addition to PET/MR-specific factors such as MR coils. Ultimately, these factors should be studied closely in the future to further evaluate and eventually harmonize the performance between systems.

6.1.3 Attenuation correction on non-standard and standard phantoms.

The vendor-supplied segmentation algorithm is not designed for use in non-standard phantoms. This is evident from Figure 10. This is mostly due to phantom materials which have quite different relaxation properties from biological tissues.

Most phantoms consist of fixed polymer or plastic structures, which are challenging to visualize using conventional T1/T2 or Dixon sequences commonly implemented for MRAC. While phantom liquids are quite easily visualized using these conventional sequences, any fixed materials such as the plastic shell of the phantom are still ignored. Thus, any phantom without either a predefined CT/TX template or a specific acquisition and segmentation protocol on the PET/MR system will not be segmented and delineated properly in the MR-based attenuation map.

Polyvinyl alcohol (PVA) cryogel phantoms might allow differentiation of phantom structures in PET/MR imaging (Soultanidis et al., 2013), although they have not yet been adopted into routine use. An alternative option is to fill the phantom with a liquid which would allow better delineation of the liquid compartments of the phantom (Ziegler et al., 2013), although this option does not allow to delineate the borders of the cylinder. Thus, either a dedicated phantom MRAC sequence or a transmission- or CT-based template which would be registered to the phantom anatomy is needed, as suggested by Boellaard et al., (Boellaard et al., 2015). These conclusions also apply to standard phantoms used for quality control and validation.

However, one limitation of applying a template-based MRAC protocol for phantom imaging for standard or non-standard phantoms is that they require near-perfect filling and positioning of the phantom. Care must also be taken as to how the attenuation coefficients for phantoms are selected if a predefined template or an acquisition protocol is used. If templates are not available on the system, an additional CT or TX scan should be used to ensure accurate quantification. Until a dedicated “phantom MRAC sequence” is found, the applicability of non-standard phantoms is limited by the availability of on-site CTAC or TXAC. Interestingly, there are no reports on applying short echo time sequences such as UTE and ZTE to derive phantom attenuation maps.

6.1.4 Main conclusion

Our study shows that it is possible to minimize the differences between PET/CT and PET/MR systems to a large degree by using CTAC (or a MRAC approach with a similar performance to that of CTAC) even with quite a simple post-processing chain. Thus, the main requirement to minimize the differences between the PET/CT and PET/MR systems is to produce an accurate attenuation map. Finally, we state that to the best of our knowledge, this was the first such investigation, and it was conducted in a multicenter setting covering 4 institutions and 7 systems covering all PET/CT and PET/MR systems of all major vendors in the clinical market.

6.2 STUDY II:

6.2.1 *Development and validation of a new MRAC method*

The second step in improving the quantitative accuracy in ^{18}F-FDG neurological PET/MR imaging to the level of PET/CT was to implement and validate a new MRAC method, improving the quantitative accuracy compared to the vendor-implemented MRAC ignoring bone.

The new MRAC method allows improving the PET image quantification compared to the vendor-provided MRAC method on the Ingenuity TF PET/MR system, enabling the quantitative accuracy in PET needed for accurate SUV quantification (< 10 %). No additional MR sequences are required and the method can be applied retrospectively to patient data already collected. The only prerequisite is access to T1-weighted data.

Therefore, our study shows that it is possible to completely derive an MR-based, individual attenuation map representing soft tissue, air and bone by using the standard attenuation MR acquisition of the Philips Ingenuity TF PET/MR together with tissue probability maps produced by the New Segment function of SPM8. This attenuation map can be created solely from a single MR sequence acquired as part of a routine examination.

6.2.2 *Main conclusion*

The MRAC method developed in this study allows accounting for the patient skull from T1-weighted images, offering a simple and computationally efficient method for improved attenuation correction. The method provided an improvement when compared to the MRAC currently available on the system and offers good accuracy when compared to CTAC and similar methods in the field. This was the first time the segmentation and processing of tissue probability maps using T1-weighted data alone was used to create an MR-based attenuation map.

6.3 STUDY III:

6.3.1 *Improving the quantitative accuracy of the MRAC method with additional tissue classes and continuous bone*

The third step was to perform a rigorous analysis of the quantitative accuracy of the MRAC method suggested by Study II and to improve it further for more demanding applications such as kinetic modeling for ^{18}F-FDG neurological PET/MR. The purpose was to improve the quantitative accuracy to the level measured in Study (I) (< 5 % error in most gray matter regions) and proposed in the literature (Ladefoged et al., 2017; Mehranian et al., 2016) by accounting for additional tissue classes for the brain and by adding a continuous estimate of the skull bones.

Several reports evaluating MRAC methods have reported the largest biases typically in the cerebellum region. Sekine et al., reported a relative difference of 3.69% ± 1.43% in the cerebellum with an atlas-based method (Sekine et al., 2016a), and 3.31% ± 1.70% when using a ZTE-based method (Sekine et al., 2017). Dickson et al., reported a difference of 17.3 % when using a UTE-based method (Dickson et al., 2014). Schramm et al., reported a mean relative difference of +12% (±6) when using the vendor-supplied MRAC method in the Ingenuity TF PET/MR (Schramm et al., 2013). In comparison, the method presented in Study III resulted in −6.60% (±2.31) for 3-class MRAC, −4.17% (±2.36%) for 4-class MRAC and −4.04% (±2.36%) for 6-class MRAC, when using a discrete skull. The bias was higher when using continuous skull. Therefore, a method, which could estimate the denser bone in the cerebellum region could reduce the bias as reported by (Ladefoged et al., 2015) would be the next development step.

Our results show that a large benefit in quantitative accuracy in PET can be gained by addition of at least one tissue class to account for the higher attenuation of the brain tissue. No large difference can be seen when using either discrete or continuous bone values for the skull. Combining both the GM and WM tissue classes would allow the creation of a 5-class attenuation map with quantitative accuracy between the 4-class and 6-class methods. Therefore, the addition of at least one additional tissue class or optimally two (one for GM/WM and one for CSF) would be sufficient to account for the attenuation of the tissues consisting of GM, WM and CSF. It also seems that when a specific maximum of separate tissue classes is reached, adding more classes does not result in large gains in quantitative accuracy and will only increase the complexity of the MRAC method.

Our findings are consistent with (Akbarzadeh et al., 2011; Akbarzadeh et al., 2013; Ouyang et al., 2013; Keereman et al., 2011), who have shown that introducing more tissue classes in segmentation-based MRAC is beneficial for improving quantitative accuracy in PET. In addition to brain tissues, accounting for fat from a Dixon-based sequence might be beneficial as was shown by Berker et al., (Berker et al., 2012). However, the current T1-weighted sequence does not allow a reliable segmentation of fat. In comparison, Lagefoed et al., (Ladefoged et al., 2015) used additional tissue masks to account for the regions which are challenging to segment: the sinus region, mastoid cells and the skull base.

If needed, the attenuation of the sinuses can be accounted for with a CT template or a sinus-specific attenuation coefficient in the method presented in this study. Interestingly, a very recent study studied the effect of sinus region attenuation. Yang et al., (Yang et al., 2017) proposed that accounting for sinus attenuation is beneficial for cerebellum quantification, which is similar to our initial experience as well (Teuho et al., 2017). We have performed initial investigation of a dedicated mask and attenuation coefficient within the sinus region in a small patient group: accounting for the attenuation of the sinus region with a specifically selected attenuation coefficient could be beneficial. This has a large effect mainly on minimizing the local bias in the sinus region while the effects across the whole gray matter are very small. The bias in the region of the cerebellum and putamen and the addition of an additional mask for the mastoid cell region as suggested by (Yang et al., 2017) should be investigated in more detail in future studies.

Our method offers two approaches to derive the patient skull: segmentation-based and CT-template based. However, a poorer anatomical delineation of the skull when using the CT-template method is achieved. Although this was improved with the latest release of our MRAC method (http://bit.ly/2fx6Jjz), which implemented improved segmentation for both the segmentation-based and CT-template based skull, the CT-template based skull still performs more poorly than the discrete segmentation-based skull. This is most probably caused by using a single template approach and a simple one-step registration in SPM8 for wrapping of the template to individual anatomy. An advanced registration method such as DARTEL in SPM8 (Izquierdo-Garcia et al., 2014) and SPM12 would need to be implemented in the future. The method of (Izquierdo-Garcia et al., 2014) uses DARTEL registration to wrap the CT template to patient anatomy. This seems to produce very good results even when subject anatomy is deformed.

The author is in the process of implementing such a method, although this will result in an increase in method complexity and computational cost. Further studies are needed to specify how much benefit these improvements will bring in total compared to the increased complexity of the method.

6.3.2 Main conclusion

This study was the first of its kind to evaluate the effect of brain tissue attenuation using 3-class, 4-class and 6-class MRAC with a discrete segmentation-based skull in comparison to continuous CT template-based skull in clinical brain MRAC. It is clearly seen that accounting for the brain tissues either with one dedicated tissue class or two additional tissue classes is beneficial for improving the quantitative accuracy of MRAC. No major benefit was seen when using a CT template-based method to account for the continuity of bone.

6.4 STUDY IV:

The fourth and final step in evaluating and improving the quantitative accuracy of ^{18}F-FDG neurological PET/MR was to investigate the remaining bias in PET images due to the effect of MRAC on scatter correction accuracy. Investigation of scatter sinogram profiles, scatter fractions and regional quantification was performed.

Differences between TF-SSS and MC-SSS were minimal in the comparison of scatter sinogram profiles and scatter fractions in the phantom and patient study, regardless of the attenuation map used in PET reconstruction. Similarly to the sinogram data analysis, the quantitative and visual differences were small in both the phantom and patient PET data. Naturally, it should be noted that in reconstructed PET images the effects of attenuation and scatter are mixed.

A slight dependency due to MRAC was detected in the MC-SSS algorithm, which had a small effect (< 5 %) even with the MRAC excluding bone. The TF-SSS algorithm offered consistent quantitative performance regardless of the accuracy of the MRAC. The performance of the MC-SSS algorithm was comparable but not superior to TF-SSS, warranting further investigations of algorithm optimization and performance with different radiotracers and TOF imaging.

In comparison to previous reports, (Bourgos et al., 2014) concluded that the difference between an ideal scatter estimate with CTAC and a non-ideal one with MRAC was less than 1 % with the SSS algorithm using tail fitting. Although very little details were given about the analysis, (Son et al., 2010) concluded that the effect of changing the attenuation map on the performance of the scatter correction algorithm was not significant. Our results are consistent with the few reports that exist about the influence of different attenuation maps on the performance of scatter correction.

Thus, whether MC-based scaling or TF-based scaling is used, the SSS algorithm still remains a reliable method for scatter correction in non-TOF ^{18}F-FDG brain PET/MR imaging regardless of the accuracy of the MR-based attenuation map.

6.4.1 Differences between MC-SSS and TF-SSS explained by different scatter scaling methods

As can be seen from both the phantom and patient study, MC-SSS shows a dependency on the accuracy of the MR-based attenuation map, although this is slight. TF-SSS does not show this kind of variation. The difference is explained by the difference between the scaling methods.

The TF-SSS scales the derived scatter shape to the emission tails, where the amplitude of the tails is not affected by the attenuation map, as they are located outside the transmission boundaries. Therefore, the scaling parameter needed to scale the SSS estimate in TF-SSS does not vary significantly between different attenuation maps, although the amplitude of the scatter estimate derived by SSS before scaling is slightly lower when using MRAC without bone. Small local errors in the scatter sinogram spatial shape and magnitude are thus neglected to some degree when the estimate is fitted to the sinogram tails.

On the other hand, the MC-SSS derived scatter estimate is lower mainly for two reasons: 1) the SSS derived scatter estimate has lower amplitude as the attenuation coefficients in the volume will be underestimated with MRAC without bone before final scaling is applied, and 2) the MC method used for scatter sinogram scaling produces a *lower scaling parameter k* (eq. 17) when using MRAC without bone. The effect of the latter is larger, as the difference in scatter sinograms after step 1) is highly noticeable, as was confirmed by extraction and comparison of scatter sinograms between TF-SSS and MC-SSS. The effect in 2) is due to the sensitivity of the MC method to the accuracy of the input images, already noted by Holdsworth et al., (Holdsworth et al., 2002), who reported in their evaluation of MC-based scatter correction for 3D PET that error in the input images, particularly in the attenuation image, will result in error in simulation sinograms and images.

Therefore, an attenuation map with lower attenuation coefficients will produce a slightly lower scatter estimate locally and also a lower *scaling factor k* in the MC-SSS simulation. This was confirmed by investigation of the derived scaling factors in MC-SSS with one patient with CTAC and $\mathrm{MRAC}_{\mathrm{2class}}$. CTAC resulted in a higher scaling factor *k* over $\mathrm{MRAC}_{\mathrm{2class}}$ by 2.4 %, which is also consistent with the experimental results. As seen from (eq. 17), the scaling factor is affected by the SF derived from the MC simulation, the emission sinogram and the SSS derived scatter sinogram. It should be noted that the total effect of this scaling-dependent underestimation remains very minor, with an approximately 3 % difference in PET quantification between the attenuation maps in MC-SSS and this is a specific situation related only to using MRAC excluding bone in combination with MC-SSS.

One possible reason for a lower factor *k* would be deriving the scaling parameters by low-count MC simulation using both the data of the emission and transmission images. As the transmission images have decreased attenuation values in the MRAC without bone, the recovered activity in the MC simulation might be lower and the resulting scaling parameter determined will also be lower. However, this is challenging to confirm as not all the results of the MC simulation are accessible on the PET/MR system. Based on the data extracted from the system, it seems that when using CTAC, the MC simulation converges faster and reaches to a higher number of estimated scatter events compared to $MRAC_{2class}$.This in turn results to a higher *SF* and higher parameter *k* (eq. 17). Comparison of the scaling parameters seems to point to this as the cause. Therefore, the effect seen in MC-SSS is mainly due to the method used for scatter scaling and in this specific situation, SSS with tail fitting (TF-SSS) offers a more robust performance across different MR-based attenuation maps as it will scale the scatter estimate to the emission tails which are unaffected by the accuracy of the attenuation map.

Although the scatter shape is underestimated in TF-SSS, because of using transmission image values in the SSS equation (eq. 11), the scaling to emission sinogram tails outside the emission and transmission object seems to compensate this quite effectively. Thus, TF-SSS offers a reasonable estimate in cases where the attenuation coefficients are underestimated, there is no contamination between emission and transmission data (affecting tail scaling) and no other errors reside in the data which would compromise the emission tail quality. Finally, it should be emphasized that there are specific study conditions where another scaling method is preferred over TF-SSS. A very recent study showed favorable performance of MC-SSS over TF-SSS (Magota et al., 2017). There are also specific study situations where the sinogram scaling might be entirely omitted, and an absolute scaling method should be preferred (Hori et al., 2015; Heußer et al., 2017) or optionally limiting the derived scaling coefficients (Miwa et al., 2016). The author recommends that these study conditions be investigated in the future.

6.4.2 Main conclusion

This was the first time that two scatter correction methods for scatter scaling were compared with a brain phantom and clinical subjects using three attenuation maps of different accuracy in a clinical PET/MR system. Our study implies that scatter algorithm performance is not affected significantly by imperfections in MRAC in non-TOF ^{18}F-FDG imaging, especially with the TF-SSS algorithm.

6.5 Limitations and Recommendations:

6.5.1 Time-of-flight imaging in static and dynamic PET studies

TOF imaging has reduced sensitivity to errors in attenuation correction, as the cross-dependencies between individual images voxels are reduced in TOF reconstruction (Mehranian et al., 2015a). Recently, TOF imaging has been shown to be beneficial in reducing the quantitative errors due to MRAC in whole-body and brain (Mehranian et al., 2015a; Kahlife et al., 2017). Regional bias in the head region could be reduced, especially when ignoring bone attenuation. Therefore, a straightforward way to improve the results achieved in Studies (I) to (IV) as a whole would be to use TOF reconstruction.

A limitation of studies (I) to (IV) was that TOF reconstruction was not possible on the Ingenuity TF PET/MR system due to technical limitations alone, which plagued the system during the years 2013 to 2017. An interesting subject for future studies would be to apply and evaluate the benefit of TOF in conjunction with MRAC for both static and dynamic brain imaging. A recent study concluded that TOF was beneficial in improving quantitative accuracy across different MRAC methods (Kahlife et al., 2017). The author is currently in the process of implementing and validating a TOF capable reconstruction protocol for brain-specific applications and eventually for dynamic studies for brain and whole-body for the Ingenuity TF PET/MR.

It is evident that developments in PET detector technology will have an impact on future clinical PET/MR systems (Herzog et al., 2016). The use of TOF is expected to increase with the next generation of PET/MR systems as the introduction of MR-compatible and fast PET detector modules such as SPiMs, have made it possible to achieve a timing resolution favorable for TOF imaging. Further advances in detector technology should be beneficial for future PET/CT systems as well. Increases in TOF resolution are expected to bring benefits to PET quantification and implementation of novel attenuation correction methods using e.g. MLAA (Nyuts et al., 1999). The author recommends that future evaluations of the subject covered in Studies (I) to (IV) be made with TOF-capable PET/MR or PET/CT systems.

6.5.2 Challenges, Limitations and Recommendations on using CTAC data for validation

One limitation concerning our studies (I to IV) is that CTAC was used for validation in all of the studies. It should be noted that CTAC is not the gold standard for attenuation correction.

In general, this makes the comparison between the proposed MRAC methods in the literature quite challenging, since differences in how both the MRAC and the CTAC data are processed (e.g. registered), converted to linear attenuation coefficients (there are at least three conversion methods available) and reconstructed will affect the results derived from the PET images. Additional differences are a result of small post-processing differences in the attenuation maps and the selection of attenuation coefficients between different studies. Since the differences that are compared between individual MRAC methods are in the range < 5 %, small changes might hinder the comparison of method performance.

Ensuring that the CTAC reference is created very carefully is essential. Thus, using manual delineation to ensure that all structures in the CT are included is recommended, if feasible. In addition, soft tissue needs to be added if the CT-based attenuation map did not cover the entire PET FOV. Although not included in this evaluation, we simulated this condition and compared the PET data using truncated CT data and noted that the differences between using truncated and non-truncated CTAC would result in an absolute bias on average of 1.2 % to 1.5%, with truncated CT giving a lower bias when compared to MRAC. Rausch et al., had similar results in their comparison of truncated and non-truncated CTAC data (Rausch et al., 2017). Sadly, there is not yet a standardized and unified analysis methodology in MRAC validation to follow; this should be addressed in the future.

6.5.3 Attenuation coefficient selection for segmentation-based MRAC

The selection of a proper attenuation coefficient for segmentation-based MRAC remains the main limitation of methods with discrete attenuation coefficients. Thus, the attenuation coefficient selected on the basis of the literature or a measured value will vary individually among the patient population in the study. However, even if attenuation coefficients are derived from measurements of large populations, measurements from individual patient data will always contain some bias, due to the accuracy of the VOI analysis implemented, the transformation of HU values to attenuation coefficients (where the implemented bilinear transform will cause some variation), the patient group in question (young or elderly) and the statistical quantity from which the final attenuation coefficients are derived (e.g.

mean, median, peak of histogram). Therefore, it is recommended to select attenuation coefficients based on established standards, such as the ICRU-104, as was done by (Zaidi et al., 2003b). In essence, selection of a discrete attenuation coefficient is always a trade-off between bias within a subject and variation among a population, as homogeneity of the attenuation coefficients within the population and within a tissue class is assumed.

In study (II), using 0.145 cm-1 for the skull bones proved to be the best trade-off in this study, which is in accordance with earlier reports (Catana et al., 2010, Anazodo et al., 2015). This was also close to the mean attenuation coefficient of bone measured from the CTAC in the patient group. In study (III), we used an empirical measure for the attenuation coefficients for different tissues using a separate patient group. Although not included in this study, we also used values of 0.096 cm-1, 0.0985 cm-1, 0.0965 cm-1 and 0.151 cm-1 for soft tissue, GM/WM, CSF and bone, respectively. These values were originally selected from the literature review and in comparison with the measurement of attenuation coefficients derived from the CTAC. We measured the difference between PET images reconstructed with these attenuation coefficients and the attenuation coefficients used in study (III) and noted a 0.8 % to 1 % difference in VOI analysis. The largest difference was noted in the CSF region, approximately 1.5 % in magnitude. The 5-class method as stated above achieved a lower bias compared to 4-class and 6-class methods in the study.

Different attenuation coefficients for bone were evaluated as part of studies (II) and (III), where a conclusion similar to that of Catana et al., (Catana et al., 2010) was reached: an attenuation coefficient between 0.145 cm-1 and 0.151 cm-1 is the best trade-off between bias and variability for bone. Similarly concerning brain tissues, an attenuation coefficient of 0.0974 cm-1 to 0.099 cm-1 would be sufficient to cover a range of attenuation values for the GM and WM, based on the results of Study (III). Since these two brain tissues have very similar attenuation coefficients, they could be combined into a single tissue class as stated above. In the study of (Son et al., 2010), a value of 0.0994 cm-1 and 0.0993 cm-1 were measured for the brain tissue using the same CT transform as our study and determined to be sufficient. However, (Son et al., 2010) studied brain tissue in general and did not account for the variation of attenuation coefficients between GM, WM and CSF. Therefore, a lower attenuation coefficient for CSF in the range of 0.096 to 0.097 cm-1 would be preferable, close to the value of 0.0965 cm-1 as suggested by (Ladefoged et al., 2015). It should be emphasized that the selection of a single attenuation coefficient for brain would imply a tradeoff between variation and bias, similar to bony tissue.

We did not account for specific pathological conditions in the bone or brain tissue in these studies. Patient groups with a known condition of reduced bone mineral density (osteopenia or osteoporosis) might need a separate weighting factor to take into account the reduced amount of bone. There are also anatomical areas in the head region which may benefit from individual segmentation and attenuation coefficients. Other areas which are commonly considered challenging for segmentation and selection of attenuation coefficients are the mastoid cells and the sinus cavities. These could be accounted for separately by using discrete masks and attenuation coefficients assigned for each area as in (Lagefoed et al., 2015) and (Yang et al., 2017b). Another area which might pose a challenge is be the frontal air space. However, the author is unaware of any reports which estimate the accuracy of segmentation specifically in this area.

However, the effect of incorrect bone segmentation and attenuation value assignment might not always be significant. Aznar et al., showed in a study of MRAC in oncological whole-body imaging that the assignment of a spongeous bone value of (0.13 cm-1) to all bones resulted in a less than 5 % quantification bias for soft tissue and bone lesions (Aznar et al., 2014). However, 7 to 16 % underestimations were seen in spine lesions. In addition, Keereman et al., concluded in their simulation study that up to 20 % misclassification of bone would result in errors below 5 % (Keereman et al., 2011), which could be adopted as future reference criteria when evaluating new MRAC methods.

Ultimately, methods that allow the derivation of subject-specific attenuation coefficients in segmentation-based MRAC are desired and will circumvent most problems mentioned in this section. Such methods have been introduced using ZTE and UTE sequences (Khalife et al., 2017; Ladefoged et al., 2017) which should prove useful in the further development of segmentation-based MRAC further. Alternative methods are well worth investigating.

6.6 Future Prospects:

6.6.1 Using MR-based Attenuation Correction in Clinical Routine

It can be seen from study (I) - from a clinical perspective, that using a registered patient CT scan or TX scan for MRAC should reduce the bias in PET/MR images to a level seen in PET/CT. This would us to achieve attenuation correction for PET/MR scans as good as the registration accuracy of the CT or TX scan allows. However, some disadvantages regarding clinical workflow and additional costs, for example, can be seen with this approach. 1) The clinical workflow has to be changed to include an additional CT scan. 2) The registration accuracy of CTAC will affect quantitative accuracy in clinical studies, as has been hypothesized (Sekine et al., 2016). The phantom used in study (I) offers nearly ideal registration accuracy as it has rigid anatomy. 3) The radiation burden of the subject is increased and 4) the advantage of having a "one-stop" PET/MR examination is lost.

Therefore, once an effective solution for MRAC for the clinical application and workflow is found and validated, it should be implemented in the clinical routine. In addition, it has been reported that even using MRAC without bone does not hinder clinical decision making (Rausch et al., 2017; Su et al., 2016; Werner et al., 2016). Lately, with all the advances made in the field of MRAC in PET/MR imaging, implementing optimized reconstruction protocols, TOF imaging and novel MRAC may improve the quantitative performance without the need for CTAC. Thus, PET/MR systems should eventually move from using CTAC and TXAC (which have their own inherent limitations as well) as an interim solution to using fully MR-based attenuation correction. At the end of the day, while any MR-based attenuation correction method will eventually be but a compromise, CTAC has its own limitations as well. A recent, large multi-center study shows promising results which would eventually promote the applicability of MRAC in clinical routine (Lagefoed et al., 2017).

6.6.2 Applicability to other radiotracers

Due to the developments achieved in the field of PET/MR imaging since 2010 and due to the analyses and technical improvements described in this thesis (Studies I to IV), MRAC can no longer be considered a critical issue for PET quantification when using ^{18}F-FDG. Therefore, the technical status of clinical brain PET/MR imaging using ^{18}F-FDG can be considered to be currently in a very good state. This concerns both the applicability of available attenuation and scatter correction methods for PET data quantification purposes.

This would warrant going forward in adaptation of PET/MR imaging in the clinical routine for neuro-degenerative diseases with investigation of advanced applications for dementia and neurocognitive disorders. Further investigations on improving MRAC in the field are still encouraged, especially for applying them to kinetic modeling or MR-based radiotherapy applications. This applies also to novel methods adapted for scatter correction. For data quantification purposes using kinetic modeling, it is essential that the bias in regions of interest used for estimation of derived parameters is minimized to the best possible degree. This concerns mainly brain receptor studies using ^{11}C-tracers, such as ^{11}C-Raclopride or when studying cerebral perfusion with ^{15}O-H_2O or similar tracers.

A few studies have looked at the effect of scatter compensation on parameter estimates derived from kinetic models in 3D brain PET studies with various tracers (Myers et al., 1996; Cherry et al., 1995; Hori et al., 2015; Magota et al., 2017). Ten years later, it can be concluded similarly to (Zaidi et al., 2007) that further studies are necessary using different PET tracers in various clinical situations to fully characterize the effect of both MR-based attenuation and scatter correction on the estimation of tracer kinetic parameters.

Developments achieved in the MRAC field and in new and accurate methods for scatter correction are beneficial for both visual and quantitative analysis when other radiotracers other than ^{18}F-FDG are used, such as ^{11}C-PiB. Radiotracers which are analyzed using visual analysis will also benefit from advances in attenuation and scatter correction methods, such as amyloid tracers. The visual analysis in amyloid tracers is mainly based on the identification of neocortical gray matter–versus–white matter contrast where the loss of this contrast points to amyloid positivity and vice versa (Barthel and Sabri et al., 2017). Consequently, methods validated for ^{18}F-FDG should be applicable for radiotracers with similar uptake patterns.

6.6.3 Applicability to MR-based radiotherapy and neuro-oncology

It should be emphasized that the conclusions in this thesis mainly concern normal adult brains imaged with ^{18}F-FDG, a typical population suspected of neurodegenerative disorders. With the increase in MR-based radiotherapy planning (MR-RT), application of MRAC methods to MR-RT should be investigated. Using PET/MR imaging would be preferable for neuro-oncology in which the utmost precision and same time-point imaging are required (Dickson et al., 2014). The creation and evaluation of pseudo-CT for both MRAC and MR-RT have been shown feasible for the pelvic area in recent reports (Arabi et al., 2016), as well as in brain (Edmund et al., 2017). These pseudo-CT methods have been adopted into clinical use in few advanced radiotherapy sites.

However, neuro-oncological patients are in general more challenging in terms of MRAC if post-operation or post-treatment imaging is performed. This is mainly due to anatomical deformations caused by tumor growth or surgical operations. This might create challenges in the creation of subject-specific attenuation maps. An interesting research subject in the future will most likely be the performance evaluation of MRAC-based methods and the method presented in this work in neuro-oncological patients with large or small brain tumors, surgical resection and in the presence of metal implants. These subjects could be a typical cohort undergoing PET/MR-based, MR-RT. Further investigations into using MRAC methods for MR-RT in the field of neuro-oncology are therefore highly recommended.

It is also reasonable to assume that the method presented in Studies (II, III) might be less robust when anatomy is deformed or when MR images have areas of void signal due to metal implants. This is an inherent limitation, as the method is largely based on MR image segmentation. We have evaluated the method developed in Studies (II) and (III) with a small group of glioblastoma patients, with fairly promising initial results. However, we were not able to perform a quantitative evaluation with PET. A group of glioblastoma patients was included in the development and evaluation of another SPM8-based method (Izquierdo-Garcia et al., 2014; Chen et al., 2017). However, these methods and the method in studies (II) and (III) are not entirely comparable due to the differences in deriving the attenuation map.

A larger clinical evaluation with a patient group with deformed anatomy should be performed in the future with the methods described in Studies (II) and (III). Neuro-oncological imaging has more requirements in terms of the robustness of the attenuation map, although a recent study shows promising results for an MRAC method in a group of patients with brain tumors (Rausch et al., 2017).

6.6.4 Future work on MRAC and scatter correction applicability in brain PET/MR imaging

Future work includes improving the MRAC method developed in studies (II) and (III) further by implementing subject-specific continuous bone attenuation values and the application of the method to dynamic brain PET imaging to study the effect of MRAC on kinetic parameters derived from PET images. Methods to include additional tissue classes (e.g. mastoid cells) not included in studies (I-IV) should be investigated. Eventually, the ultimate goal would be to move to full pseudo-CT creation from MR images. Furthermore, the effect of TOF imaging for improving the quantitative accuracy of PET images when using MRAC and TOF-dependent scatter estimate should be investigated as a continuation of this study using different radiotracers than ^{18}F-FDG (IV).

6.6.5 Extension of scatter correction evaluation to whole-body PET/MR and PET/CT imaging

The work of Study (IV) focused on the evaluation of scatter correction in ^{18}F-FDG brain imaging with issues specific for PET/MR imaging. However, there are issues in whole-body PET/MR imaging which prompt the performing of additional evaluations for novel scatter correction methods such as MC-SSS. One such issue is the robustness of different scatter correction algorithms in the presence of a large amount of out-FOV scatter, which is more of an issue in whole-body studies. Other issues specific for whole-body imaging include: ^{68}Ga prostate-specific membrane antigen (PSMA) studies which exhibit high accumulation in bladder and kidneys (60-100 target to background ratio) (Heußer et al., 2017), truncation due to limited MR FOV, lung segmentation issues, respiratory and cardiac movement in thorax area and void areas due to implants. These could be conducted as a future work and extension of study (IV).

7 CONCLUSIONS

Quantitative accuracy in ^{18}F-FDG brain PET/MR is well comparable to PET/CT once an MRAC method which achieves accuracy close to CTAC is used for attenuation correction. Thus, the essential requirement to minimize the differences between PET/MR and PET/CT systems is an accurate attenuation map. Additionally, using an accurate attenuation map in PET/MR imaging will also minimize the bias introduced by scatter correction.

An MRAC method using only T1-weighted MR images was introduced, validated and further developed using only a freely available and distributable software. The method has an acceptable accuracy for quantification of gray matter radioactivity in ^{18}F-FDG brain PET/MRI imaging, which is below the accepted limit of SUV bias (< 10 %) with the basic version and below SUV reproducibility (< 5 %) with the advanced version, for the majority of the gray matter regions. A codebase for the method is available on the Internet (http://bit.ly/2fx6Jjz) – for free use, modification and distribution.

Concerning the accuracy of the scatter correction algorithm when used with MRAC, no significant changes in either the approximated scatter shapes or quantitative accuracy of the PET images were detected with two scatter scaling methods, the TF-SSS and the MC-SSS. Therefore, scatter correction is not an issue with non-TOF ^{18}F-FDG brain imaging, even when using an imperfect MR-based attenuation map without bone.

In conclusion, the technical status of ^{18}F-FDG brain PET/MRI imaging is currently very good due to several methodological advancements made since 2010. This has significant implications for the clinical adaptation of ^{18}F-FDG PET/MR in imaging and clinical diagnosis of neurodegenerative diseases.

ACKNOWLEDGEMENTS

This study was conducted within the Finnish Center of Excellence in Molecular Imaging in Cardiovascular and Metabolic Research at the Turku PET Centre, Department of Clinical Physiology and Nuclear Medicine in Turku University Hospital and University of Turku, Turku, Finland during November 2013 to February 2018 and in the department of Department of Investigative Radiology, National Cardiovascular Center Research Institute, Osaka, Japan during September 2014 to March 2016.

First and foremost, thanks be to God! Like apostle Paul states in his letter to the Corinthians: “But thanks be to God, who gives us the victory through our Lord Jesus Christ.” (1 Cor. 15:57, ESV). I have a lot to be thankful of and I have been blessed greatly in my life and in my work through Him. What is impossible to me, is possible to Him. Where my strength ends, His strength begins: “My flesh and my heart may fail, but God is the strength of my heart and my portion forever.” (Psalm 73:26). As Christ himself states: “Apart from me you can do nothing” (John 15:5) and likewise Paul “I can do all things through Christ who strengthens me” (Philippians 4:13). Without Him, I can do nothing, I am nothing and I have nothing. However, in Him – I already have everything! “Whom have I in heaven but you?” (Psalm 73:25). Thanks be to God!

Second, I want to thank my lovely wife and my best friend, Elina. You are a gift, a precious gem far more worth than rubies (Proverbs 31:10) and the love of my life. It is amazing that I never knew you when I started this thesis work and for the short time we have been together, since my arrival from Japan in 2016 – I would never imagine to be a husband to someone else but you. I am very blessed to be your husband and you are a daily blessing in my life. My gratitude is yours, for the love, support and patience in sharing your life and most importantly, sharing your faith with me every day. You are my strong helper (ezer), you inspire me to grow more like Christ every day and you inspire me to be the best husband to you.

Third, I express my sincere gratitude to the former professor Jaakko Hartiala (head of the department of Clinical Physiology and Nuclear Medicine at the beginning of the study) and especially to Professor Juhani Knuuti, the Director of Turku PET Centre and the Head of the Department of Clinical Physiology and Nuclear Medicine, for providing such excellent research facilities and every kind of support for executing this project. I also want to acknowledge Professor Hidehiro Iida for hosting me for nearly two years from September 2014 to March 2016 in NCVC, Osaka and providing every kind of support possible for conducting my research projects in a high-level, national Japanese institute and beyond. I also want acknowledge Ms. Yuka Tsuji for her friendship and all the support for during my stay in Japan.

I think I now have a mother in both Finland and in Japan. I wish I could have stayed there longer, but if that had happened, I would never have met my future wife.

Then, I wish to express my deepest gratitude to my supervisors, Prof. Mika Teräs and Prof. Hidehiro Iida, for their expertise, for their support and help in making this thesis work a reality. I have been impressed by your enthusiasm, talent and experience in PET instrumentation, PET modelling and PET image quantification. Without your help, support and expertise, this thesis and many other works done beside it would never have been made. I especially want to thank Prof. Iida for hosting my stay in Osaka for nearly two years – those years in Japan were definitely the best time of my life that far and a beginning for something entirely new. I also want to acknowledge Prof. Teräs for giving me every kind of support needed, his experience and giving me the liberty to experiment and try out my skills in so many things with PET instrumentation, fixing and calibrating the HRRT, dual gating, PET reconstruction, MRI and the like. You both are greatly acknowledged for supervisors and more importantly, friends.

My best thanks also go to Prof. Hannu Eskola for his work in my supervisory group for my PhD work and especially his expertise already during my Master's and Bachelor's thesis in Technical University of Tampere (TUT), both of which got me interested to go further and pursue a career in medical imaging sciences. I especially want to thank Tanja Hasu, whose courses in radiation biology sparked initially my interest in the Medical Physics field in 2006, which I still have up to this day. Last but not least, from my TUT days I want to acknowledge Prof. Ulla Ruotsalainen, also a former laboratory engineer in Turku PET Centre, who’s lectures in PET image reconstruction and signal processing in TUT inspired me to learn more deeply about both subjects, which I use in my current work on a daily basis.

I want to acknowledge both Prof. Ronald Boellaard and Prof. Hans Herzog for the pre-examination of this thesis, for their valuable time they used to review and improve the quality of the thesis manuscript, all the comments and feedback. I want to thank you both for putting such an efficient effort and work to finish the review in the intended time schedule. I especially want to thank Prof. Herzog for his experience and knowledge and the discussions we had during the thesis review through Skype, which I greatly enjoyed. At this point, I would also like to acknowledge Jacquiline Välimäki for improving my lousy English for the thesis summary – with many thanks for the fast and efficient review.

I would also like to thank all of the professors and investigators in Turku PET Centre whom I have had the privilege to work with. I have had the privilege to contribute to several projects of yours, whom I would like to especially acknowledge Prof. Antti Saraste for the cardiac PET and dual gating PET projects, Prof. Marko

Seppänen and Prof. Jukka Kemppainen for the respiratory gating projects in oncology, Prof. Heikki Minn in the FLUCIPRO trial and many others, Prof. Anne Roivainen for the animal MRI projects, Prof. Juha Rinne and Lauri Nummenmaa for the neurology projects and MRI projects of the brain, Prof. Merja Haaparanta-Solin and Tove Grönroos and Olof Solin for the latest projects in animal PET/CT.

For actually conceiving this thesis work into publications and finalizing it – no one can do it alone. I am deeply indebted to every of my co-authors for each of the work done in each of the individual publications. From Turku PET Centre I would like to thank especially Jarkko Johansson and Jouni Tuisku for their expertise in brain PET analysis and modelling. Jani Linden for his great talent in mathematics and programming, Antti Karlsson for his great talents in physics and programming - you two are definitely smarter than I ever will be. I would also like to give my sincere thanks to Virva Saunavaara for her great expertise in MRI and help with the phantom studies and especially to Tuula Tolvanen with her great expertise on phantom studies – you are a true “phantom wizard”. Finally, my gratitude goes to Terhi Tuokkola for helping us scientists to understand the radiologist’s point of view in our PET, CT and MRI studies.

I also want to acknowledge all my wonderful colleagues and co-authors in international instutions, especially the “Rigshospitalet team”: AE Hansen, S Holm and S H Keller – without your support, insight and feedback the first publication would never have been finished. I also like to thank G Delso and P Veit-Haibach for their extensive work on getting the final PET/MR system for this paper on board. Last but not least, I want to especially thank Dr. K Magota from Sapporo, whom I had the privilege to work with for a short time in Japan and luckily even further beyond my stay in Osaka. I am deeply indebted to you all. Related to these studies, I also want to acknowledge the 3D printed Iida brain phantom, which has been my travel companion in my trips to Denmark, Sapporo and Canada. He is a quiet but efficient guy who gets the job done.

I want to acknowledge all my fellow co-workers in Turku PET Centre and in NCVC, whom I had the privilege of spending time and working with, especially to Marko and Rami for their excellent support in IT and always willing to listen to my silly requests about IT matters, Hannu for his great knack on building gadgets for everything needed in PET, Vesa for his extensive Wiki page and his great knowledge in PET image modelling, Chunlei for his enthusiasm and work with Carimas, our coders Timo and Sauli who have empathically listened my software requests, Harri for this great work in programming in general, and the physicist team in Turku University Hospital, especially to Kalle Koskensalo with the help of establishing many practical items for our animal MRI system. A special thanks

goes to Tuomas Koivumäki and the Bioimpedance project, which were a starting point for my scientific career in Turku PET Centre.

From NCVC, I want to thank all of my colleagues from Japan and from Germany whom I had the privilege to work with for almost two years in Osaka. I would like to especially thank Dr. Takashi Temma, Dr. Satoshi Iguchi, Dr. Emni, Dr. Koshino, Dr. Makoto Yamazaki, Sanda-san and many others who were my "family" during that time. Thank you for your hard work and your kind hospitality for everything. If it is ever possible, I would like to work again with you all, please come and visit Finland soon! My special thanks go to Dr. Hans Wehrl and Mario Amend, who visited us in NCVC during the hot Osakan summer in 2015. Although your visit was brief, it was wonderful to share my experience with you two.

My special thanks for this thesis goes to the all of the Turku PET Centre technologists, radiographers and laboratory staff whom I've had a great experience to work with and all the things I have actually learned from you when spending the time either on the PET/MR, PET/CT or HRRT. My special thanks goes to you all, especially Anne-Mari for her great practical experience on the PET/MR system, Minna Aatsinki for always finding time to do the reservations for the animal or phantom experiments and the infamous "PET dual gating team": Henna, Silja, Aliisa, Tiina and the rest. I sincerely tried to list you all, with my best thanks to: Tarja, Marjo, Hannele, Sanna, Heidi, Pauliina, Pirkko, Johanna, Eija and many others. I would also like to thank the animal PET/CT and MRI team for their help and the support for the MRI side projects: my thanks goes to Aake, Jenni & Heidi & Riikka for their animal handling expertise and to Petri and Sina for making those MRI projects eventually a reality.

To those whom I have forgotten from the previous list, this one is for you: I want to express my sincere gratitude to all the people I have had the privilege to work with in Turku PET Centre since 2011. I want to thank my fellow co-workers and researchers for creating such an easy-going atmosphere and just for a fun and easy place to conduct your work. I love you all.

I also want to acknowledge my brothers and sisters in Christ in both Finland and Japan. Without your support and especially your prayers, I never would have made this far. As Paul states in the letter to Philippians 1:9-11 (ESV): "9 And it is my prayer that your love may abound more and more, with knowledge and all discernment, 10 so that you may approve what is excellent, and so be pure and blameless for the day of Christ, 11 filled with the fruit of righteousness that comes through Jesus Christ, to the glory and praise of God."

I want to express my gratitude to Pastor Kondo at Hamadera Bible Church (HBC) in Sakai, for his faithful preaching and love for the Word. I especially want to thank

Chris, Yoshiki, Ash, Tami-chan, Takashi H, Takashi K, Janelle, Kat, Imasaka-san and his wife, Hikawa-san and his wife, Kitaoka-san and his wife, Narita-san and his wife, Hibino-san and many others I have already forgotten and had the privilege to fellowship during my time in Japan and all the Bible studies we had through Skype. I still have your "Thank you" note for our wedding. I would also like to acknowledge Ms. Toyoda-san for letting me to teach at their Bible study, it was really a blessing to me. Finally, I especially want to acknowledge Grace, who lead me eventually to HBC and back to the Lord after several years I spent lost: "for this your brother was dead, and is alive; he was lost, and is found" (Luke 15:32).

I want to express my gratitude to the people I've had the privilege to meet at Turun ev.lut. Opiskelija- ja Koululaislähetys (Turun OPKO) for the last two years. My best regards go to Markus & Kiia and family, Eveliina, Mirjami, Tiina, Mika, Mikko, Juuso and Ilona and all of the other regulars whom I've had the privilege to spend time with. I also want to thank our student workers Mikko and Robert for all the fun times we had together, for their encouragement and support, helping us with the program and logistics for every spring, summer and fall and for letting me to lead the Bible studies almost two years in a row. I hope the Lord will bless you all after I am now, at the end of the graduation and "retirement" from OPKO.

My deepest hope and a fervent prayer was that after moving to Finland I would find find a good, loving and faithful congregation also from Finland, where I could settle as my "home". And eventually I did find one. I am deeply indebted to the Lutheran Congregation of St. Paul and all the people there, for giving me a home that I longed for so long. I want to express my gratitude especially to Pastor Sebastian for his great sermons on every Sunday and his easy-going attitude and kindness. I would also like to knowledge Eero for his positive and sincere attitude and the great knowledge he has about the Bible. Here are my deepest thanks to you all: Matthew and Martta and family, Mikko and Anne and family, Jaakko and Aili, Risto and Jenni and family, Erik and Riitta, Jorma and Raili, Anssi and Suvi, Soila and many others that I have forgotten. Grace, Peace and Mercy from our Lord.

Finally, I want to express my gratitude to my friends, relatives and especially my parents Raija and Raimo. I think you have always been a great encouragement to me, pressing me onward to continue with my studies and encouraging me when I have been down. You have unselfishly given your love and support for me during all of these years, through the good times and the bad times. I value deeply for your ever-loving, unselfish attitude for me and my work with always having the time for me, even though I have not been able to see you as often as I would have liked. With this thesis out of the way, I hope we could share the time together again during those beautiful summer days in the countryside as we did in the past.

Last but not least, I want to thank not just Turku PET Centre, University of Turku and also Turku University Hospital for the monetary support and salary throughout all of these years but also all of the foundations and monetary sources that have provided support for making this thesis a reality. Without this support and time relieved to focus on research, analysis and writing, this thesis would have been never finished. Therefore, this financial support is greatly acknowledged.

This study was financially supported by the Alfred Kordelin Foundation (Alfred Kordelinin säätiö) and the Finnish Cultural Foundation, Varsinais-Suomi Regional fund (Suomen Kulttuurirahaston Varsinais-Suomen rahasto). Financial support was also received from Hospital District of Southwest Finland (EVO- and ERVA-funding, project number 13236) and the funding from University of Turku Graduate School (UTUGS) funded doctoral position in the Doctoral Programme in Clinical Research. Finally, I would like to acknowledge the unique opportunity provided by the Academy of Finland in funding in the strategic Japanese-Finnish research co-operation on "Application of Medical ICT Devices" supported by both the Academy of Finland (project number 269977), University of Turku, Turku University Hospital, and the Åbo Akademi University.

At the end, I only have one thing to say: "I wish I would and could have done more".

Turku, February 2018

Jarmo Teuho

ALFRED
KORDELININ
SÄÄTIÖ

VARSINAIS-SUOMEN KULTTUURIRAHASTO ⌘

REFERENCES

Accorsi R, Adam L-E, Werner ME, Karp JS. Optimization of a fully 3D single scatter simulation algorithm for 3D PET. Phys Med Biol. 2004 Jun 21;49(12):2577–98.

Adam LE, Karp JS, Freifelder R. Scatter correction using a dual energy window technique for 3D PET with NaI(Tl) detectors. In: 1998 IEEE Nuclear Science Symposium Conference Record 1998 IEEE Nuclear Science Symposium and Medical Imaging Conference (Cat No98CH36255). 1998. p. 2011–8 vol.3.

Aitken AP, Giese D, Tsoumpas C, Schleyer P, Kozerke S, Prieto C, et al. Improved UTE-based attenuation correction for cranial PET-MR using dynamic magnetic field monitoring. Med Phys. 2014 Jan 1;41(1):

Akbarzadeh A, Ay MR, Ahmadian A, Alam NR, Zaidi H. Impact of using different tissue classes on the accuracy of MR-based attenuation correction in PET-MRI. In: 2011 IEEE Nuclear Science Symposium Conference Record. 2011. p. 2524–30.

Akbarzadeh A, Ay MR, Ahmadian A, Alam NR, Zaidi H. MRI-guided attenuation correction in whole-body PET/MR: assessment of the effect of bone attenuation. Ann Nucl Med. 2013 Feb;27(2):152–62.

Anazodo UC, Thiessen JD, Ssali T, Mandel J, Günther M, Butler J, et al. Feasibility of simultaneous whole-brain imaging on an integrated PET-MRI system using an enhanced 2-point Dixon attenuation correction method. Front Neurosci. 2015;8:434.

Andreasen D, Van Leemput K, Hansen RH, Andersen JAL, Edmund JM. Patch-based generation of a pseudo CT from conventional MRI sequences for MRI-only radiotherapy of the brain. Med Phys. 2015 Apr;42(4):1596–605.

Andersen FL, Ladefoged CN, Beyer T, Keller SH, Hansen AE, Højgaard L, et al. Combined PET/MR imaging in neurology: MR-based attenuation correction implies a strong spatial bias when ignoring bone. Neuroimage. 2014 Jan 1;84:206–16.

Arabi H, Rager O, Alem A, Varoquaux A, Becker M, Zaidi H. Clinical assessment of MR-guided 3-class and 4-class attenuation correction in PET/MR. Mol Imaging Biol. 2015 Apr;17(2):264–76.

Arabi H, Koutsouvelis N, Rouzaud M, Miralbell R, Zaidi H. Atlas-guided generation of pseudo-CT images for MRI-only and hybrid PET-MRI-guided radiotherapy treatment planning. Phys Med Biol. 2016;61(17):6531–52.

Ashburner J, Friston KJ. Unified segmentation. Neuroimage. 2005 Jul 1;26(3):839–51.

Aznar MC, Sersar R, Saabye J, Ladefoged CN, Andersen FL, Rasmussen JH, et al. Whole-body PET/MRI: the effect of bone attenuation during MR-based attenuation correction in oncology imaging. Eur J Radiol. 2014 Jul;83(7):1177–83.

Bai C, Shao L, Silva AJD, Zhao Z. A generalized model for the conversion from CT numbers to linear attenuation coefficients. IEEE Transactions on Nuclear Science. 2003 Oct;50(5):1510–5.

Bailey DL. Transmission scanning in emission tomography. Eur J Nucl Med. 1998 Jul 1;25(7):774–87.

Bailey DL, Meikle SR. A convolution-subtraction scatter correction method for 3D PET. Phys Med Biol. 1994 Mar;39(3):411–24.

Bailey DL, Pichler BJ, Gückel B, Barthel H, Beer AJ, Bremerich J, et al. Combined PET/MRI: Multi-modality Multi-parametric Imaging Is Here: Summary Report of the 4th International Workshop on PET/MR Imaging; February 23-27, 2015, Tübingen, Germany. Mol Imaging Biol. 2015 Oct;17(5):595–608.

Bal H, Panin VY, Platsch G, Defrise M, Hayden C, Hutton C, et al. Evaluation of MLACF based calculated attenuation brain PET imaging for FDG patient studies. Phys Med Biol. 2017;62(7):2542.

Barney JS, Rogers JG, Harrop R, et al. Object Shape Dependent Scatter Simulations for PET. IEEE Trans Nucl Sci 1991;38:719–25.

Barthel H, Schroeter ML, Hoffmann K-T, Sabri O. PET/MR in dementia and other neurodegenerative diseases. Semin Nucl Med. 2015 May;45(3):224–33.

Bendriem B, Townsend DW. The Theory and Practice of 3D PET. The Netherlands:Kluwer Academic Publishers; 1998.

Benoit D, Ladefoged CN, Rezaei A, Keller SH, Andersen FL, Højgaard L, et al. Optimized MLAA for quantitative non-TOF PET/MR of the brain. Phys Med Biol. 2016 Dec 21;61(24):8854–74.

Bergström M, Litton J, Eriksson L, Bohm C, Blomqvist G. Determination of object contour from projections for attenuation correction in cranial positron emission tomography. J Comput Assist Tomogr. Apr 1982;6(2):365–72.

Berker Y, Franke J, Salomon A, Palmowski M, Donker HCW, Temur Y, et al. MRI-based attenuation correction for hybrid PET/MRI systems: a 4-class tissue segmentation technique using a combined ultrashort-echo-time/Dixon MRI sequence. J Nucl Med. 2012 May;53(5):796–804.

Berker Y, Kiessling F, Schulz V. Scattered PET data for attenuation-map reconstruction in PET/MRI. Med Phys. 2014 Oct;41(10):102502.

Berker Y, Li Y. Attenuation correction in emission tomography using the emission data—A review. Med Phys. 2016 Feb;43(2):807–32.

Bettinardi V, Presotto L, Rapisarda E, Picchio M, Gianolli L, Gilardi MC. Physical performance of the new hybrid PET⁄CT Discovery-690. Med Phys. 2011 Oct;38(10):5394–411.

Bezrukov I, Mantlik F, Schmidt H, Schölkopf B, Pichler BJ. MR-Based PET attenuation correction for PET/MR imaging. Semin Nucl Med. 2013 Jan;43(1):45–59.

Bezrukov I, Schmidt H, Gatidis S, Mantlik F, Schäfer JF, Schwenzer N, et al. Quantitative Evaluation of Segmentation- and Atlas-Based Attenuation Correction for PET/MR on Pediatric Patients. J Nucl Med. 2015 Jul;56(7):1067–74.

Boellaard R, Hofman MBM, Hoekstra OS, Lammertsma AA. Accurate PET/MR quantification using time of flight MLAA image reconstruction. Mol Imaging Biol. 2014 Aug;16(4):469–77.

Boellaard R, Rausch I, Beyer T, Delso G, Yaqub M, Quick HH, et al. Quality control for quantitative multicenter whole-body PET/MR studies: A NEMA image quality phantom study with three current PET/MR systems. Medical Physics. 2015 Oct 1;42(10):5961–9.

Brendle C, Schmidt H, Oergel A, Bezrukov I, Mueller M, Schraml C, et al. Segmentation-Based Attenuation Correction in Positron Emission Tomography/Magnetic Resonance: Erroneous Tissue Identification and Its Impact on Positron Emission Tomography Interpretation. Investigative Radiology. 2015 May;50(5):339–346.

Burgos N, Cardoso MJ, Thielemans K, Modat M, Pedemonte S, Dickson J, et al. Attenuation correction synthesis for hybrid PET-MR scanners: application to brain studies. IEEE Trans Med Imaging. 2014 Dec;33(12):2332–41.

Burgos N, Cardoso MJ, Thielemans K, Modat M, Dickson J, Schott JM, et al. Multi-contrast attenuation map synthesis for PET/MR scanners: assessment on FDG and Florbetapir PET tracers. Eur J Nucl Med Mol Imaging. 2015 Aug;42(9):1447–58.

Burger C, Goerres G, Schoenes S, Buck A, Lonn AHR, Von Schulthess GK. PET attenuation coefficients from CT images: experimental evaluation of the transformation of CT into PET 511-keV attenuation coefficients. Eur J Nucl Med Mol Imaging. 2002 Jul;29(7):922–7.

Burgos N, Thielemans K, Cardoso MJ, Markiewicz P, Jiao J, Dickson J, et al. Effect of scatter correction when comparing attenuation maps: Application to brain PET/MR. In: 2014 IEEE Nuclear Science Symposium and Medical Imaging Conference (NSS/MIC). 2014. p. 1–5.

Cabello J, Lukas M, Förster S, Pyka T, Nekolla SG, Ziegler SI. MR-based attenuation correction using ultrashort-echo-time pulse sequences in dementia patients. J Nucl Med. 2015 Mar;56(3):423–9.

Carney JPJ, Townsend DW, Rappoport V, Bendriem B. Method for transforming CT images for attenuation correction in PET/CT imaging. Med Phys. 2006 Apr;33(4):976–83.

Catana C, van der Kouwe A, Benner T, Michel CJ, Hamm M, Fenchel M, et al. Toward implementing an MRI-based PET attenuation-correction method for neurologic studies on the MR-PET brain prototype. J Nucl Med. 2010 Sep;51(9):1431–8.

Censor Y, Gustafson DE, Lent A, Tuy H. A New Approach to the Emission Computerized Tomography Problem: Simultaneous Calculation of Attenuation and Activity Coefficients. IEEE Transactions on Nuclear Science. 1979 Apr;26(2):2775–9.

Chen CH, Muzic RF Jr, Nelson AD, et al. A Nonlinear Spatially Variant Object-dependent System Model for Prediction of Partial Volume Effects and Scatter in PET. IEEE Trans Med Imaging. 1998;17:214–27

Chen Y, Juttukonda M, Su Y, Benzinger T, Rubin BG, Lee YZ, et al. Probabilistic Air Segmentation and Sparse Regression Estimated Pseudo CT for PET/MR Attenuation Correction. Radiology. 2015 May;275(2):562–9.

Chen KT, Izquierdo-Garcia D, Poynton CB, Chonde DB, Catana C. On the accuracy and reproducibility of a novel probabilistic atlas-based generation for calculation of head attenuation maps on integrated PET/MR scanners. Eur J Nucl Med Mol Imaging. 2017 Mar;44(3):398–407.

Cheng J-CK, Salomon A, Yaqub M, Boellaard R. Investigation of practical initial attenuation image estimates in TOF-MLAA reconstruction for PET/MR. Med Phys. 2016 Jul;43(7):4163.

Cherry SR, Huang S-C. Effects of scatter on model parameter estimates in 3D PET studies of the human brain. IEEE Transactions on Nuclear Science. 1995 Aug;42(4):1174–9.

Clinthorne NH, Fessler JA, Hutchins GD, Rogers WL. Joint maximum likelihood estimation of emission and attenuation densities in PET. In: Conference Record of the 1991 IEEE Nuclear Science Symposium and Medical Imaging Conference. 1991. p. 1927–32 vol.3.

Conti M. Why is TOF PET reconstruction a more robust method in the presence of inconsistent data? Phys Med Biol. 2011 Jan 7;56(1):155–68.

Defrise M, Rezaei A, Nuyts J. Time-of-flight PET data determine the attenuation sinogram up to a constant. Phys Med Biol. 2012;57(4):885.

Delso G, Fürst S, Jakoby B, Ladebeck R, Ganter C, Nekolla SG, et al. Performance measurements of the Siemens mMR integrated whole-body PET/MR scanner. J Nucl Med. 2011 Dec;52(12):1914–22.

Delso G, Martinez-Möller A, Bundschuh RA, Ladebeck R, Candidus Y, Faul D, et al. Evaluation of the attenuation properties of MR equipment for its use in a whole-body PET/MR scanner. Phys Med Biol. 2010 Aug 7;55(15):4361–74.

Delso G, Carl M, Wiesinger F, Sacolick L, Porto M, Hüllner M, et al. Anatomic Evaluation of 3-Dimensional Ultrashort-Echo-Time Bone Maps for PET/MR Attenuation Correction. J Nucl Med. 2014 May 1;55(5):780–5.

Delso G, Zeimpekis K, Carl M, Wiesinger F, Hüllner M, Veit-Haibach P. Cluster-based segmentation of dual-echo ultra-short echo time images for PET/MR bone localization. EJNMMI Phys. 2014 Jun 4;1.

Delso G, Wiesinger F, Sacolick LI, Kaushik SS, Shanbhag DD, Hüllner M, et al. Clinical evaluation of zero-echo-time MR imaging for the segmentation of the skull. J Nucl Med. 2015 Mar;56(3):417–22.

De Dreuille O, Strijckmans V, Ameida P, Loc'h C, Bendriem B. Bone equivalent liquid solution to assess accuracy of transmission measurements in SPECT and PET. IEEE Transactions on Nuclear Science. 1997 Jun;44(3):1186–90.

Dickson JC, O'Meara C, Barnes A. A comparison of CT- and MR-based attenuation correction in neurological PET. Eur J Nucl Med Mol Imaging. 2014 Jun;41(6):1176–89.

Drzezga A, Barthel H, Minoshima S, Sabri O. Potential Clinical Applications of PET/MR Imaging in Neurodegenerative Diseases. J Nucl Med. 2014 Jun 1;55(Supplement 2):47S–55S.

Dukart J, Mueller K, Horstmann A, Barthel H, Möller HE, Villringer A, et al. Combined Evaluation of FDG-PET and MRI Improves Detection and Differentiation of Dementia. PLoS One. 2011 Mar 23;6(3).

Edmund JM, Nyholm T. A review of substitute CT generation for MRI-only radiation therapy. Radiat Oncol. 26. tammikuuta 2017;12(1):28.

Evans R. The Atomic Nucleus. McGraw Hill Book Company, Inc., New York (1955). 972 pp.

Fei B, Yang X, Nye JA, Aarsvold JN, Raghunath N, Cervo M, et al. MR/PET quantification tools: Registration, segmentation, classification, and MR-based attenuation correction. Med Phys. 2012 Oct;39(10):6443–54.

Gaens M, Bert J, Pietrzyk U, Shah NJ, Visvikis D. GPU-accelerated Monte Carlo based scatter correction in brain PET/MR. In: 2013 IEEE Nuclear Science Symposium and Medical Imaging Conference (2013 NSS/MIC). 2013. p. 1–3.

Grant AM, Deller TW, Khalighi MM, Maramraju SH, Delso G, Levin CS. NEMA NU 2-2012 performance studies for the SiPM-based ToF-PET component of the GE SIGNA PET/MR system. Med Phys. 2016 May 1;43(5):2334–43.

Grodzki DM, Jakob PM, Heismann B. Ultrashort echo time imaging using pointwise encoding time reduction with radial acquisition (PETRA). Magn Reson Med. 2012 Feb;67(2):510–8.

Herzog H, Pietrzyk U, Shah NJ, Ziemons K. The current state, challenges and perspectives of MR-PET. Neuroimage. 2010 Feb;49(3):2072–82.

Herzog H, Lerche C. Advances in Clinical PET/MRI Instrumentation. PET Clin. 2016 Apr;11(2):95–103.

Heußer T, Mann P, Rank CM, Schäfer M, Dimitrakopoulou-Strauss A, Schlemmer H-P, et al. Investigation of the halo-artifact in 68Ga-PSMA-11-PET/MRI. PLoS One [Internet]. 2017 Aug 17;12(8). Available from: https://www.ncbi.nlm.nih.gov/pmc/articles/PMC5560715/

Hirano Y, Koshino K, Iida H. Influences of 3D PET scanner components on increased scatter evaluated by a Monte Carlo simulation. Phys Med Biol. 2017 May 21;62(10):4017–30.

Hitz S, Habekost C, Fürst S, Delso G, Förster S, Ziegler S, et al. Systematic Comparison of the Performance of Integrated Whole-Body PET/MR Imaging to Conventional PET/CT for ^{18}F-FDG Brain Imaging in Patients Examined for Suspected Dementia. J Nucl Med. 2014 Jun;55(6):923–31.

Hofmann M, Steinke F, Scheel V, Charpiat G, Farquhar J, Aschoff P, et al. MRI-Based Attenuation Correction for PET/MRI: A Novel Approach Combining Pattern Recognition and Atlas Registration. J Nucl Med. 2008 Nov 1;49(11):1875–83.

Hoffman EJ and Phelps ME, Positron Emission Tomography: Principles and Quantitation. In: Positron Emission Tomography and Autoradiography, Eds.: Phelps ME, Mazziota JC and Schlebert HR, Raven Press, New York, 1986.

Hofmann M, Pichler B, Schölkopf B, Beyer T. Towards quantitative PET/MRI: a review of MR-based attenuation correction techniques. Eur J Nucl Med Mol Imaging. 2009 Mar;36 Suppl 1:S93-104.

Holdsworth CH, Levin CS, Janecek M, Dahlbom M, Hoffman EJ. Performance analysis of an improved 3-D PET Monte Carlo simulation and scatter correction. IEEE Transactions on Nuclear Science. 2002 Feb;49(1):83–9.

Hori Y, Hirano Y, Koshino K, Moriguchi T, Iguchi S, Yamamoto A, et al. Validity of using a 3-dimensional PET scanner during inhalation of 15O-labeled oxygen for quantitative assessment of regional metabolic rate of oxygen in man. Phys Med Biol. 2014 Sep 21;59(18):5593–609.

Hu Z, Ojha N, Renisch S, Schulz V, Torres I, Buhl A, et al. MR-based attenuation correction for a whole-body sequential PET/MR system. In: 2009 IEEE Nuclear Science Symposium Conference Record (NSS/MIC). 2009. p. 3508–12.

Iatrou M, Manjeshwar RM, Ross SG, Thielemans K, Stearns CW. 3D implementation of Scatter Estimation in 3D PET. In: 2006 IEEE Nuclear Science Symposium Conference Record. 2006. p. 2142–5.

Iatrou M, Manjeshwar RM, Stearns CW. Comparison of two 3D implementations of TOF scatter estimation in 3D PET. In: 2007 IEEE Nuclear Science Symposium Conference Record. 2007. p. 3474–7.

Iida H, Hori Y, Ishida K, Imabayashi E, Matsuda H, Takahashi M, et al. Three-dimensional brain phantom containing bone and grey matter structures with a realistic head contour. Ann Nucl Med. 2013 Jan;27(1):25–36.

Izquierdo-Garcia D, Hansen AE, Förster S, Benoit D, Schachoff S, Fürst S, et al. An SPM8-based approach for attenuation correction combining segmentation and nonrigid template formation: application to simultaneous PET/MR brain imaging. J Nucl Med. 2014 Nov;55(11):1825–30.

Jang H, Liu F, Bradshaw T, McMillan AB. Rapid dual-echo ramped hybrid encoding MR-based attenuation correction (dRHE-MRAC) for PET/MR. Magn Reson Med. 2017 Oct 2;

Jakoby BW, Bercier Y, Conti M, Casey ME, Bendriem B, Townsend DW. Physical and clinical performance of the mCT time-of-flight PET/CT scanner. Phys Med Biol. 2011 Apr 21;56(8):2375–89.

Johansson A, Karlsson M, Nyholm T. CT substitute derived from MRI sequences with ultrashort echo time. Med Phys. 2011 May;38(5):2708–14.

Johansson A, Garpebring A, Asklund T, Nyholm T. CT substitutes derived from MR images reconstructed with parallel imaging. Med Phys. 2014 Aug;41(8):082302.

Joshi A, Koeppe RA, Fessler JA. Reducing between scanner differences in multi-center PET studies. Neuroimage. 2009 May 15;46(1):154–9.

Juttukonda MR, Mersereau BG, Chen Y, Su Y, Rubin BG, Benzinger TLS, et al. MR-based attenuation correction for PET/MRI neurological studies with continuous-valued attenuation coefficients for bone through a conversion from R2* to CT-Hounsfield units. Neuroimage. 2015 May 15;112:160–8.

Keereman V, Fierens Y, Broux T, Deene YD, Lonneux M, Vandenberghe S. MRI-Based Attenuation Correction for PET/MRI Using Ultrashort Echo Time Sequences. J Nucl Med. 2010 May 1;51(5):812–8.

Keereman V, Holen RV, Mollet P, Vandenberghe S. The effect of errors in segmented attenuation maps on PET quantification. Med Phys. 2011 Nov;38(11):6010–9.

Keereman V, Mollet P, Berker Y, Schulz V, Vandenberghe S. Challenges and current methods for attenuation correction in PET/MR. Magn Reson Mater Phy. 2013 Feb 1;26(1):81–98.

Khalifé M, Fernandez B, Jaubert O, Soussan M, Brulon V, Buvat I, et al. Subject-specific bone attenuation correction for brain PET/MR: can ZTE-MRI substitute CT scan accurately? Phys Med Biol [Internet]. 2017; Available from: http://iopscience.iop.org/10.1088/1361-6560/aa8851

Khateri P, Saligheh Rad H, Jafari AH, Fathi Kazerooni A, Akbarzadeh A, Shojae Moghadam M, et al. Generation of a Four-Class Attenuation Map for MRI-Based Attenuation Correction of PET Data in the Head Area Using a Novel Combination of STE/Dixon-MRI and FCM Clustering. Mol Imaging Biol. 2015 Dec;17(6):884–92.

Kinahan PE, Townsend DW, Beyer T, Sashin D. Attenuation correction for a combined 3D PET/CT scanner. Med Phys. 1998 Oct;25(10):2046–53.

Klein O, Nishina Y. Über die Streuung von Strahlung durch freie Elektronen nach der neuen relativistischen Quantendynamik von Dirac Z. Z Phys 1929;52:853–68.

Koesters T, Friedman KP, Fenchel M, Zhan Y, Hermosillo G, Babb J, et al. Dixon Sequence with Superimposed Model-Based Bone Compartment Provides Highly Accurate PET/MR Attenuation Correction of the Brain. J Nucl Med. 2016 Jun 1;57(6):918–24.

Kolthammer JA, Muzic RF, Ye J. Method for Modeling and Accounting for Cascade Gammas in Images. Patent number US20160048615. 2016 Feb 18; Available from: https://www.google.com/patents/US20160048615

Kops ER, Herzog H. Template based attenuation correction for PET in MR-PET scanners. In: IEEE Nuclear Science Symposium Conference Record, 2008 NSS '08. 2008. p. 3786–9.

Kops ER, Hautzel H, Herzog H, Antoch G, Shah NJ. Comparison of Template-Based Versus CT-Based Attenuation Correction for Hybrid MR/PET Scanners. IEEE Transactions on Nuclear Science. 2015 Oct;62(5):2115–21.

Ladefoged CN, Benoit D, Law I, Holm S, Kjær A, Højgaard L, et al. Region specific optimization of continuous linear attenuation coefficients based on UTE (RESOLUTE): application to PET/MR brain imaging. Phys Med Biol. 2015 Oct 21;60(20):8047–65.

Ladefoged CN, Law I, Anazodo U, St. Lawrence K, Izquierdo-Garcia D, Catana C, et al. A multicentre evaluation of eleven clinically feasible brain PET/MRI attenuation correction techniques using a large cohort of patients. NeuroImage. 2017 Feb 15;147:346–59.

Ladefoged CN, Andersen FL, Kjær A, Højgaard L, Law I. RESOLUTE PET/MRI Attenuation Correction for O-(2-(18)F-fluoroethyl)-L-tyrosine (FET) in Brain Tumor Patients with Metal Implants. Front Neurosci. 2017;11:453.

Larsson A, Johansson A, Axelsson J, Nyholm T, Asklund T, Riklund K, et al. Evaluation of an attenuation correction method for PET/MR imaging of the head based on substitute CT images. MAGMA. 2013 Feb;26(1):127–36.

Levin CS, Dahlbom M, Hoffman EJ. A Monte Carlo correction for the effect of Compton scattering in 3-D PET brain imaging. IEEE Transactions on Nuclear Science. 1995 Aug;42(4):1181–5.

Li Y, Defrise M, Metzler SD, Matej S. Transmission-less attenuation estimation from time-of-flight PET histo-images using consistency equations. Phys Med Biol. 2015 Aug 21;60(16):6563–83.

Magota K, Shiga T, Asano Y, Shinyama D, Ye J, Perkins AE, et al. Scatter correction with combined single-scatter simulation and Monte Carlo simulation scaling improved the visual artifacts and quantification in 3D brain PET/CT imaging with (15)O-gas inhalation. J Nucl Med. 2017 Jun 23;

Malone IB, Ansorge RE, Williams GB, Nestor PJ, Carpenter TA, Fryer TD. Attenuation Correction Methods Suitable for Brain Imaging with a PET/MRI Scanner: A Comparison of Tissue Atlas and Template Attenuation Map Approaches. J Nucl Med. 2011 Jul 1;52(7):1142–9.

Mansor S, Boellaard R, Huisman MC, van Berckel BNM, Schuit RC, Windhorst AD, et al. Impact of New Scatter Correction Strategies on High-Resolution Research Tomograph Brain PET Studies. Mol Imaging Biol. 2016 Aug;18(4):627–35.

Martinez-Möller A, Souvatzoglou M, Delso G, Bundschuh RA, Chefd'hotel C, Ziegler SI, et al. Tissue classification as a potential approach for attenuation correction in whole-body PET/MRI: evaluation with PET/CT data. J Nucl Med. 2009 Apr;50(4):520–6.

Mehranian A, Arabi H, Zaidi H. Vision 20/20: Magnetic resonance imaging-guided attenuation correction in PET/MRI: Challenges, solutions, and opportunities. Med Phys. 2016 Mar 1;43(3):1130–55.

Mehranian A, Arabi H, Zaidi H. Quantitative analysis of MRI-guided attenuation correction techniques in time-of-flight brain PET/MRI. Neuroimage. 2016 Apr 15;130:123–33.

Mehranian A, Zaidi H. Impact of time-of-flight PET on quantification errors in MR imaging-based attenuation correction. J Nucl Med. 2015 Apr;56(4):635–41.

Mehranian A, Zaidi H. Joint Estimation of Activity and Attenuation in Whole-Body TOF PET/MRI Using Constrained Gaussian Mixture Models. IEEE Trans Med Imaging. 2015 Sep;34(9):1808–21.

Mehranian A, Zaidi H, Reader AJ. MR-guided joint reconstruction of activity and attenuation in brain PET-MR. Neuroimage. 2017 Sep 13;162:276–88.

Meikle SR, Dahlbom M, Cherry SR. Attenuation correction using count-limited transmission data in positron emission tomography. J Nucl Med. 1993 Jan;34(1):143–50.

Meikle SR, Badawi RD. Quantitative Techniques in PET. In: Positron Emission Tomography [Internet]. Springer, London; 2005 [cited 2017 Oct 3]. p. 93–126. Available from: https://link.springer.com/chapter/10.1007/1-84628-007-9_5

Mérida I, Reilhac A, Redouté J, Heckemann RA, Costes N, Hammers A. Multi-atlas attenuation correction supports full quantification of static and dynamic brain PET data in PET-MR. Phys Med Biol. 2017 Apr 7;62(7):2834–58.

Miwa K, Umeda T, Murata T, Wagatsuma K, Miyaji N, Terauchi T, et al. Evaluation of scatter limitation correction: a new method of correcting photopenic artifacts caused by patient motion during whole-body PET/CT imaging. Nuclear Medicine Communications. 2016 Feb;37(2):147–54.

Mollet P, Keereman V, Clementel E, Vandenberghe S. Simultaneous MR-compatible emission and transmission imaging for PET using time-of-flight information. IEEE Trans Med Imaging. 2012 Sep;31(9):1734–42.

Mollet P, Keereman V, Bini J, Izquierdo-Garcia D, Fayad ZA, Vandenberghe S. Improvement of attenuation correction in time-of-flight PET/MR imaging with a positron-emitting source. J Nucl Med. 2014 Feb;55(2):329–36.

Myers R, Cunningham V, Bailey DL, et al, editors. Quantification of Brain Function Using PET. San Diego (CA): Academic Press;1996.

Natterer, F., Herzog, H.: Attenuation correction in positron emission tomography. Math. Meth. Appl. Sci. 1992; 15: 321-330

Natterer F. Determination of tissue attenuation in emission tomography of optically dense media. Inverse Problems. 1993;9(6):731.

Navalpakkam BK, Braun H, Kuwert T, Quick HH. Magnetic resonance-based attenuation correction for PET/MR hybrid imaging using continuous valued attenuation maps. Invest Radiol. 2013 May;48(5):323–32.

Nuyts J, Dupont P, Stroobants S, Benninck R, Mortelmans L, Suetens P. Simultaneous maximum a posteriori reconstruction of attenuation and activity distributions from emission sinograms. IEEE Trans Med Imaging. 1999 May;18(5):393–403.

Ollinger JM. Model-based scatter correction for fully 3D PET. Phys Med Biol. 1996 Jan;41(1):153–76.

Ouyang J, Chun SY, Petibon Y, Bonab AA, Alpert N, Fakhri GE. Bias atlases for segmentation-based PET attenuation correction using PET-CT and MR. IEEE Trans Nucl Sci. 2013 Oct 1;60(5):3373–82.

Panin VY, Aykac M, Casey ME. Simultaneous reconstruction of emission activity and attenuation coefficient distribution from TOF data, acquired with external transmission source. Phys Med Biol. 2013 Jun 7;58(11):3649–69.

Poynton CB, Chen KT, Chonde DB, Izquierdo-Garcia D, Gollub RL, Gerstner ER, et al. Probabilistic atlas-based segmentation of combined T1-weighted and DUTE MRI for calculation of head attenuation maps in integrated PET/MRI scanners. Am J Nucl Med Mol Imaging. 2014;4(2):160–71.

Rausch I, Rischka L, Ladefoged CN, Furtner J, Fenchel M, Hahn A, et al. PET/MRI for Oncologic Brain Imaging: A Comparison of Standard MR-Based Attenuation Corrections with a Model-Based Approach for the Siemens mMR PET/MR System. J Nucl Med. 2017 Sep 1;58(9):1519–25.

Rezaei A, Defrise M, Bal G, Michel C, Conti M, Watson C, et al. Simultaneous reconstruction of activity and attenuation in time-of-flight PET. IEEE Trans Med Imaging. 2012 Dec;31(12):2224–33.

Rezaei A, Nuyts J, Deirise M. Analytic reconstruction of the attenuation from 3D time-of-flight PET data. In: 2012 IEEE Nuclear Science Symposium and Medical Imaging Conference Record (NSS/MIC). 2012. p. 2330–3.

Rezaei A, Defrise M, Nuyts J. ML-reconstruction for TOF-PET with simultaneous estimation of the attenuation factors. IEEE Trans Med Imaging. 2014 Jul;33(7):1563–72.

Rorden C, Bonilha L, Fridriksson J, Bender B, Karnath H-O. Age-specific CT and MRI templates for spatial normalization. Neuroimage. 2012 Jul 16;61(4):957–65.

Rothfuss H, Panin V, Moor A, Young J, Hong I, Michel C, et al. LSO background radiation as a transmission source using time of flight. Phys Med Biol. 2014 Sep 21;59(18):5483–500.

Roy S, Wang W-T, Carass A, Prince JL, Butman JA, Pham DL. PET Attenuation Correction using Synthetic CT from Ultrashort Echo-time MRI. J Nucl Med. 2014 Dec;55(12):2071–7.

Schulz V, Torres-Espallardo I, Renisch S, Hu Z, Ojha N, Börnert P, et al. Automatic, three-segment, MR-based attenuation correction for whole-body PET/MR data. Eur J Nucl Med Mol Imaging. 2011 Jan;38(1):138–52.

Schreibmann E, Nye JA, Schuster DM, Martin DR, Votaw J, Fox T. MR-based attenuation correction for hybrid PET-MR brain imaging systems using deformable image registration. Med Phys. 2010 May;37(5):2101–9.

Schramm G, Langner J, Hofheinz F, Petr J, Beuthien-Baumann B, Platzek I, et al. Quantitative accuracy of attenuation correction in the Philips Ingenuity TF whole-body PET/MR system: a direct comparison with transmission-based attenuation correction. MAGMA. 2013 Feb;26(1):115–26.

Sekine T, Buck A, Delso G, Ter Voert EEGW, Huellner M, Veit-Haibach P, et al. Evaluation of Atlas-Based Attenuation Correction for Integrated PET/MR in Human Brain: Application of a Head Atlas and Comparison to True CT-Based Attenuation Correction. J Nucl Med. 2016 Feb;57(2):215–20.

Sekine T, Burgos N, Warnock G, Huellner M, Buck A, Ter Voert EEGW, et al. Multi-Atlas-Based Attenuation Correction for Brain 18F-FDG PET Imaging Using a Time-of-Flight PET/MR Scanner: Comparison with Clinical Single-Atlas- and CT-Based Attenuation Correction. J Nucl Med. 2016 Aug;57(8):1258–64.

Sekine T, Ter Voert EEGW, Warnock G, Buck A, Huellner M, Veit-Haibach P, et al. Clinical Evaluation of Zero-Echo-Time Attenuation Correction for Brain 18F-FDG PET/MRI: Comparison with Atlas Attenuation Correction. J Nucl Med. 2016 Dec;57(12):1927–32.

Son Y-D, Kim H-K, Kim S-T, Kim N-B, Kim Y-B, Cho Z-H. Analysis of Biased PET Images Caused by Inaccurate Attenuation Coefficients. J Nucl Med. 2010 May 1;51(5):753–60.

Soultanidis GM, Mackewn JE, Tsoumpas C, Marsden PK. PVA Cryogel for Construction of Deformable PET-MR Visible Phantoms. IEEE Transactions on Nuclear Science. 2013 Feb;60(1):95–102.

Su K-H, Hu L, Stehning C, Helle M, Qian P, Thompson CL, et al. Generation of brain pseudo-CTs using an undersampled, single-acquisition UTE-mDixon pulse sequence and unsupervised clustering. Med Phys. 2015 Aug;42(8):4974–86.

Surti S, Kuhn A, Werner ME, Perkins AE, Kolthammer J, Karp JS. Performance of Philips Gemini TF PET/CT scanner with special consideration for its time-of-flight imaging capabilities. J Nucl Med. 2007 Mar;48(3):471–80.

Ter-Pogossian MM, Mullani NA, Ficke DC, Markham J, Snyder DL. Photon time-of-flight-assisted positron emission tomography. J Comput Assist Tomogr. 1981 Apr;5(2):227–39.

Teuho J, Johansson J, Linden J, Saunavaara V, Tolvanen T, Teräs M. Specification and estimation of sources of bias affecting neurological studies in PET/MR with an anatomical brain phantom. Nuclear Instruments and Methods in Physics Research Section A: Accelerators, Spectrometers, Detectors and Associated Equipment. 2014 Jan 11;734, Part B:179–84.

Teuho J, Tuisku J, Linden J, Teräs M. Effect of sinus attenuation in MR-based attenuation correction in 18F-FDG brain PET/MR. In: EMBEC & NBC 2017 [Internet]. Springer, Singapore; 2017 [cited 2017 Aug 21]. p. 266–9. (IFMBE Proceedings). Available from: https://link.springer.com/chapter/10.1007/978-981-10-5122-7_67

Torrado-Carvajal A, Herraiz JL, Alcain E, Montemayor AS, Garcia-Cañamaque L, Hernandez-Tamames JA, et al. Fast Patch-Based Pseudo-CT Synthesis from T1-Weighted MR Images for PET/MR Attenuation Correction in Brain Studies. J Nucl Med. 2016 Jan;57(1):136–43.

Tzourio-Mazoyer N, Landeau B, Papathanassiou D, Crivello F, Etard O, Delcroix N, et al. Automated anatomical labeling of activations in SPM using a macroscopic anatomical parcellation of the MNI MRI single-subject brain. Neuroimage. 2002 Jan;15(1):273–89.

Valk PE, Bailey DL, Townsend DW, et al, editors. Positron Emission Tomography: Basic Science and Clinical Practice. London: Springer; 2003. p. 115–46

Veit-Haibach P, Kuhn FP, Wiesinger F, Delso G, von Schulthess G. PET-MR imaging using a trimodality PET/CT-MR system with a dedicated shuttle in clinical routine. MAGMA. 2013 Feb;26(1):25–35.

Wagenknecht G, Kaiser H-J, Mottaghy FM, Herzog H. MRI for attenuation correction in PET: methods and challenges. Magn Reson Mater Phy. 2013 Feb 1;26(1):99–113.

Wang W, Hu Z, Gualtieri EE, Parma MJ, Walsh ES, Sebok D, et al. Systematic and Distributed Time-of-Flight List Mode PET Reconstruction. In: IEEE Nuclear Science Symposium Conference Record, 2006. 2006. p. 1715–22.

Watson CC, Newport D, Casey ME. A Single Scatter Simulation Technique for Scatter Correction in 3D PET. In: Three-Dimensional Image Reconstruction in Radiology and Nuclear Medicine [Internet]. Springer, Dordrecht; 1996 [cited 2017 Aug 17]. p. 255–68. (Computational Imaging and Vision). Available from: https://link.springer.com/chapter/10.1007/978-94-015-8749-5_18

Watson CC, Newport D, Casey ME, deKemp RA, Beanlands RS, Schmand M. Evaluation of simulation-based scatter correction for 3-D PET cardiac imaging. IEEE Transactions on Nuclear Science. 1997 Feb;44(1):90–7.

Watson CC. New, faster, image-based scatter correction for 3D PET. In: 1999 IEEE Nuclear Science Symposium Conference Record 1999 Nuclear Science Symposium and Medical Imaging Conference. 1999. p. 1637–41 vol.3.

Watson CC, Casey ME, Michel C, Bendriem B. Advances in scatter correction for 3D PET/CT. In: IEEE Symposium Conference Record Nuclear Science 2004. 2004. p. 3008–12.

Watson CC. Extension of Single Scatter Simulation to Scatter Correction of Time-of-Flight PET. IEEE Transactions on Nuclear Science. 2007 Oct;54(5):1679–86.

Watson CC. Supplemental transmission method for improved PET attenuation correction on an integrated MR/PET. Nuclear Instruments and Methods in Physics Research Section A: Accelerators, Spectrometers, Detectors and Associated Equipment. 2014 Jan 11;734(Part B):191–5.

Werling A, Bublitz O, Doll J, Adam L-E, Brix G. Fast implementation of the single scatter simulation algorithm and its use in iterative image reconstruction of PET data. Phys Med Biol. 2002;47(16):2947.

Werner P, Rullmann M, Bresch A, Tiepolt S, Jochimsen T, Lobsien D, et al. Impact of attenuation correction on clinical [(18)F]FDG brain PET in combined PET/MRI. EJNMMI Res. 2016 Dec;6(1):47.

Werner ME, Surti S, Karp JS. Implementation and Evaluation of a 3D PET Single Scatter Simulation with TOF Modeling. In: IEEE Nuclear Science Symposium Conference Record, 2006. 2006. p. 1768–73.

Wiesinger F, Sacolick LI, Menini A, Kaushik SS, Ahn S, Veit-Haibach P, et al. Zero TEMR bone imaging in the head. Magn Reson Med. 2016 Jan 1;75(1):

Wollenweber SD. Parameterization of a model-based 3-D PET scatter correction. IEEE Transactions on Nuclear Science. 2002 Jun;49(3):722–7.

Wollenweber SD, Ambwani S, Delso G, Lonn AHR, Mullick R, Wiesinger F, et al. Evaluation of an Atlas-Based PET Head Attenuation Correction Using PET/CT & MR Patient Data. IEEE Transactions on Nuclear Science. 2013 Oct;60(5):3383–90.

Wollenweber SD, Ambwani S, Lonn AHR, Shanbhag DD, Thiruvenkadam S, Kaushik S, et al. Comparison of 4-Class and Continuous Fat/Water Methods for Whole-Body, MR-Based PET Attenuation Correction. IEEE Transactions on Nuclear Science. 2013 Oct;60(5):3391–8.

Yang J, Jian Y, Jenkins N, Behr SC, Hope TA, Larson PEZ, et al. Quantitative Evaluation of Atlas-based Attenuation Correction for Brain PET in an Integrated Time-of-Flight PET/MR Imaging System. Radiology. 2017 Jul;284(1):169–79.

Yang J, Wiesinger F, Kaushik S, Shanbhag D, Hope TA, Larson PEZ, et al. Evaluation of sinus/edge corrected ZTE-based attenuation correction in brain PET/MRI. J Nucl Med. 2017 May (In Press).

Ye J, Song X, Hu Z. Scatter correction with combined single-scatter simulation and Monte Carlo simulation for 3D PET. In: 2014 IEEE Nuclear Science Symposium and Medical Imaging Conference (NSS/MIC). 2014. p. 1–3.

Ye J. Fast Scatter Estimation in PET Reconstruction. Patent number US9659389. 2017 May 23; Available from: https://www.google.fi/patents/US9659389

Zaidi H. Comparative evaluation of scatter correction techniques in 3D positron emission tomography. Eur J Nucl Med. 2000 Dec;27(12):1813–26.

Zaidi H. Scatter modelling and correction strategies in fully 3-D PET. Nucl Med Commun. 2001 Nov;22(11):1181–4.

Zaidi H, Hasegawa B. Determination of the attenuation map in emission tomography. J Nucl Med. 2003 Feb;44(2):291–315.

Zaidi H, Montandon M-L, Slosman DO. Magnetic resonance imaging-guided attenuation and scatter corrections in three-dimensional brain positron emission tomography. Med Phys. 2003 May;30(5):937–48.

Zaidi H, Koral KF. Scatter modelling and compensation in emission tomography. Eur J Nucl Med Mol Imaging. 2004 May 1;31(5):761–82.

Zaidi H, editor. Quantitative Analysis of Nuclear Medicine Images. New York: Springer; 2006. p. 205–35.

Zaidi H, Montandon M-L, Meikle S. Strategies for attenuation compensation in neurological PET studies. Neuroimage. 2007 Jan 15;34(2):518–41.

Zaidi H, Montandon M-L. Scatter Compensation Techniques in PET. PET Clinics. 2007 Apr;2(2):219–34.

Zaidi H, Montandon M-L, Slosman DO. Magnetic resonance imaging-guided attenuation and scatter corrections in three-dimensional brain positron emission tomography. Med Phys. 2003 May;30(5):937–48.

Zaidi H, Ojha N, Morich M, Griesmer J, Hu Z, Maniawski P, et al. Design and performance evaluation of a whole-body Ingenuity TF PET-MRI system. Phys Med Biol. 2011 May 21;56(10):3091–106.

Zhang B, Pal D, Hu Z, Ojha N, Guo T, Muswick G, et al. Attenuation correction for MR table and coils for a sequential PET/MR system. In: 2009 IEEE Nuclear Science Symposium Conference Record (NSS/MIC). 2009. p. 3303–6.

Ziegler S, Braun H, Ritt P, Hocke C, Kuwert T, Quick HH. Systematic evaluation of phantom fluids for simultaneous PET/MR hybrid imaging. J Nucl Med. 2013 Aug;54(8):1464–71.

APPENDICES

SUPPLEMENTAL TABLE 1. Anatomical region numbers and their corresponding names as given in the AAL atlas. This research was originally published in JNM. Teuho et al 2017. Quantitative Evaluation of 2 Scatter-Correction Techniques for 18F-FDG Brain PET/MRI in Regard to MR-Based Attenuation Correction. JNM. 2017;58:1691-1698. © by the Society of Nuclear Medicine and Molecular Imaging, Inc.

Region Number	Region Name	Region Number	Region Name
1	Precentral	18	Lingual
2	Rolandic. Oper.	19	Occipital
3	Supp. Motor Area	20	Fusiform
4	Olfactory	21	Postcentral
5	(Region not named)	22	SupraMarginal
6	Frontal. Sup	23	Angular
7	Frontal. Med	24	Precuneus
8	Frontal. Inf	25	ParacentralLobule
9	Rectus	26	Caudate
10	Insula	27	Putamen
11	Cingulum Ant.	28	Pallidum
12	Cingulum Mid.	29	Thalamus
13	Cingulum Post.	30	Heschl.
14	Hippocampus/ ParaHippocampal.	31	Parietal
15	Amygdala	32	Temporal
16	Calcarine	33	Vermis
17	Cuneus	34	Cerebellum Crus.
		35	Cerebellum

Annales Universitatis Turkuensis

Turun yliopisto
University of Turku

ISBN 978-951-29-7137-4 (PRINT)
ISBN 978-951-29-7138-1 (PDF)
ISSN 0355-9483 (PRINT) | ISSN 2343-3213 (PDF)

Painosalama Oy, Turku, Finland 2018